Title
Exploring Lysosomal pH as a Therapeutic Strategy for Neurodegeneration

Author
Chin, Marcus Yu-Yeung

Publication Date
2021

Peer reviewed|Thesis/dissertation

Exploring Lysosomal pH as a Therapeutic Strategy for Neurodegeneration

by
Marcus Chin

DISSERTATION
Submitted in partial satisfaction of the requirements for degree of
DOCTOR OF PHILOSOPHY

in

Pharmaceutical Sciences and Pharmacogenomics

in the

GRADUATE DIVISION
of the
UNIVERSITY OF CALIFORNIA, SAN FRANCISCO

Approved:

DocuSigned by:
Deanna Kroetz
0611A116B51E4AA...

Deanna Kroetz
Chair

DocuSigned by:
Michelle Arkin

Michelle Arkin

DocuSigned by:
Aimee Kao
745CF57D40DB494...

Aimee Kao

Committee Members

Dedication

To my loving family, my beacon of light.

Thank you for supporting me throughout every step of this amazing journey.

And to all my friends, with whom I persevered.

Thank you for lifting my spirits.

Acknowledgements

I am eternally grateful for everyone who has supported me throughout my journey as a PhD student. I feel fortunate to be surrounded by so many amazing individuals who motivated both my scientific and personal endeavors.

I would first like to thank my co-advisors, Drs Michelle Arkin and Aimee Kao for fostering a wonderful collaboration through which I was able to learn so much. Thank you both for your joined efforts in creating a multi-disciplinary, synergistic educational experience.

I sincerely thank Michelle for inspiring my curiosity for drug discovery and high-throughput techniques. Your focus on the scientific methodology and acumen for next-level technologies enabled me to hone my critical thinking skills and appreciate novel trends in science. Thank you for galvanizing the start of my PhD, allowing me the freedom to explore multiple scientific paths, and always being present during challenging times.

I am also thankful to Aimee for welcoming me into her lab with open arms to jumpstart my transition. Your positivity and outlook on neuroscience were contagious, serving as a constant source of encouragement. Your patient connection was always a noble reminder to continue my mission of discovering therapeutics for those in need. Thank you for believing in me and providing an excellent work environment for my studies.

I would also like to thank Dr. Deanna Kroetz for her tremendous role in supporting my progression throughout my PhD. Thank you for your dedication to the PSPG program and for being a compassionate mentor to students. I am grateful that I had the opportunity to pursue my PhD in such a friendly and collaborative atmosphere, which was enabled by your leadership and kindness.

To all the postdocs I have had the pleasure of working with, thank you for training and coaching me in lab. Your advice and guidance were invaluable during my time at UCSF. You are the true unsung heroes of academia. Thank you for your tireless contributions.

Life as a PhD student would not have been the same without the friendships I made along the way. To the graduate students I have commiserated and bonded with, we made it! And for those who are still pursuing their PhD, I know that you will undoubtedly reach your goals with flying colors. Thank you for being a continual source of laughter and joy in my day.

To my amazing friends, thank you for all the social activities and hilarious adventures. You allowed me to achieve a healthy work-life balance outside of graduate school. A special recognition to my college friends for welcoming me into the Bay Area in my first year and for convincing me that the west coast is as enjoyable as the east coast.

And finally, to my loving family, thank you for everything. You are the backbone of my life and I would have never made it this far without you. Michelle, thank you for being my best friend. I feel so fortunate that we were able to support each other in California. Mom and Dad, thank you for never giving up on me. Words cannot describe the amount of unwavering guidance and unconditional love you have given me. I am so blessed to have our amazing family. Thank you from the bottom of my heart.

Contributions

CHAPTER 1:

Reimagining dots and dashes: Visualizing structure and function of organelles for high-content imaging analysis

Marcus Y. Chin, Jether Amos Espinosa, Grace Pohan, Sarine Markossian, and Michelle R. Arkin

Published in Cell Chemical Biology; https://doi.org/10.1016/j.chembiol.2021.01.016

CHAPTER 2:

A genetically encoded, pH-sensitive mTFP1 biosensor for probing lysosomal pH

Marcus Y. Chin, Anand R. Patwardhan, Kean-Hooi Ang, Austin L. Wang, Carolina Alquezar, Mackenzie Welch, Phi T. Nguyen, Michael Grabe, Anna V. Molofsky, Michelle R. Arkin and Aimee W. Kao

Published in American Chemical Society Sensors; https://doi.org/10.1021/acssensors.0c02318

CHAPTER 3:

Phenotypic screening using high-content imaging to identify lysosomal pH modulators in a neuronal cell model

Marcus Y. Chin, Kean-Hooi Ang, Julia Davies, Carolina Alquezar, Virginia G. Garda, Brendan Rooney, Kun Leng, Martin Kampmann, Aimee W. Kao and Michelle R. Arkin

Manuscript submitted

Epigraph

"Man cannot discover new oceans unless he has the courage to lose sight of the shore"

- Andre Gide

"To aim at excellence, our reputation, and friends, and all must be ventured; to aim at the average we run no risk and provide little service"

- Oliver Goldsmith

Exploring Lysosomal pH as a Therapeutic Strategy for Neurodegeneration

Marcus Chin

Abstract

Lysosomes are a type of functional compartment, or organelle, that is responsible for crucial cellular processes such as protein homeostasis, nutrient sensing, molecular signaling, and secretion. These biochemical pathways ultimately dictate the intricate balance between health and diseases, including neurodegeneration and cancer. Despite decades of research on lysosomes, their role in devastating disorders such as Alzheimer's disease remains largely unknown. In order to achieve a better understanding of lysosomes, specifically in the context of therapeutics for neurodegeneration, my thesis aimed to (1) describe the exciting field of organelle probe development for phenotypic discovery campaigns, (2) engineer a novel biochemical probe that measures lysosomal pH, a crucial aspect of lysosomal function in cells and (3) launch a high-throughput drug screen focused on identifying small molecules and possible molecular pathways that govern lysosomal function. Ultimately, this work contributes to the actively expanding field of phenotypic drug discovery, with specific focus on lysosomal pH and development of cell-based quantitative techniques.

TABLE OF CONTENTS

LIST OF FIGURES

LIST OF TABLES

LIST OF ABBREVIATIONS

ALB1; ABL proto-oncogene 1

ATP; Adenosine triphosphate

BafA1; Bafilomycin A1

BDNF; Brain-derived neurotrophic factor

CMV; cytomegalovirus

ConA; Concanamycin A

CQ; Chloroquine

CV; Coefficient of variation

DMSO; Dimethyl sulfoxide

EC_{50}; Half maximal effective concentration

FC; Fold change

FIRE-pHLy; Fluorescence Indicator REporting pH in Lysosomes

FITC; Fluorescein isothiocyanate

FP; Fluorescent Protein

HEK293; Human embryonic kidney 293

HTS; High-throughput screening

iPSC; Induced pluripotent stem cells

LAMP1; Lysosomal-associated membrane protein 1

LAMP2; Lysosomal-associated membrane protein 2

LC3B; Microtubule-associated protein light chain 3B

mTFP1; monomeric teal fluorescent protein

mTOR; Mammalian target of rapamycin

mTORC; mTOR complex

PI3K; Phoshoinositide 3-kinase

RA; Retinoic acid

UbC; ubiquitin C

ULK; Unc-51 like autophagy activating kinase

V-ATPase; Vacuolar-type ATPase

WT; Wildtype

CHAPTER 1: REIMAGINING DOTS AND DASHES: VISUALIZING STRUCTURE AND FUNCTION OF ORGANELLES FOR HIGH-CONTENT IMAGING ANALYSIS

Marcus Y. Chin[1], Jether Amos Espinosa[1], Grace Pohan[1], Sarine Markossian[1,2], and Michelle R. Arkin[1,*]

[1]Small Molecule Discovery Center and Department of Pharmaceutical Chemistry, University of California, San Francisco, California 94143, USA

[2]Current Address: National Center for Advancing Translational Sciences, Rockville, Maryland 20892-4874 USA

*Correspondence and Lead Contact: michelle.arkin@ucsf.edu

Key words: Organelles, functional probes, high-content imaging, high-content analysis, drug screening, mitochondria, lysosome, Golgi apparatus, membraneless organelles

ABSTRACT

Organelles are responsible for biochemical and cellular processes that sustain life and their dysfunction causes diseases from cancer to neurodegeneration. While researchers are continuing to appreciate new roles of organelles in disease, the rapid development of specifically targeted fluorescent probes that report on the structure and function of organelles will be critical to accelerate drug discovery. Here, we highlight four organelles that collectively exemplify the progression of phenotypic discovery, starting with mitochondria, where many functional probes have been described, then continuing with lysosomes and Golgi and concluding with nascently described membraneless organelles. We introduce emerging probe designs to explore organelle-specific morphology and dynamics and highlight recent case studies using high content analysis in order to stimulate further development of novel probes and high-content approaches for organellar high throughput screening.

INTRODUCTION

Organelles are the main structural and functional subunits within our cells. They are the cellular factories and powerhouses involved in maintaining cell health and homeostasis. Disruption of specific organelle functions can be a cause or a symptom of cancer, neurodegeneration, and rare genetic diseases, among others. To discover compounds that correct these disruptions, phenotypic screens can take advantage of automated microscopy (high-content imaging or high-content analysis; HCA) and clinically relevant *in vitro* models such as those using patient-derived, induced pluripotent stem cells (iPSCs). Ideally, such sophisticated screens would include organelle-specific probes that report on the structure, function, and dynamics of organelles in live cells.

Fluorescent probes that target specific organelles include chemical dyes that bind based on particular biological features, such as net charge or lipophilicity, and genetically encoded protein sensors with fluorescent proteins (FPs) fused to an organelle-specific tag **(Fig. 1.1A)**. Small-molecule probes tend to be bright and easy to use, while genetically encoded sensors have the advantages of high organellar specificity, controlled expression, low toxicity (for extended live-cell imaging), and use in higher order models. Chemical and biological probes can be used to monitor *structural* features such as size, shape, number, and dynamics of the organelle. *Functional* probes also report on the organelle's biological function, such as the pH and protein degradation capacity of the lysosome or protein transport across the Golgi apparatus. HCA-based screens take advantage of structural and functional probes to discover and characterize molecules or genes that modulate organelle dysfunction. For HCA, ideal fluorophores have high photostability for live imaging, high quantum yield for sensitivity, and narrow excitation and

emission spectra to allow multi-color imaging. Furthermore, fluorescence-based sensors should show low toxicity and minimally perturb organelle function.

For some organelles, an array of functional probes are already available; for others, organelle-specific sensors are being actively developed or sit on the more distant horizon (Rosania et al., 2003; Thompson et al., 2017; Valm et al., 2017; Zhu et al., 2016). For example, functional probes to quantify mitochondrial health have been utilized throughout the drug discovery industry, particularly to predict hepatotoxicity (Iannetti et al., 2019). For other organelles such as lysosomes, probes have largely concentrated on interrogating one functional aspect (e.g. pH) (Yue et al., 2016), but recent efforts aimed at improving probe specificity, encompassing other lysosomal functions into probe design and translating existing ones into screening paradigms. Functional probes for organelles such as the Golgi apparatus (herein known as the Golgi) and membraneless organelles (MLOs) are in development, and are just beginning to be utilized in high throughput applications.

Here, we introduce the state-of-the-art for the design and HCA application of organelle-specific sensors for these four organelles **(Fig. 1.1B; Table 1.1)**. Additional organelles have been the subject of recent reviews (Daemen et al., 2015; Fam et al., 2018; Kempfer and Pombo, 2020; Lajoie et al., 2014; Panda et al., 2019; Weiss et al., 2018). The emergence of new probes will facilitate a better understanding of organellar biology and provide a platform to launch phenotypic screens with organelle-specific readouts that are directly correlated with diseases.

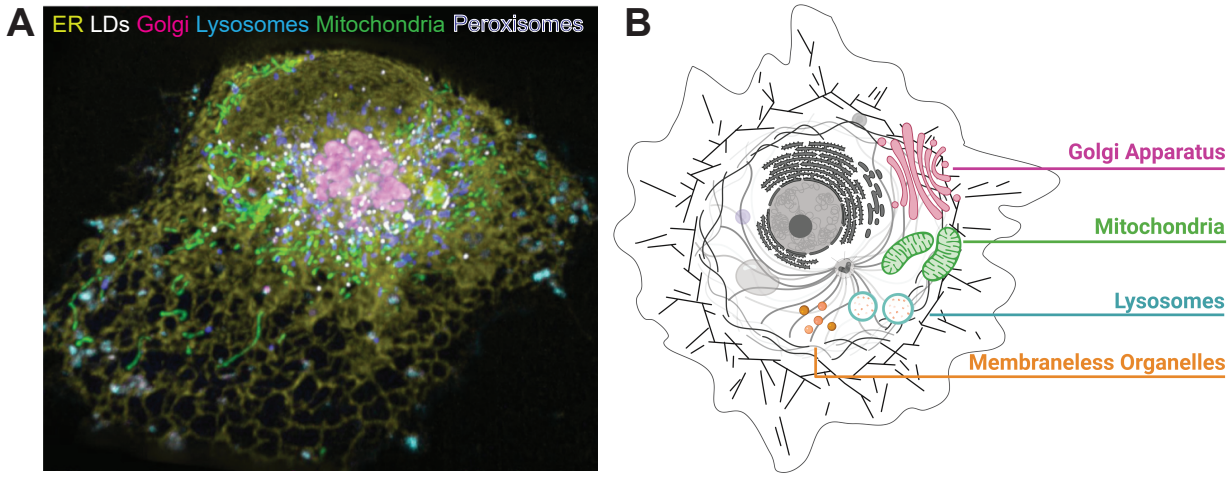

Figure 1.1 Organelle-specific probes elucidate intricate networks and a multitude of foci within the animal cell.
(A) Maximum intensity projection of images captured by a multispectral lattice light sheet microscope of a COS-7 cell either expressing fluorescent proteins or labeled with dyes targeting different organelles including the endoplasmic reticulum (ER), lipid droplets (LDs), the Golgi, lysosomes, mitochondria, and peroxisomes (adapted with permission from Cohen et al., 2018). (B) A schematic depicting the major organelles in an animal cell and highlighting the organelles that are the focus of this review. See also **Table 1.1**. Created with BioRender.com.

MITOCHONDRIA

Mitochondrial structure, function, and disease relevance

Mitochondria, often called "powerhouses" of the cell, produce adenosine triphosphate (ATP), the energy currency of most cellular processes. Mitochondria are composed of an outer and inner membrane, which is the site of ATP-generating oxidative phosphorylation. Highly convoluted cristae structures of the inner membrane increase surface area to maximize ATP yield through the electron transport chain (ETC). As electrons are shuttled through the ETC, the mitochondrial membrane potential ($\Delta\Psi$) forms between the negatively-charged matrix and positively-charged intermembrane space to maintain ATP production and storage **(Fig. 1.2A)**. Additionally, mitochondria have important roles in regulating apoptosis, cellular redox homeostasis, intracellular calcium signaling, and neurogenesis (Ji et al., 2020; Khacho and Slack,

2018; Liu et al., 2020; Vringer and Tait, 2019). Interestingly, mitochondria are not synthesized *de novo*; instead, they are recycled through regulated cycles of fission and fusion (McInnes, 2013). Finally, mitochondria are the only non-nuclei organelles in animal cells with their own DNA (mtDNA) that codes for RNAs and proteins involved in oxidative phosphorylation.

Mitochondrial dysregulation has broad implications in disease, particularly in neurodegeneration and myopathies. Neurons and muscle cells may be particularly vulnerable because their functions depend heavily on ATP consumption (Chanséaume and Morio, 2009; Mattson et al., 2008). Specific mutations in mitochondria-related proteins lead to myopathies such as Duchenne muscular dystrophy, where excessive calcium exposure leads to mitochondrial swelling, overproduction of reactive oxygen species (ROS), and increased mitochondrial permeability (Vila et al., 2017). Additionally, mitochondrial damage is also an effect of environmental toxins and drugs, particularly in the liver (drug-induced liver injury, or DILI) (Aleo et al., 2014). The diversity of mitochondrial dysfunctions in disease justifies the design of probes that monitor these different functions.

Structural and functional probes for mitochondria

The development of fluorescent dyes and genetically encoded probes to monitor mitochondrial function is advanced compared to many other organelles. Probes cover a broad array of mitochondrial features, including $\Delta\Psi$, mtDNA, ATP and ROS **(Fig. 1.2A-D)**. Many of these are suitable for live imaging, allowing the measurement of dynamics. Furthermore, multiple probes have been used in combination to discover and characterize molecules that modulate mitochondrial function.

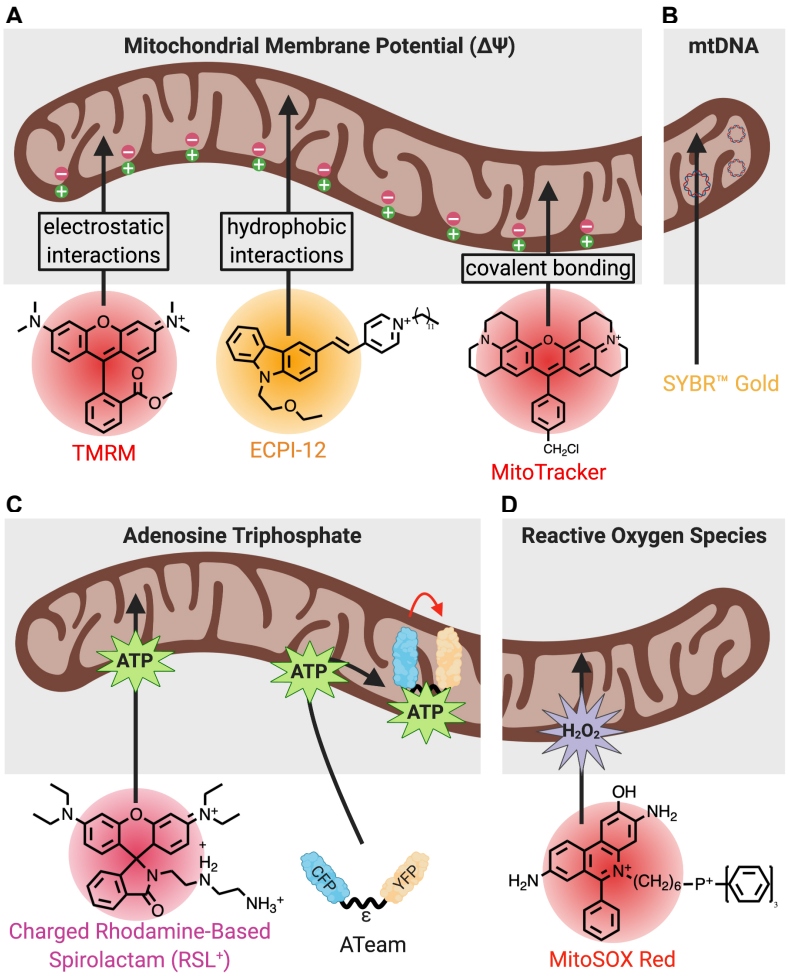

Figure 1.2. Examples of biomarkers used in live-cell readouts to quantify mitochondrial health. (A) Cationic fluorophores that target the negative mitochondrial membrane potential (ΔΨ) in the matrix. Tetramethylrhodamine methyl ester (TMRM) is a functional probe that uses electrostatic interactions with the polarized ΔΨ to directly measure changes in ΔΨ (Elmore et al., 2004). (*E*)-1-dodecyl-4-(2-(9-(2-ethoxyethyl)-9*H*-carbazol-3-yl)vinyl)pyridin-1-ium iodide (ECPI-12) is a structural probe that uses reaction-free lipophilic interactions with the mitochondrial inner membrane (Zhang et al., 2019). MitoTrackers are structural probes that irreversibly bind to thiol groups to permanently stain mitochondria independent of ΔΨ fluctuations (Chazotte, 2011). (B) The proprietary mitochondrial DNA (mtDNA) probe SYBR Gold binds directly to mtDNA present in mitochondrial nucleoids (Jevtic et al., 2018). (C) Probes designed to target ATP include charged rhodamine-based spirolactams (RSL^+) and Adenosine 5-Triphosphate indicator based on Epsilon subunit for Analytical Measurements (ATeam) (Imamura et al., 2009). ATeam is shown with the epsilon (ε) subunit flanked between Cyan Fluorescent Protein (CFP) and Yellow Fluorescent Protein (YFP). (D) MitoSOX Red targets reactive oxygen species (ROS) within live mitochondria (De Biasi et al., 2016). Created with BioRender.com.

Cationic lipophilic dyes, such as tetramethylrhodamine methyl ester (TMRM) are functional probes that report on changes in ΔΨ. TMRM accumulates inside live mitochondria and forms temporary electrostatic interactions with the polarized ΔΨ **(Fig. 1.2A)**. When

mitochondria are depolarized or damaged, these ionic interactions are lost, TMRM diffuses away, and mitochondrial fluorescence intensity decreases. TMRM also shows fast membrane equilibration, high specificity, low ETC inhibition, and low toxicity (Elmore et al., 2004). TMRM has been extensively used to investigate mitochondrial ΔΨ in cancer cells; for instance, lung (A549, H446, SPC) and breast (MCF-7) cancer cells were shown to have higher ΔΨ compared to noncancerous control cells (Creed and McKenzie, 2019; Zhang et al., 2015). More recent ΔΨ probes like ECPI-12 (named after its modified C_{12}-alkyl chain) rely on hydrophobic interactions to localize to the inner mitochondrial membrane without permanently binding to thiol groups **(Fig. 1.2A)**. Therefore, ECPI-12 is highly ΔΨ-independent and allows for high biocompatibility in situ and long-term tracking of mitochondria with fewer mitotoxic side-effects (Zhang et al., 2019) compared to commercially available dyes such as MitoTrackers that are reaction-based (Chazotte, 2011; Zhang et al., 2019).

Visualizing mtDNA provides another avenue to probe mitochondrial structure and function **(Fig. 1.2B)**. Jevtic et al. tested whether a positively charged cyanine dye called SYBR Gold could selectively label mitochondrial nucleoids, the region within the mitochondria that houses mtDNA (Jevtic et al., 2018; Tuma et al., 1999). At low concentrations, SYBR Gold preferentially accumulated within unperturbed mitochondria in live cells. Super-resolution structured illumination microscopy (SIM) (Gustafsson et al., 2008) was then used to track mitochondrial nucleoid motion. Though at an early stage of development, mtDNA-binding dyes like SYBR Gold could eventually probe mtDNA-related pathologies, such as systemic lupus erythematosus (Caielli et al., 2016), and be multiplexed with other functional dyes.

ATP levels are an important indicator of mitochondrial health. ATP is commonly measured by bioluminescent assays that detect the ATP-dependent luciferin-luciferase reaction (Crouch et al., 1993). These assays require cell lysis and are not selective for mitochondrial ATP; by contrast, an ideal ATP probe would work in living systems and bind specifically to mitochondrial ATP. To address these challenges, de la Fuente-Herreruela et al. introduced a small-molecule dye called rhodamine-based spirolactam (RSL^+) that accumulated specifically in mitochondria and measured mitochondrial ATP levels in live cells (de la Fuente-Herreruela et al., 2017) **(Fig. 1.2C)**. Hydrogen bonding between the polyphosphates in ATP and the diethylenetriamine moiety in RSL^+ led to opening of the spirolactam ring, resulting in increased fluorescence. RSL^+ measured baseline ATP levels in human skin fibroblasts as well as ATP depletion in mouse embryonic fibroblasts treated with a mitochondrial toxin.

Adenosine 5-Triphosphate indicator based on epsilon (ε) subunit for analytical measurements (ATeam) is a genetically encoded ATP sensor based on fluorescence resonance energy transfer (FRET) **(Fig. 1.2C)**. ATP binding causes a conformational change in the ε subunit of *Bacillus subtilis* F_0F_1-ATP synthase, bringing cyan-FP (CFP) and yellow-FP (YFP) variants in proximity to activate a FRET signal (Imamura et al., 2009). One *in vivo* study used ATeam to report mitochondrial ATP levels in a peripheral neuropathy mouse model. ATeam was fused to the mitochondrial targeting sequence of cytochrome c oxidase VIII (COX VIII) and was expressed in the demyelinated axons of mice (van Hameren et al., 2019). Van Hameren et al. concluded that in demyelinating neurodegenerative diseases, decreased mitochondrial ATP levels were due to dysregulated ATP production and increased export rate of mitochondrial ATP to the cytoplasm by ADP/ATP translocase. By localizing ATeam to the mitochondria, this study

provided novel insight on the role that axonal mitochondria had on the production of ATP under pathological conditions.

Mitochondria are hotspots for the formation of ROS, which are important signaling molecules at normal concentrations; however, when mitochondria are damaged, electron leakage can result in the harmful overproduction of ROS (D'Autréaux and Toledano, 2007; Murphy et al., 2016). MitoSOX Red is a commonly used dye that discriminates between cellular and mitochondrial ROS production (De Biasi et al., 2016). MitoSOX Red targets the negatively charged mitochondrial inner membrane through the addition of the lipophilic, cationic substituent triphenyl phosphonium and fluoresces when it reacts with superoxide (Deshwal et al., 2018; Kaludercic et al., 2014) **(Fig. 1.2D)**. Genetically encoded ROS sensors such as HyPer are based on yeast and bacterial ROS-detecting proteins and specifically measure hydrogen peroxide within mitochondria (Ermakova et al., 2014; Markvicheva et al., 2011).

There are several genetically encoded sensors that measure mitochondrial redox state (Liao et al., 2020). Fluorescent proteins roGFP1/2, rxYFP, and rxmRuby2 contain cysteine mutations near the proteins' chromophore (Banach-Latapy et al., 2014; Hanson et al., 2004; Piattoni et al., 2019). Under oxidative environments, the cysteine residues form a disulfide bond and the chromophore is protonated, leading to a shift in its excitation spectrum (from 488 nm to 405 nm for roGFP, for instance). Relative redox environment is thus determined by exciting the protein at both wavelengths and measuring the fluorescence ratio. These probes can then be targeted to different regions within mitochondria by adding mitochondrial localization signal sequences. For instance, targeting rxYFP to the mitochondrial matrix and the intermembrane space demonstrated that the latter is more oxidizing than the former; furthermore, these probes showed that the redox properties of mitochondria and cytosol were independently regulated (Hu

et al., 2008). Very recently, Werley et al. used the mitochondrial targeting sensor mito-roGFP2-Grx1 as part of an array of 20 genetically encoded sensors that have the potential to elucidate signaling cascades and mechanisms of action of chemical probes and drug leads (Werley et al., 2020).

Multiplexing mitochondrial probes for high-content analysis and screening

Mitochondrial dysfunction has become a focus for early diagnosis and intervention for neurodegenerative diseases (Peng et al., 2020). To study mitochondrial function in neurons, Varkuti et al. measured ΔΨ and ATP levels, as reported by TMRM and luciferase respectively, in wild-type primary mouse neurons. Primary screening of 2,400 drugs identified 120 hits that promoted TMRM fluorescence and ATP generation, with a subset validated to promote mitochondrial respiration, mitochondria branching, and overall neurite area. Under neurodegenerative disease contexts such as oxidative stress and Alzheimer's disease mutation, several drugs also protected against ΔΨ decline (Varkuti et al., 2020). To develop a human-relevant screening model for Parkinson's disease (PD), Little et al. were the first to use HCA to evaluate mitochondria in iPSC-derived neurons from patients with mutations in α-synuclein, which is often mutated and aggregated in PD. In this assay, mitochondrial morphology and ΔΨ were determined by measuring TMRM area and intensity, respectively. Cells were imaged and individually analyzed using automated confocal microscopy. PD patient-derived cells displayed reductions in ΔΨ and altered mitochondrial area and length compared to healthy control neurons (Little et al., 2018).

Another study used amyotrophic lateral sclerosis (ALS) iPSC-derived motor neurons to screen for small-molecule regulators that increased axonal transport of mitochondria (Shlevkov et al., 2019) **(Fig. 1.3A)**. In neurons, transport of mitochondria along the axon to distal dendritic

networks is critical for neuronal function and communication; inhibition of axonal trafficking has been linked to disorders such as ALS (Magrané et al., 2014; Wang et al., 2013). Shlevkov et al. labeled mitochondria with the fluorescent protein Mito-DsRed, imaged every 2 seconds for 5 mins, and used an in-house analysis pipeline to quantify the percent of motile mitochondria and the average distance mitochondria traveled along axons and dendrites **(Fig. 1.3B)**. From a screen of 3,200 molecules with known bioactivity, six compounds enhanced mitochondrial axonal transport in the ALS motor neurons. These compounds were reported to inhibit F-actin, Aurora Kinase B (AurKB) and Tripeptidyl peptidase 1 (TPP1); indeed, knocking down these genes phenocopied the effect of the small molecules. It is noteworthy that both the ALS and PD studies utilized patient-derived iPSCs differentiated into cell types relevant for the disease. Though using patient-derived cells increases the complexity of high-throughput screening, these systems may improve translation from assay to clinic.

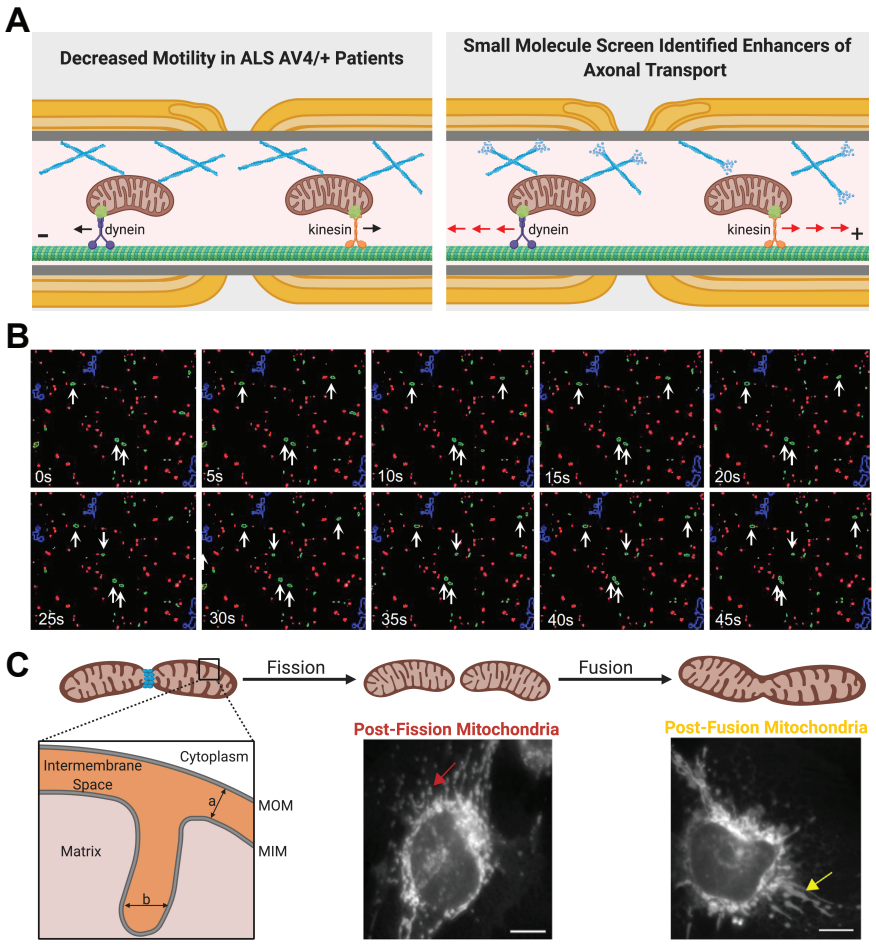

Figure 1.3. Examples of mitochondrial phenotypes amenable to HCA and HTS studies.
(A) High-throughput screening identified aurora kinase B (AurKB), tripeptidyl peptidase 1 (TPP1), and F-actin as targets of mitochondrial axonal trafficking in iPSC-derived neurons from an ALS patient (Shlevkov et al., 2019). (B) Minimum intensity projection of a time-lapse sequence showing stationary (red) versus motile (green) mitochondria. White arrows indicate objects that exhibit significant movement. Images were adapted from (Shlevkov et al., 2019) with permission. (C) Schematic of mitochondrial morphofunction. Structural parameters shown are mitochondrial outer membrane (MOM), mitochondrial inner membrane (MIM), distance between MOM and MIM (labeled "a") and intercristae space (labeled "b") (Bulthuis et al., 2019). Live imaging of mitochondrial morphology using MitoTracker probes show fragmented mitochondria (post-fission; red arrow) and elongated mitochondria (post fusion; yellow arrow). Scale bar represents 10 µm. Microscopy images were adapted from (Harwig et al., 2018) with permission. Created with BioRender.com.

Multiplexing of mitochondrial probes is widely used for studying drug-induced liver injury (DILI). DILI is a major cause of failure in drug development with mitotoxicity being one common cause of hepatotoxicity. Early testing for potential mitochondrial toxicity in high-throughput models could therefore significantly increase drug discovery success. Recently,

Pohan et al. optimized a suite of high-throughput assays to measure mitochondria-related biomarkers indicative of DILI, including ΔΨ, ROS, and ATP, along with other cell health parameters including cell count, glutathione, and vacuolar density (Pohan et al., 2020). Although the assays utilized live cells, the multiplexed dyes were toxic to cells after prolonged exposure and were therefore incompatible for real-time cell monitoring. To enable live, kinetic monitoring of mitochondrial damage, Chandrasekharan et al. developed a screen based on the genetically encoded mt-roGFP2 to measure mitochondrial redox and TMRM to measure ΔΨ (Chandrasekharan et al., 2019; Gutscher et al., 2008). Using time-lapse imaging, the authors demonstrated that mitochondrial oxidation preceded loss of membrane potential and mitochondrial permeability; this order of mitochondrial derangement was consistent for a library of anticancer agents. These studies demonstrate the utility of multiplexing small-molecule and genetically encoded probes for high-throughput and time-dependent measurement of mitochondrial damage for *in vitro* toxicology prediction.

The bidirectional relationship between mitochondrial ultrastructure and function, or morphofunction, is emerging as a crucial aspect of mitochondrial biology and disease (Bulthuis et al., 2019). Mitochondria morphofunction includes the dynamic fission and fusion of the mitochondrial outer and inner membranes, and the maintenance and regulation of cristae **(Fig. 1.3C)**. These processes rapidly change given the physiological needs of the cell (Scott and Youle, 2010) and are dysregulated in multiple diseases (Archer, 2013; Koch et al., 2016; Waterham et al., 2007). For example, activating mutations in the protein-homeostasis regulator valosin-containing protein (VCP) lead to excessive degradation of mitofusin – a protein essential for mitochondrial fusion. VCP mutation thus leads to increased mitochondrial fission, decreased function, and myopathy (Zhang et al., 2017). Interestingly, small-molecule inhibitors of the

mitochondrial outer membrane protein GTPase dynamin-related protein 1 may be able to reverse such excess fission (Bulthuis et al., 2019). In addition, morphofunction is phenotypically more complex than fission and fusion alone and requires sophisticated quantitative tools to explore mitochondrial phenotypic diversity. MitoGraph is an image analysis platform implemented by Harwig et al. to measure individual morphometric characteristics that range from entirely fragmented to hyper-elongated mitochondria (Harwig et al., 2018) **(Fig. 1.3C)**. Mitochondria are detected through image segmentation and then classified through machine learning. MitoGraph has been validated to quantitatively analyze mitochondrial networks, volume, total length, and degree of branching in live and fixed cells. As another example, Iannetti et al. developed an unbiased HCA workflow to compare TMRM-stained mitochondria from two primary human skin fibroblast lines. Using confocal microscopy and multivariate analysis, over 30 mitochondrial descriptors were identified, including mitochondrial shape and branching (Iannetti et al., 2016). Morphofunction analysis could be a compelling approach for unbiased phenotypic drug screening for mitochondrial dysfunction.

Prospect of mitochondrial phenotypic discovery

Taking advantage of the unique structure, functions, and dynamics of mitochondria, diverse chemical and genetically encoded sensors have been developed. Many of these probes are active in live cells and have been incorporated into multiplexed screens and sophisticated cell models. While there is always room for innovation, the maturity of sensor development for mitochondria serves as inspiration for other organelles.

LYSOSOME

Lysosomal structure, function, and disease relevance

Lysosomes are small membrane-bound organelles that serve as major cellular sites for macromolecule degradation, a feat performed by lysosomal hydrolases that operate under acidic conditions. Enzymatic activity is ensured by tight regulation of lysosomal pH, which is profoundly acidic (pH~4.5) compared to other organellar compartments (Casey et al., 2010). Low pH is set by the vacuolar-type H^+-ATPase (V-ATPase) pump that generates a proton gradient by hydrolyzing ATP. Other ion channels and transporters are also involved with balancing ion flux between the lysosomal lumen and cytosol (Mindell, 2012).

Lysosomes are part of the greater endolysosomal network that encompasses endocytosis, membrane trafficking, membrane maturation, and autophagy. This network is critical to cellular homeostasis and is implicated in many diseases. Compared to lysosomal assays, autophagy screening is relatively mature and has been previously reviewed (Fleming et al., 2011; Panda et al., 2019; Shu et al., 2012). In contrast to autophagy, endosomal probe development is more nascent. Defining endosomes is difficult due to the heterogeneous characteristics of endosomal types and biochemical markers (Naslavsky and Caplan, 2018). Lysosomes are positioned between autophagosomes and endosomes in terms of sensor and HCA development and represent an emerging target for phenotypic discovery.

For decades, lysosomes were regarded as static organelles that received and degraded waste. Relatively recently, they have garnered attention as potential primary therapeutic targets because of newly appreciated functions in protein homeostasis, cellular signaling, nutrient sensing, immune response, and secretion (Appelqvist et al., 2013; Settembre et al., 2013). In lysosomal storage disorders (LSDs), for instance, genetic mutations cause lysosomal enzyme

deficiencies and impede the degradation of lipids and proteins. Accumulated waste material, such as cholesterol, is observed across different cell types, including those found in the central nervous system (Bi and Liao, 2010). Additionally, lysosomal enlargement is thought to cause lysosomal impairments, overall cellular dysfunction and cell death in LSDs. Likewise, underperforming lysosomes are linked to the pathogenesis of neurodegenerative diseases. For instance, lysosomal acidification defects are seen in Alzheimer's disease models (Colacurcio and Nixon, 2016; Harguindey et al., 2007; Wolfe et al., 2013). The expression and activity of lysosomal enzymes such as cathepsins are also changed (Stoka et al., 2016). Together, these data suggest that abnormal lysosomal pH reduces degradative efficiency, compromising protein homeostasis and leading to neurodegenerative disease protein deposition. Cancers, by contrast, are characterized by hyperactive lysosomal function, including alterations in lysosomal positioning, composition and volume. Increased activity of lysosomal hydrolases and their enhanced extracellular secretion degrades the extracellular matrix and allows cancer cells to become invasive (Kallunki et al., 2013; Kirkegaard and Jäättelä, 2009).

Lysosome-based screening

Because abnormal lysosomal function is strongly linked to disease pathogenesis, lysosome-specific probes are highly desirable for phenotypic screening. Several HTS studies have explored phenotypes such as lysosomal size, positioning, and calcium regulation in relation to LSDs and cancer **(Fig. 1.4)**.

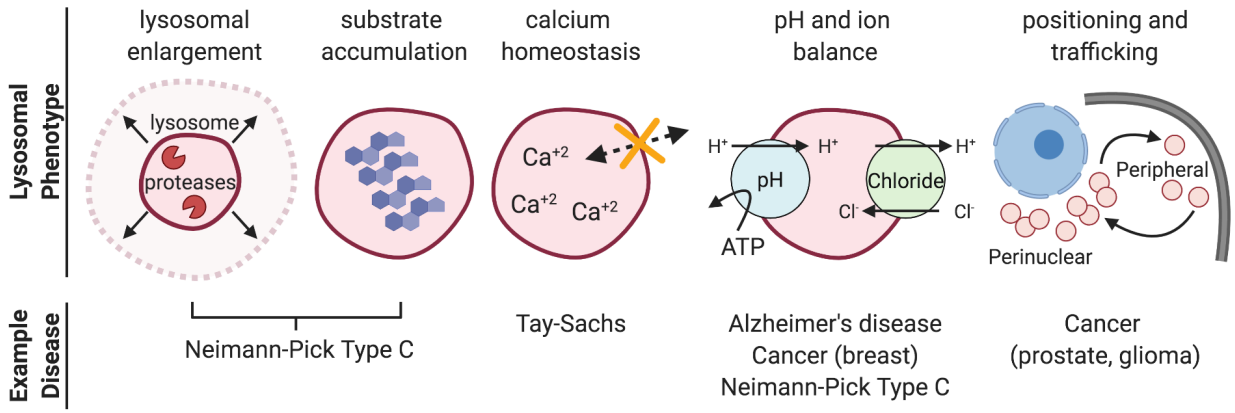

Figure 1.4. Lysosomal phenotypes and diseases highlighted in recently developed probes and HTS studies. References (from left to right): Lysosomal enlargement (Xu et al., 2014); substrate accumulation (Pugach et al., 2018); calcium homeostasis (Colussi and Jacobson, 2016); pH and ion balance (Chen et al., 2015; Leung et al., 2019; Chin et al., 2020; Ponsford et al., 2020; Webb et al., 2020); Positioning and trafficking (Circu et al., 2016; Ishii et al., 2019). Created with BioRender.com.

A majority of lysosome-based phenotypic screens have focused on LSDs. For example, to study Niemann-Pick disease type C (NPC), two independent groups developed HCA assays using patient-derived NPC fibroblasts to screen against lysosomal morphology and cholesterol accumulation (**Fig. 1.4**). NPC is caused by mutations in the cholesterol and lipid transporter genes *NPC1* or *NPC2*, which results in substrate buildup and enlargement of lysosomes. Xu et al. measured the fluorescence and size of lysosomes using LysoTracker, a dye that accumulates in acidic organelles. During assay validation, they found that methyl-β-cyclodextrin (MβCD), which is known to sequester cholesterol (Ilangumaran and Hoessli, 1998; Rosenbaum et al., 2010), reduced the size of enlarged lysosomes found in NPC cells (Xu et al., 2014). Pugach et al. further profiled lysosomal size with LysoTracker and immunofluorescence staining of lysosome-associated membrane protein 1 (LAMP1), a well-established marker of lysosomes. After screening 3532 drugs, kinase inhibitors, and metabolites, twenty-three compounds rescued NPC cholesterol accumulation, as stained by the cholesterol-binding dye fillipin. The antimicrobial compound alexidine was the most active and functioned by increasing mRNA transcript and protein levels of *NPC1* (Pugach et al., 2018).

Targeting lysosomal calcium release may also be a therapeutic approach for treating LSDs (**Fig. 1.4**). Disruption of calcium homeostasis is common to multiple LSDs and causes dysfunctional vesicle membrane dynamics and autophagy (Feng and Yang, 2016; Medina and Ballabio, 2015; Scotto Rosato et al., 2019). Colussi et al. developed a HTS assay to identify small molecules that restored lysosomal calcium function in Tay-Sachs disease (TSD) using patient-derived fibroblasts, which released lower levels of calcium from lysosome stores compared to wild-type cells (Colussi and Jacobson, 2019). Intracellular calcium was measured using a calcium-sensitive indicator Fluo-8 AM after induction of lysosomal calcium release. Primary screening of 1,200 FDA-approved drugs in TSD cells identified the antiparasitic drug pyrimethamine as the most active to restore wild-type levels of calcium release. Pyrimethamine, which accumulates in lysosomes (Clarke et al., 2011; Perrin, 1965), had been implicated in autophagy regulation (Giammarioli et al., 2012; Tommasino et al., 2016) and lysosomal activation (Jang et al., 2016).

Lysosomes traffic away from the perinuclear region towards the periphery during cancer growth and metastasis (**Fig. 1.4**). Tumorigenic stimuli such as acidic extracellular microenvironments promote anterograde lysosomal trafficking to the cell surface, where cathepsins are secreted to initiate tumor invasion (Steffan et al., 2009, 2011). To discover therapeutics that inhibited this lysosomal movement, one study developed a HCA platform and identified modulators of lysosomal positioning in prostate cancer and glioma cells (Circu et al., 2016). Lysosomal positioning, as visualized by LAMP1, was determined based on the number of lysosomes that fell within a pre-designated ring region surrounding the nucleus compared to the cytosol and/or cell surface. From a screen of 2,210 FDA-approved drugs, eighteen compounds preferentially induced perinuclear lysosomal localization. Among the top hits was the

antihelminthic drug niclosamide, which has previously been shown to affect cancer proliferation and survival pathways (Lee et al., 2020; Wang et al., 2018). Niclosamide inhibited cathepsin B secretion and blocked tumor cell migration in motility models. Interestingly, niclosamide altered lysosomal pH, suggesting a correlation between lysosomal acidity and positioning. Taken together, studies such as Pugach et al., Colussi et al., and Circu et al. exemplified the power of drug repurposing campaigns focused on screening lysosomal-specific phenotypes in disease-relevant cell models.

Functional probes targeted to lysosomes

Traditional lysosomal dyes are lipophilic, weak bases that pass through membranes and preferentially target acidic compartments such as lysosomes and late endosomes. Compared to their predecessors, newer generations of probes are organelle-selective and monitor lysosomal functions, providing advantages for future applications in HTS.

Both small-molecule and genetically encoded probes have been designed to measure lysosomal pH. Superior LysoProbes are rhodamine-based dyes that achieve specific lysosomal localization and probe retention by exploiting N-linked glycosylation, a common post-translational modification present on lysosomal membrane proteins that protects them from degradation (Chen et al., 2015) **(Fig. 1.5A)**. Superior LysoProbes were conjugated with N-linked glycan moieties such as lactose and contained a fluorescent rhodamine spirolactam that was sensitive to acidic pH in the range of 4.8 to 6.0. The authors applied this probe to map both lysosomal position and pH changes in response to lobaplatin, a novel anticancer cisplatin analog that induced apoptosis. Compared to control, lobaplatin-treated cells showed enlarged and less acidic lysosomes that accumulated away from the perinuclear region. Thus, Superior LysoProbes were applied to profiling multiple derangements in lysosomes during apoptosis.

Very recently, three genetically encoded lysosomal pH probes have emerged, each focused on a different application. Each included the lysosomal protein LAMP1 fused to different fluorescent protein pairs to measure pH changes in the lysosomal lumen. One FP was selected for sensitivity to pH, while mCherry was used as a reference to normalize protein expression. Ponsford and colleagues created a probe called Ratiometric pHluorin (RpH)-LAMP1-3xFLAG, which detected pH from 4.0 to 7.0. The authors used this probe to map lysosomal pH in cell lines and primary neurons as a function of culture times and learned that pH was highly stable over several days in culture (Ponsford et al., 2020). Webb et al., designed pHLARE (pH Lysosomal Activity REporter), which used superfolder (sf) GFP to sense pH from 4.0 to 6.0 in cancer cells. Interestingly, transfecting the non-transformed breast cell line MCF10a with the oncogene hRASV12 lowered lysosomal pH from 5.23 to 4.67 (Webb et al., 2020). Finally, Chin and colleagues developed Fluorescence Indicator Reporting pH of Lysosomes (FIRE-pHLy), using monomeric teal fluorescent protein 1 (mTFP1) as the pH sensor domain and measured pH from 3.5 to 6.0 **(Fig. 1.5B)** (Chin et al., 2020). FIRE-pHLy was stably expressed and demonstrated consistent response to the V-ATPase inhibitor bafilomycin in cancer cells, neurons, and in *Caenorhabditis elegans* animals. Notably, FIRE-pHLy quantitation used automated microscopy and analysis, demonstrating the potential for future HTS studies with this and potentially with related ratiometric pH sensors.

Besides pH, intraluminal chloride (Cl^-) concentration also plays a major role in lysosomal acidification by balancing the positive transmembrane voltage gradient generated by protons (Mindell, 2012). Deficits in chloride homeostasis lead to severe lysosomal pathologies. For example, deficiency of CLC-7, an H^+/Cl^- antiporter, causes both bone resorption failure and LSD-like neurodegenerative phenotypes (Kasper et al., 2005; Weinert et al., 2010). To better

understand Cl^--mediated lysosomal dynamics, Leung et al. engineered a DNA-based ratiometric biosensor called ChloropHore, which simultaneously measured pH and Cl^- ions in lysosomes using two independent sensor domains based on small-molecule dyes previously described (Saha et al., 2015). An anionic integration domain aided in lysosomal targeting via receptor-mediated endocytosis **(Fig. 1.5C)**. ChloropHore reported pH from 4.5 to 6.5 and physiological Cl^- concentrations from 5 mM to 120 mM (Chakraborty et al., 2017). Addition of ChloropHore to patient-isolated NPC fibroblasts identified differences in diseased lysosomal subpopulations. Compared to wild-type cells, NPC cells showed overall lower numbers of lysosomes with high Cl^- concentrations. Furthermore, the luminal Cl^- concentrations in perinuclear lysosomes was lower than in peripheral lysosomes, while pH was increased in both spatial types (Leung et al., 2019). These data indicated the pathological consequences of aberrant lysosomal distribution, pH, and chloride levels in NPC. This innovative study points the way to using dual ion measurements in future HTS campaigns.

Finally, Ishii et al. developed a genetically encoded protein trafficking probe, lysosomal MEasurement of protein Transporting integrity by RatIo Quantification (METRIQ), that is synthesized in the ER and traffics through the Golgi to lysosomes **(Fig. 1.5D)**. The biosensor consists of a lysosomal resident protein (e.g. LAMP1) attached to sfGFP, a T2A self-cleaving peptide, and mCherry. Upon synthesis, lysosomal-METRIQ autocleaves and releases mCherry into the cytosol, providing an internal control for expression. The remaining lysosomal sfGFP fragment is shuttled into lysosomes where it is degraded and fluorescence is quenched. Therefore, changes in red/green fluorescence ratios indicate alterations in trafficking and lysosomal degradative function. 368 drugs known to inhibit intracellular signaling pathways were added to HeLa cells stably transfected with lysosomal-METRIQ and ratios were measured

by flow cytometry. The cyclin-dependent kinase (CDK) inhibitors Kenpaullone and purvalanol A were among the top hits (Ishii et al., 2019). After target confirmation studies, CDK5 was determined to decrease lysosomal biogenesis independently of cell cycle arrest, although the exact mechanism remained to be elucidated. This study exemplified efforts to further elucidate new targets involved in lysosomal function by screening with lysosome-specific probes.

Prospect of lysosomal phenotypic discovery

Recent studies suggest a deeper complexity to lysosomal biology than previously imagined. Newer designs of probes bolster our understanding of lysosomes by providing more accurate labeling and functional measurements for pH, chloride, protease activity (Cheloha et al., 2019; To et al., 2015), and protein trafficking. Optimization of these functional sensors into HTS platforms will pave the way for discovery of compounds that normalize lysosomal functions altered in disease.

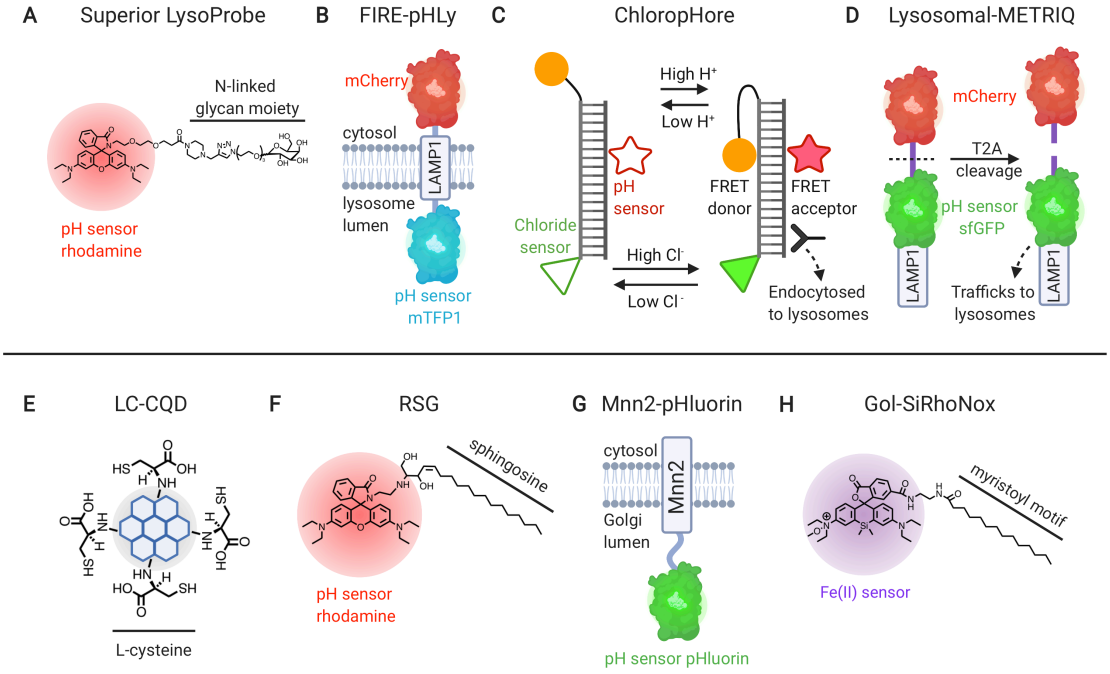

Figure 1.5. Examples of lysosome- and Golgi-targeted probes.
(A) Superior LysoProbe, pH-sensitive rhodamine conjugated with N-linked glycan moieties for improved lysosomal targeting; Chen et al., 2015. (B) FIRE-pHLy, ratiometric pH sensor chimera with cyan fluorescent protein, mTFP1, and LAMP1 for targeting; Chin et al., 2020. (C) ChloropHore, DNA-based dual-ion reporter for lysosomal pH (FRET-induced) and intraluminal chloride; Leung et al., 2019. (D) Lysosomal-METRIQ, self-cleaving ratiometric probe for membrane trafficking and lysosomal integrity; Ishii et al., 2019. (E) L-cysteine carbon quantum dots (LC-CQD) with functionalized cysteines for Golgi anchoring; R. S. Li et al., 2017. (F) Rhodamine-sphingosine (RSG), pH sensor conjugated with lipid sphingosine for Golgi recognition; Fan et al., 2019. (G) Mnn2-pHluorin, green fluorescent protein pH sensor targeted to Golgi membranes; Deschamps et al., 2020. (H) Gol-SiRhoNox, Fe(II) sensor with myristoyl motif for Golgi targeting; Hirayama et al., 2019. Created with BioRender.com.

GOLGI

Golgi structure, function, and disease relevance

The Golgi consists of interconnected stacks of flattened cisternae membranes that are responsible for packaging, processing and sorting molecular cargoes (lipids and proteins) to various cellular destinations. The Rab GTPases play master regulatory roles in cargo selection, transport, and membrane fusion events. Newly synthesized cargoes undergo anterograde trafficking from ER to the Golgi, where they are shuttled through the stacks, modified by enzymes, and exported. Golgi matrix and tethering proteins ensure proper structural integrity and movement through the Golgi, respectively. Retrograde Golgi-to-ER trafficking is also essential for retrieving ER export factors and Golgi soluble *N*-ethylmaleimide-sensitive factor attachment protein receptors (SNAREs) that allow for the fusion between membranes. The balance of inward and outward membrane trafficking maintains normal ER and Golgi functions. Stressors such as temperature, osmotic shock and drugs can disrupt this balance, causing the Golgi to collapse into the ER and resulting in cell death (Hicks and Machamer, 2005; Spang, 2013).

Golgi structure dynamically disassembles and reassembles during mitosis **(Fig. 1.6A)**. Golgi dysregulation causes fragmentation or dispersal of the Golgi, a common disease phenomenon (Hicks and Machamer, 2005; Li et al., 2019). In neurodegenerative disorders, Golgi

fragmentation is promoted by diverse molecular mechanisms. In early-stage AD, amyloid-beta peptides disrupt Golgi reassembly stacking proteins (Joshi et al., 2014, 2015). In PD, alpha-synuclein aggregation interferes with anterograde trafficking (Lashuel and Hirling, 2006). Finally in ALS, secretory vesicle trafficking is impaired (Atkin et al., 2014; Soo et al., 2015). Dysregulation of Golgi is also found in cancer, with mechanisms including aberrant glycosylation, overactivated Rab proteins, and elevated expression of Golgi-signaling kinases (Petrosyan, 2015). However, despite numerous examples of Golgi dysfunction, the relationship between Golgi morphofunction and disease remains unknown.

Phenotypic profiling of Golgi morphology using HCA methods

Since Golgi structure is complex and changes dynamically during healthy and disease states, the information captured by imaging Golgi is multidimensional. Image analysis has benefited from development of machine learning methods that allow images to be classified for different phenotypes even when these phenotypes have not been pre-defined **(Fig. 1.6B, C)**. The use of machine learning in Golgi HCA provides an instructive example of how these methods can be used for multiple organellar phenotypes.

Three studies utilized supervised machine learning to automatically classify Golgi phenotypes in a high-throughput fashion **(Fig. 1.6B)** (Chia et al., 2012; Galea and Simpson, 2013; Galea et al., 2015). Galea et al. developed a supervised machine learning methodology using GFP fused to GalNAc-T, a Golgi resident protein, to classify normal and damaged Golgi phenotypes based on multiple features such as area and number of fragments. These authors then applied this approach to screen RNAi in a kinetic assay to uncover synergies between retrograde trafficking regulators (Galea et al., 2015). They stimulated retrograde transport with brefeldin A and measured GalNAc-T distribution between ER and Golgi at three time points to define

retrograde transport rates. From this screen and further mechanistic experiments, the authors identified the critical roles of Rabs 1 and 6 in stimulating Golgi-ER trafficking.

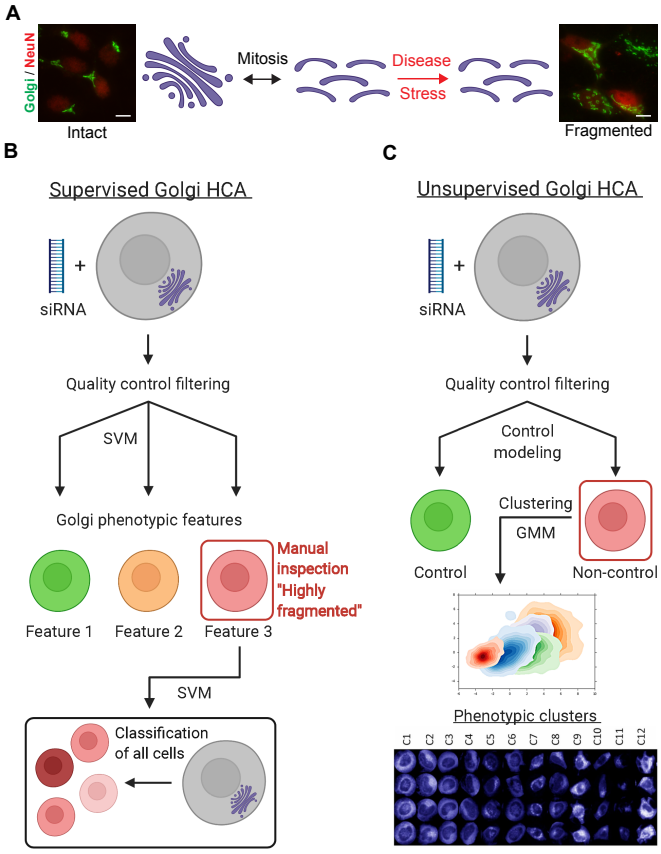

Figure 1.6. Golgi morphological states and HCA quantification methodologies.
(A) Schematic of Golgi structural dynamics during mitosis and disease or stress conditions. Images show representative intact and fragmented Golgi phenotypes (courtesy of Dr. Yanzhuang Wang, University of Michigan). Primary hippocampal neurons were treated with control or amyloid-beta peptides and stained for Golgi reassembly-stacking protein of 65 kDa, GRASP65 (green) and neuron marker, NeuN (red). Scale bars in all images, 10 µm. (B) Example of supervised Golgi HCA workflow (Galea and Simpson, 2013). Reference samples were chosen to manually pre-define Golgi phenotypes. Single vector machine (SVM), one type of machine learning algorithm, then developed a classification model based on whichever features distinguished the phenotypes from each other. The resulting model was then applied to new samples to quantify the presence of these phenotypes. (C) Example of unsupervised method to classify and cluster Golgi fragmentation phenotypes in siRNA gene knockdown cells (Hussain et al., 2017). Machine learning was applied on mock control cells to separate control-like and non-control-like states without pre-specifying phenotypes. Non-control-like phenotypes were then clustered according to a Gaussian mixture model (GMM), a probabilistic model that learns the differences between normally distributed but potentially overlapping subpopulations, i.e. one specific Golgi phenotype, within an overall population, i.e. all Golgi phenotypes. Created with BioRender.com.

Unsupervised machine learning may discover previously unrecognized Golgi fragmentation patterns **(Fig. 1.6C)**. Hussain et al. explored a diversity of Golgi morphologies, as extracted from GalNAc-T staining and analyzed using an unsupervised clustering framework

(Hussain et al., 2017). From this model, new Golgi phenotypes were described and protein-protein interactions were predicted based on related phenotypic signatures. For example, the SNARE proteins STX18, GOSR2, USE1, USO1, and STX5 were predicted to associate based on phenotypic similarity; these proteins had previously been shown to affect ER and Golgi trafficking (Dilcher et al., 2003; Shorter et al., 2002; Xu et al., 2000), and were predicted to form physical complexes (Hussain et al., 2017). Thus, unsupervised clustering models described many additional Golgi phenotypes that were useful for uncovering new biological associations.

Golgi probes with improved targeting and functionality

Small molecule probes targeting Golgi typically contain fluorophores conjugated to sphingolipids that concentrate in the Golgi during trafficking and metabolism. For example, 7-nitrobenz-2-oxa-1,3-diazole (NBD)-ceramide and BODIPY-ceramide dyes are used for imaging Golgi in live cells. However, because ceramide analogs can localize to other compartments of the cell, more specific Golgi-targeted probes are needed. Recent probes have focused on improving Golgi-targeting while others use a combination of targeting and biosensor groups to simultaneously measure Golgi function.

L-cysteine provides a novel Golgi targeting mechanism inspired by the cysteine-dependent anchoring of abundant Golgi resident proteins (Aoki et al., 1992; Maeda et al., 2001). Aoki et al. first demonstrated that cysteine residues within the membrane-anchoring domain of galactosyltransferase are required for Golgi retention. Similarly, Maeda et al. reported that protein kinase D, a key regulator of Golgi vesicle dynamics, is also recruited to the Golgi network via its cysteine-rich domain. Applying this concept, Li and colleagues designed an L-cysteine carbon quantum dot (LC-CQD) nanoprobe that targeted Golgi **(Fig. 1.5E)**. LC-CQDs significantly improved Golgi localization compared to D-cysteine-CQDs, indicating that cysteine

chirality strongly influenced targeting capability. Other advantages of the probe included high brightness and excellent photostability. Cells incubated with LC-CQD could be imaged continuously for one hour, which was six times longer than the fluorescence of BODIPY-ceramide or genetically encoded N-acetylgalactosaminyltransferase-GFP (Li et al., 2017).

Functional probes have been developed to measure Golgi luminal pH. Fan et al. developed a small molecule probe that monitored changes in Golgi acidification in both live cells and *in vivo* settings. The fluorescence probe, termed RSG, was composed of Golgi-targeting sphingosine conjugated to pH-sensitive rhodamine spirolactam **(Fig. 1.5F)** (Fan et al., 2019). Another Golgi pH sensor was synthesized by Deschamps et al. The genetically encoded probe was composed of a fusion between pHluorin, a pH-sensitive GFP-based sensor, and Mnn2, a Golgi membrane-associated enzyme **(Fig. 1.5G)**. Golgi pH varies along the stack to govern normal protein glycosylation (Kellokumpu et al., 2002), changing from pH 6.7 near the ER (*cis*) to 6.0 near the plasma membrane (*trans*) (Paroutis et al., 2004). The pHluorin probe was used to map *cis*- and *medial*-Golgi pH and to differentiate the roles of yeast V-ATPase subunits (Deschamps et al., 2020). Since defects in Golgi pH are linked to cancer and cystic fibrosis, among other diseases (Rivinoja et al., 2012), screening for compounds that modulate Golgi pH could yield important chemical probes and new drug targets.

One group developed an iron-sensitive probe with the goal of elucidating the emerging role of Golgi in iron metabolism. Iron homeostasis is crucial for controlling oxidative damage of labile, or unbound, Fe(II) in the cell. Furthermore, missorting of the iron transporter DMT1 is linked to neurodegenerative diseases (Belaidi and Bush, 2016). Using their previously developed Fe(II)-specific chemical switch, Hirayama and colleagues synthesized Gol-SiRhoNox to measure labile Fe(II) Golgi pools. Gol-SiRhoNox consisted of a myristoyl motif to aid in Golgi targeting

and a silicon-fused rhodamine modified with *N*-oxide that fluoresced after Fe(II)-mediated cleavage **(Fig. 1.5H)** (Ishida et al., 2013). Gol-SiRhoNox measured Fe(II) distribution in protein-sorting deficient systems. While Fe(II) distribution was normally Golgi dominant, deletion of the protein-sorting machinery shifted Fe(II) and DMT1 localization to lysosomes. However, rescue by a molecular chaperone led to redistribution of DMT1 and Fe(II) to the Golgi (Hirayama et al., 2019).

Anterograde trafficking from ER to Golgi can be challenging to study because anterograde and retrograde transport occur in tandem. Boncompain and colleagues have built an innovative system called Retention Using Selective Hook (RUSH) to synchronize transport of a protein cargo by controlling its release from a donor compartment, e.g., ER (Boncompain et al., 2012). The RUSH system uses two fusion proteins. One fusion protein includes streptavidin attached to a signal sequence "hook" that localizes streptavidin to the donor compartment; the second fusion protein contains cargo fused to a fluorescent protein and a streptavidin-binding peptide (SBP). The fluorescent cargo is held in the donor compartment by SBP binding to streptavidin. When biotin is added to cells, SBP is released and the cargo traffics normally to the acceptor compartment, thus allowing imaging of uni-directional protein trafficking. The RUSH assay was adapted to screen for small-molecule regulators of anterograde trafficking in HeLa cells (Boncompain et al., 2019). In this screen, ManII, a Golgi glycosylase, was tagged with eGFP and SBP; streptavidin was fused with the ER-retention signal peptide KDEL as the hook. Upon treatment with biotin, ManII was released and transported to the Golgi acceptor compartment within thirty minutes. From a library of 640 FDA-approved drugs, two epithelial growth factor receptor (EGFR) inhibitors, BML-265 and Tyrphostin AG1478, caused cargo to remain in the ER; these effects were reversible when the compound was removed. Both

compounds also inhibited anterograde trafficking of EGFR to prevent its localization on the cell surface, which has clinical implications in cancer (Tomas et al., 2014).

Prospect of Golgi phenotypic discovery

Golgi phenotypic discovery is being accelerated by powerful HCA techniques, which allow visualization of the complex relationship between Golgi structure, dynamics, and trafficking. Additionally, innovative probes that achieve better Golgi specificity and the ability to sense pH and Fe(II) provide ripe opportunities for phenotypic screening.

MEMBRANELESS ORGANELLES

Membraneless organelles (MLOs) structure, function, and disease relevance

Membraneless organelles (MLOs) are non-membrane-bound subcellular compartments that perform specialized biochemical functions (Crabtree and Nott, 2018) (**Fig. 1.7A, B**). MLOs exist in both the nucleus and cytoplasm as liquid foci caused by liquid-liquid phase separation (LLPS) of specific RNAs and proteins (Alberti et al., 2019; Boeynaems et al., 2018; Chong et al., 2018; Weber and Brangwynne, 2012). MLOs play various roles in RNA processing, ribonucleoprotein (RNP) assembly, and cellular stress response (Anderson and Kedersha, 2002; Chang et al., 2018; Fan and Leung, 2016; Galganski et al., 2017; Kimball et al., 2003; Lafarga et al., 2016; Lallemand-Breitenbach and de Thé, 2010; Luo et al., 2018; Morris, 2008; Pederson, 2011; Spector and Lamond, 2011; Tripathi et al., 2012; Waris et al., 2014). They are also highly dynamic structures; in many cases, proteins and RNAs exchange with MLOs on the seconds-minutes time scale, allowing these bodies to respond quickly to changes in cell state (Chang et al., 2018; Moon et al., 2019). A summary of the different MLOs, their functions, constituents,

and detection probes can be found in **Table 1.2**. Interest in MLOs for chemical biology and drug discovery has dramatically increased in the past five years, and methodologies for visualizing MLOs were recently reviewed (Mitrea et al., 2018). Due to their small size (~0.1 - 5 μm) and highly dynamic nature, these structures are the vanguard for design of functional HCA probes and high-throughput phenotypic screens.

Given the important roles of MLOs in cellular homeostasis, perturbations in organellar constituents could affect their function and dynamics, leading to progression of diseases such as ALS and cancer. For instance, promyelocytic leukemia nuclear bodies (PML-NBs) contain ca. 30 proteins, including tumor suppressors (p53, PML), DNA repair factors, and apoptotic inducers. PML-NBs are often down-regulated in cancer, suggesting a resistance to DNA damage-mediated cell death and apoptosis (Chang et al., 2018; Guan and Kao, 2015; Gurrieri et al., 2004; Lallemand-Breitenbach and de Thé, 2010; Reineke and Kao, 2009). Stress granules (SGs) are another MLO that form in the presence of a wide array of cellular stresses, and contain translationally stalled mRNA and stalled 48S preinitiation complexes (Anderson and Kedersha, 2002; Fan and Leung, 2016; Kimball et al., 2003; Waris et al., 2014). In ALS, patient cells have been found to contain mutant fused in sarcoma (FUS) and/or mutant TAR-DNA binding protein of 43 kDa (TDP-43) in SGs. This recruitment may impact cellular defense mechanisms and lead to disease progression (Baron et al., 2013; Wolozin and Ivanov, 2019). Mutations of FUS and TDP-43 occur in low-complexity domains, protein regions with a low diversity of amino acid composition, perhaps leaving them more vulnerable to self-association and phase-separation (Conicella et al., 2016; Elbaum-Garfinkle, 2019; Murakami et al., 2015).

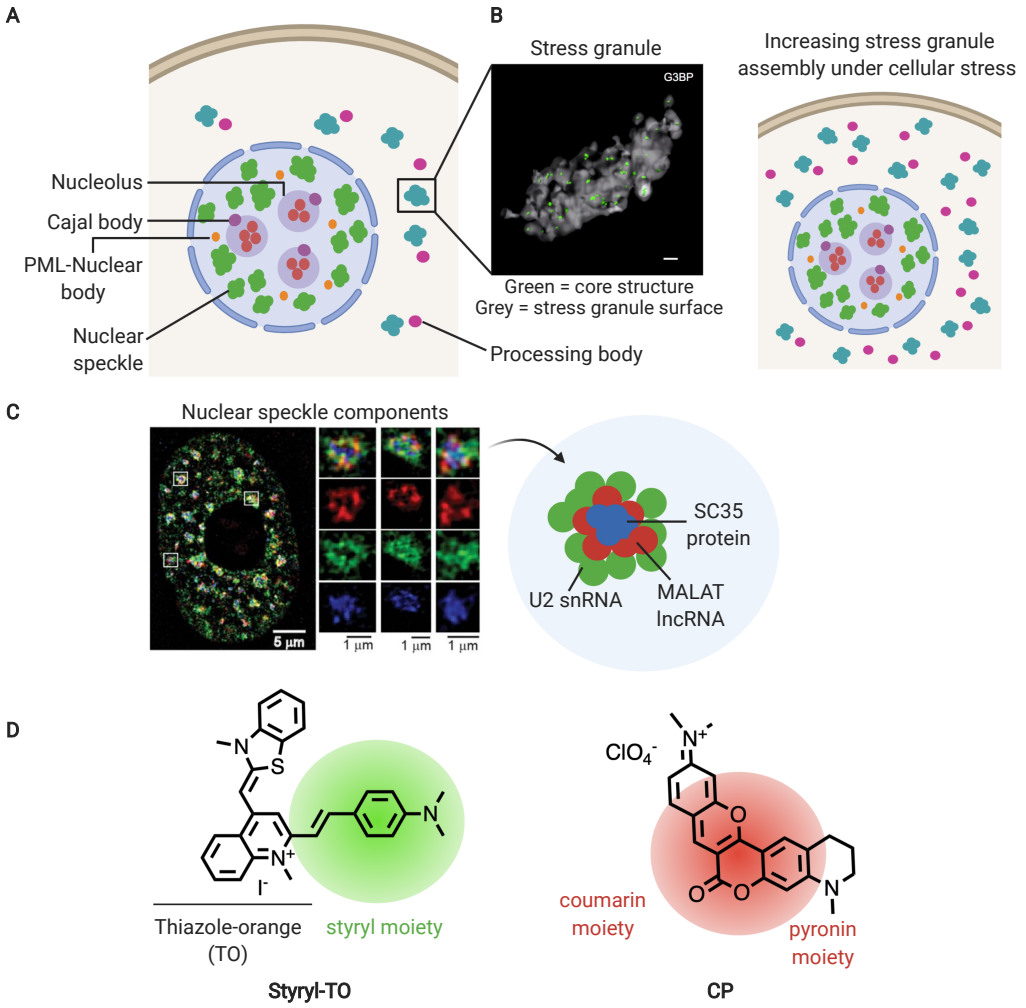

Figure 1.7. Membraneless organelle (MLO) localization, function, and organization examples.
(A) Schematic diagram of MLOs. (B) Three-dimensional stochastic optical reconstruction microscopy (STORM) of stress granule (SG) with green dots showing the area with high G3BP protein concentration (core) and grey surface showing area with less concentrated material (granule shell), scale bar: 500 nm. SG assembly increases in response to cellular stress. (C) Structured illumination microscopy (SIM) of nuclear speckle components. Three speckles confined in white squares were enlarged for better visualization, revealing spatial organization of U2 snRNAs, MALAT long noncoding RNAs (lncRNAs), and SC35 proteins. STORM and SIM images were adapted from (Jain et al., 2016) and (Fei et al., 2017), respectively, with permissions. (D) Example of small molecule probes for nucleoli rDNA detection: A thiazole orange (TO)-based dye with a styryl substituent (Styryl-TO), and for rRNA detection: hybridized coumarin and pyronin moieties (CP) (Liu et al., 2015; Lu et al., 2016). Colors represent dyes' emission wavelengths. See also **Table 1.2**. Created with BioRender.com.

MLO-based screening

Two of the drivers for HCA technology development for MLOs are their associations with disease pathology and their novel properties compared to membrane-bound organelles. Due to their small size and complex dynamics, MLOs require careful image analysis protocols

(Caragine et al., 2019; He et al., 2018; Major et al., 2017). Here, we highlight a few imaging-based screening studies that either show relevance of MLOs in chemical biology/drug discovery or employ advanced imaging techniques. These screens use structural probes, including fluorescence *in situ* hybridization (FISH) to identify RNAs (Jain et al., 2016; Wang et al., 2019), and immunofluorescence or FP fusions to monitor proteins in MLOs (Marrone et al., 2018; Platani et al., 2000). Of these three methods, only genetically encoded fusion proteins are amenable to live-cell screening.

Yip et al. developed a phenotypic screening assay to identify compounds that induced PML-NBs formation as an anticancer strategy (Yip et al., 2011). They noted that the beneficial effects of interferon (INF) and arsenical (As_2O_3) treatments in cancer are due to PML-NB formation, but their high toxicities dampen their effectiveness as anticancer treatments. The authors hypothesize that compounds inducing PML-NB formation directly would restore the tumor suppressor activity of PML with lower toxicity. For the screen, PML-NBs were visualized by immunofluorescence staining of PML protein in fixed HeLa cells and were identified as stained puncta within the nucleus. A library of 1280 drugs and a pooled combinatorial library containing millions of compounds were screened, using IFN-gamma as a positive control. Additionally, since DNA-damaging agents upregulate PML-NBs, markers for direct DNA damage (phosphorylated H2AX histone and phosphorylated Chk1 kinase) were included as counter screens. The high-content screen of the combinatorial library identified N-methyl triamine-containing compounds that induced PML-NB formation without causing phosphorylation of H2AX and Chk1. This early example of an HCA screen for MLOs also demonstrated the feasibility of counting these small objects in high throughput.

As noted above, the recruitment of FUS to SGs is associated with impaired stress responses in ALS. Disease-causing mutations such as P525L in the nuclear localization signal (NLS) of FUS are particularly prone to SG recruitment (Marrone et al., 2018). To discover drugs and mechanisms to reduce FUS localization to SGs, Marrone et al. developed HCA assays in iPSCs and iPSC-derived motor neurons using fusion proteins containing eGFP fused to wild-type (wt) or P525L-FUS. These FUS-eGFP fusions were added via CRISPR/Cas9 gene-editing, leading to near-wild-type expression levels. Under stress, SGs containing P525L-FUS-eGFP appeared larger and brighter than granules containing wtFUS-eGFP, indicating an impairment in SG dynamics. Screening 1600 existing drugs in P525L-FUS-eGFP cells identified several autophagy inducers, including rapamycin and known CNS-active drugs, that minimized size, number, and intensity of mutant SGs. Interestingly, the authors showed that fewer than 5% of SGs co-stained for the autophagy marker LC3, suggesting that FUS-eGFP itself, rather than FUS-eGFP-containing SGs, were degraded by autophagy. This conclusion was in agreement with one published study (Ganassi et al., 2016), and in contrast to another one that found colocalization of autophagosomes and FUS+ SGs (Ryu et al., 2014). In addition to the biological insight provided by this screen, several technical features are noteworthy. This manuscript appears to be the first to report an HCA screen measuring endogenous SGs in live iPSCs and motor neurons. Also, adding fluorescent fusions into the endogenous locus of the protein-of-interest via gene editing allowed wild-type regulation and expression. This study thus represents a significant advancement towards the goal of measuring membraneless organelle function and dynamics in human-relevant cell models.

Nuclear speckles are among the most complex MLOs; they are involved in mRNA processing and contain hundreds of proteins and RNAs. Remarkably, Fei et al. demonstrated

sub-organellar spatial organization (Fei et al., 2017) within the nuclear speckle using single-molecule FISH (smFISH) and immunofluorescence, coupled with superresolution microscopy (SIM) (**Fig. 1.7C**). Furthermore, Wang et al. used FISH technology to develop an imaging-based pooled-CRISPR screening methodology to identify proteins that modulated localization of long noncoding RNA (lncRNA) to nuclear speckles (Wang et al., 2019). They used lentiviral transfection to co-deliver bar-coded single guide RNAs (sgRNAs) targeting potential regulatory RNA-binding proteins and a FISH-based reporter for the lncRNA of interest. They then performed single-cell, multiplex error-robust FISH (MERFISH) to read the barcodes of the corresponding sgRNA that induced or inhibited recruitment of the lncRNA into the nuclear speckles. To demonstrate the potential of this technology, they screened 162 sgRNAs targeting 54 RNA binding proteins and successfully identified known positive and negative regulators of the lncRNA MALAT1. Two of these RNA-binding proteins, heterogeneous nuclear (hn)RNPH1 and hnRNPK, were also shown to affect localization of other nuclear speckle constituents such as U2 small nuclear (sn)RNA, poly-A-containing RNAs, preribosomal RNA, and MRP, suggesting that perturbations of hnRNP genes could lead to abnormal nuclear speckle formation.

Interestingly, a few studies have shown that different MLOs work together in processing RNAs and RNPs. For example, assembled snRNPs are transported from Cajal bodies to nuclear speckles for protein modification, and mRNAs are transported from SGs to processing bodies (p-bodies) for degradation (Fan and Leung, 2016; Morris, 2008). Other linkages between MLOs are yet to be discovered. Using pools of siRNAs targeting 1354 human genes, Berchtold et al. developed a multiplexed HCA platform to immunostain six different MLOs and identified genes regulating MLO formation, as well as shared regulatory pathways (Berchtold et al., 2018). For example, down-regulation of cAMP phosphodiesterases increased the number of p-bodies, while

cAMP-dependent protein kinase (PKA) was required for formation of Cajal bodies. Furthermore, genes regulating nucleolar morphology were also found to be involved in splicing-related functions of nuclear speckles. This finding was in agreement with previous studies where follicular cells with a mutation in a splicing factor gene SRRM2 exhibited smaller nucleoli (Policarpio-Nicolas and Sirohi, 2013; Tomsic et al., 2015). Thus, MLOs are not only highly dynamic organelles, but also form a complex network for RNA and protein processing in the cell.

Development of MLO-targeted probes

Fluorescent probe development for MLOs is rapidly expanding. Small-molecule fluorophores and RNA sensors for live-cell applications will offer advantages and complementarity to current methods for high-content and high-throughput applications.

To our knowledge, chemical probes targeting MLOs have so far only been demonstrated for ribosomal (r)DNA and rRNA detection (**Fig. 1.7D**). Several reported dyes, however, suffer from poor photostability, selectivity, and/or cell permeability (Li et al., 2006, 2013; Song et al., 2014). A thiazole orange (TO)-based dye with a styryl substituent creates a highly selective probe called styryl-TO that intercalates into the G-quadruplex structures of rDNA in live PC3 cells (Lu et al., 2015, 2016). The probe exhibits high rDNA-to-dsDNA selectivity due to its styryl moiety. The deep red fluorescence probe CP and a naphthalimide dye called probe 1 are also demonstrated to have good rRNA-to-DNA selectivity, photostability, and compatibility with live-cell imaging (Cao et al., 2019; Liu et al., 2015; Zhou et al., 2015). Both CP and probe 1 bind to rRNA through hydrophobic interactions. CP has been used to monitor live nucleoli dynamics prior, during, and after mitosis in HeLa cells (Zhou et al., 2015). As reported by other studies (Dundr et al., 2000; Leung et al., 2004), nucleoli were found distorted and reduced in size, finally

disappearing during mitosis and reassembling during telophase. This study exemplified the potential of small-molecule probes to monitor MLO dynamics.

Advanced RNA-detection methodologies, largely focused on single-molecule detection, have generated deep insight into RNA dynamics in MLOs and provide an exciting opportunity for live-cell HCA for screening applications. These probes were very recently reviewed (Braselmann et al., 2020). Briefly, approaches include fluorescent-protein fusions with RNA-binding proteins, molecular beacons, and dye-binding RNA-based aptamers. Aptamers are nucleic acid sequences that are selected for binding to particular targets. Since Jaffrey and co-workers described aptamers that bind to small-molecule dyes (Filonov et al., 2014; Paige et al., 2011), several groups have developed genetically-encoded RNA sensors that bind to cell-permeable dyes in live cells (Cawte et al., 2020; Yatsuzuka et al., 2018). As a recent example, Cawte et al. used a FRET-based aptamer fused to a reporter mRNA to demonstrate detection of single mRNA molecules in MLOs called paraspeckles.

Prospects for MLOs phenotypic discovery

MLO-based screens have focused on structure and composition. Emerging small-molecule and RNA-based probes could enable high-throughput screening platforms in live cells to visualize dynamic readouts such as rates of organelle fusion, trafficking, and colocalization of RNAs and proteins on a much larger scale. Both the biology and technology to study MLOs are rapidly co-evolving.

OUTLOOK

Phenotypic screening has become increasingly prevalent as a means to identify active small molecules in human-relevant disease models. However, after primary screening,

determining a compound's mechanism of action often becomes a major obstacle; approaches that accelerate this process are needed. Looking forward, organellar-based phenotypic discovery may fill this gap by incorporating higher specificity of mechanistic information, while maintaining clinically-relevant cellular phenotypes in assay design. Exciting new developments are on the horizon with the emergence of improved chemical and genetically encoded probes for organelles. Effective designs target probes to specific organelles - and even suborganellar compartments - while measuring organelle-specific functions. By combining newer generations of functional probes with powerful HCA and patient-derived cells, future HTS studies have the capacity to generate large amounts of disease-relevant multi-parametric data that can be explored to identify not only new molecular targets but also therapeutic leads for drug discovery.

SIGNIFICANCE

Organelles are defined cellular compartments, each with its own unique structure and function. Past technologies were tremendously useful in elucidating these properties; however, as our understanding of organellar functions and dynamics deepens, so will the need to develop more specific tools. As exemplified in this review, organelles are not static structures – mitochondria undergo fusion and fission, lysosomes traffic to and from the nucleus, Golgi disperses and reforms during mitosis and stress, and MLO constituents assemble rapidly in response to different cellular states. Specific probes are enabling accurate labeling of organelles and even suborganellar structures, and will allow for multiplexed measurements of organelle systems. Recently, there has been an emphasis on organelle-specific screens using primary and patient-derived cells that recapitulate the cellular contexts of disease, promising better translation from bench to clinic. Taken together, organellar phenotypic discovery is brimming with novel probes and technologies that are only just being applied to HTS platforms. In this review, we

introduced several key organelles where we see active and innovative phenotypic discovery with emphasis on tool development and HTS case studies.

TABLES

Table 1.1. Summary of organelle detection probes.

	Probe type	Targeting strategy	Structure-based?	Function-based?	Live/Fixed conditions?	Dynamic/Endpoint?	Cell toxicity?	Reference(s)
MITOCHONDRIA								
TMRM	small molecule	electrostatic interaction with polarized ΔΨ	No	Yes	Live	Dynamic	Yes	(Elmore et al., 2004)
ECPI-12	small molecule	lipophilic interactions with MIM	Yes	No	Live	Dynamic	No*	(Zhang et al., 2019)
MitoTracker	small molecule	irreversible binding to thiol groups in MIM	Yes	No	Live	Endpoint	Yes	(Chazotte, 2011)
SYBR Gold	small molecule	direct mtDNA binding	Yes	No	Both	Dynamic	No	(Jevtic et al., 2018)
RSL+	small molecule	direct binding to mitochondrial ATP	No	Yes	Live	Dynamic	N/R**	(de la Fuente-Herreruela et al., 2017)
ATeam	genetically encoded	fused to mitochondrial targeting sequence of COX VIII	No	Yes	Live	Dynamic	No	(Imamura et al., 2009)
MitoSox Red	small molecule	reacts with superoxide	Yes	No	Live	Endpoint	Yes	(De Biasi et al., 2016)
LYSOSOMES								
LysoTracker	small molecule	ion trapping/lysosomotropism	Yes	No	Both	Dynamic	Yes	(Pugach et al., 2018; Xu et al., 2014; Zhang et al., 1994)
Superior LysoProbes	small molecule	functionalized with N-linked glycan moieties	Yes	Yes	Live	Dynamic	No	(Chen et al., 2015)
(RpH)-LAMP1-3xFLAG	genetically encoded	fused to LAMP1	No	Yes	Both	Dynamic	No	(Ponsford et al., 2020)
pHLARE	genetically encoded	fused to LAMP1	No	Yes	Both	Dynamic	No	(Webb et al., 2020)
FIREpHLy	genetically encoded	fused to LAMP1	No	Yes	Both	Dynamic	No	(Chin et al., 2020)
ChloropHore	DNA-based	trafficked to lysosomes via scavenger receptors	No	Yes	Live	Dynamic	N/R	(Leung et al., 2019)
Lysosomal METRIQ	genetically encoded	fused to lysosomal resident proteins (i.e. LAMP1, ASAH1, DNase IIα)	No	Yes	Both	Dynamic	No	(Ishii et al., 2019)
GOLGI APPARATUS								
GFP-GalNAc-T	genetically encoded	fused to GalNAc-T	Yes	No	Both	Dynamic	No	(Galea and Simpson, 2013; Galea et al., 2015)
NBD-Cer	small molecule	fluorophore-labeled ceramide	Yes	No	Both	Dynamic	Yes	(Lipsky and Pagano, 1985)
BODIPY-Cer	small molecule	fluorophore-labeled ceramide	Yes	No	Both	Dynamic	Yes	(Pagano et al., 1991)
LC-CQD	small molecule	anchoring in Golgi membranes via L-cysteine residues	Yes	No	Both	Dynamic	No	(Li et al., 2017)
RSG	small molecule	conjugated with sphingosine	No	Yes	Live	Dynamic	No	(Fan et al., 2019)
Mnn2-pHluorin	genetically encoded	fused with Mnn2	No	Yes	Both	Dynamic	No	(Deschamps et al., 2020)
Gol-SiRhoNox	small molecule	conjugated with myristoyl motif	No	Yes	Live	Dynamic	No	(Hirayama et al., 2019)
ManII-SBP-eGFP	genetically encoded	fused to ManII	No	Yes	Both	Dynamic	No	(Boncompain et al., 2012)
MEMBRANELESS ORGANELLES								
anti-PML	antibody	PML targeted	Yes	No	Fixed	Endpoint	N/A***	(Yip et al., 2011)

	Probe type	Targeting strategy	Structure based?	Function based?	Live/fixed conditions	Dynamic/ Endpoint	Cell toxicity?	Reference(s)
FUS-eGFP	genetically encoded	Added via CRISPR/Cas9 gene-editing, leading to near-wild-type expression level	Yes	No	Both	Dynamic	No	(Marrone et al., 2018)
CP	small molecule	rRNA targeted, hydrophobic group allows for nuclear permeability and crescent shape facilitates molecular docking	Yes	No	Both	Dynamic	No	(Liu et al., 2015; Zhou et al., 2015)
Probe1 (naphthalimide dye)	small molecule	rRNA targeted, molecular docking by hydrophobic interactions and hydrogen bonds	Yes	No	Both	Dynamic	No	(Cao et al., 2019)
Styryl-TO	small molecule	rDNA G-quadruplexes intercalator	Yes	No	Both	Dynamic	N/R	(Lu et al., 2015, 2016)
Mango II aptamer (M2x24)	genetically encoded	Single mRNA transcript tagging	Yes	No	Both	Dynamic	N/R	(Cawte et al., 2020)

*No = reported no toxicities under the conditions of this study; **N/R = not reported; ***N/A = not applicable.

Table 1.2. Membraneless organelles (MLOs) functions and detection probes.

Membraneless Organelles (MLOs)	Functions	Major Scaffolding Constituents and Available Detection Probes*	Ref.
Nucleolar MLOs			
Nucleolus	Ribosomal RNA synthesis, signal recognition particle (SRP) RNA synthesis	*Proteins* **Fibrillarin (FBL): m-Cerulean/GFP/Ab**, **NPM1: DsRed/RFP**, **Nucleolin (NCL): Ab**, **B23: Ab**, UBTF, UTP6, RPF1, and Nop56 *Chemical probes for RNA detection* **SYTO RNASelect, NUCLEOLAR-ID**, **Styryl dyes: E36/PY/IN**, **Neainfra-red dyes: Hsd/Hsd-CB7**, **Crescent-shape dye: CP**, **Naphthalimide dye: Probe 1**, **Ligand integrated dye: Styryl-TO**, **Two-photon excited fluorescence (TPEF) dye: DBF**, and **Carbon dots**	(Brangwynne et al., 2011; Cao et al., 2019; Caragine et al., 2019; He et al., 2018; Li et al., 2006, 2013; Lu et al., 2015; Pederson, 2011; Shishova et al., 2011; Song et al., 2014; Zhou et al., 2015)
Cajal body	Small nuclear ribonucleoproteins (snRNP) assembly, small nucleolar (sno)RNA metabolism, and post-transcriptional modification of spliceosomal U small nuclear (sn)RNAs	*Proteins* **SMN complex (gemin1-8 and unr interacting protein): GFP/Ab**, **Coilin: GFP/Ab**, and WRAP53β	(Bergstrand et al., 2019; Dundr et al., 2004; Morris, 2008; Platani et al., 2000)
Nuclear speckle	snRNP modification and storage, gene transcription, regulation of pre-mRNA alternative splicing, i.e. phosphorylation, cellular distribution, splicing activity	*RNA* **MALAT1: smFISH** and **U1**, **U2: smFISH** *Proteins* **SC35: eYFP/Ab**, **U2B": YFP/Ab**, and **SON: Ab**	(Fei et al., 2017; Galganski et al., 2017; Spector and Lamond, 2011; Tripathi et al., 2012)
PML nuclear body	Tumor suppressor, sensing DNA damage, DNA repair, apoptosis, stem cell renewal, telomere elongation	*Proteins* **SUMOylated PML isoforms: GFP/Ab**	(Guan and Kao, 2015; Guo et al., 2000; Gurrieri et al., 2004; Hoischen et al., 2018)
Paraspeckle	RNA retention in nucleus, defense against viral infection	*RNA* **NEAT1: smFISH/ Mango aptamer** *Proteins* **PSPC1: YFP/Ab**, **NONO: eGFP/Ab**, **SFPQ: Ab**, FUS, HNRNPK, HNRNPH3, DAZAP1, and RBM14	(Bond and Fox, 2009; Cawte et al., 2020; Fox and Lamond, 2010; Fox et al., 2018; Wang et al., 2018)
Nuclear stress body	Defense against cellular stresses	*RNA* **satellite III (Sat III): biotinylated antisense oligonucleotide** *Proteins* **HSF1: Ab**, HSF2, SAFB, Sam68, and SRSF	(Biamonti, 2004; Chatterjee et al., 2019)
Histone locus body	Histone mRNA biosynthesis	*Proteins* **FLICE-associated huge (FLASH): Ab**, **NPAT: Ab**, **and Mxc: GFP/Ab** *RNA-protein complexes* U7 snRNP	(Duronio and Marzluff, 2017; Kurihara et al., 2020)
Cytoplasmic MLOs			
Stress granule	Storage of translationally stalled mRNA, defense against cellular stresses	*Proteins* **FUS: eGFP/Ab**, **G3BP: GFP/mRFP/Ab**, **TIA: GFP/mRFP**, TDP43, 48S preinitiation complexes (small ribosomal subunits and translation initiation factors, i.e. eIF2, eIF3, eIF4E, and eIF4G)	(Baron et al., 2013; Fan and Leung, 2016; Marrone et al., 2018; Waris et al., 2014)
Processing body	mRNA decay, storage of mRNA decay enzymes	*Proteins* **Lsm14A: GFP**, **Dcp1/ Dcp2: mCherry**, Ccr4-Not, Lsm1-7, Edc3, Edc4, Pat1, DDX6, and Xrn1	(Hubstenberger et al., 2017; Luo et al., 2018; Sachdev et al., 2019)

MLO(s)	Functions	Major Scaffolding Constituents and Available Detection Probes*	Ref.
Germ granule	mRNA translation regulation in germ cells	*RNA* Nanos *Proteins* **PGL-1: GFP/RFP/SNAP-tag**, PGL-3, MEG-3, MEG-4, **Vasa and related DEAD box RN, helicases(GLH-1 to 4): GFP/Ab**, Argonaute family (Aubergine, PIWI), Tudor domain proteins, and Nanos	(Aoki et al., 2019; Lev et al., 2019; Trcek and Lehmann, 2017; Voronina et al., 2011)

*Bolded text represents MLOs constituents with available detection probes.

ACKNOWLEDGEMENTS

We would like to thank Dr. Yanzhuang Wang and his laboratory (University of Michigan) for providing immunofluorescence images for Figure 1.6A. This work was supported by R01 (M.C., M.R.A.) and the University of California National Laboratories, Office of the President and GlaxoSmithKline (J.A.E., G.P., S.M., M.R.A.).

AUTHOR CONTRIBUTIONS

M.Y.C, J.A.E., G.P., S.M., and M.R.A. wrote and edited the manuscript.

DECLARATION OF INTERESTS

The authors declare no competing interests.

REFERENCES

1. Alberti, S., Gladfelter, A., and Mittag, T. (2019). Considerations and challenges in studying liquid-liquid phase separation and biomolecular condensates. Cell *176*, 419–434.
2. Aleo, M.D., Luo, Y., Swiss, R., Bonin, P.D., Potter, D.M., and Will, Y. (2014). Human drug-induced liver injury severity is highly associated with dual inhibition of liver mitochondrial function and bile salt export pump: ALEO ET AL. Hepatology *60*, 1015–1022.
3. Anderson, P., and Kedersha, N. (2002). Stressful initiations. J Cell Sci *115*, 3227–3234.
4. Aoki, D., Lee, N., Yamaguchi, N., Dubois, C., and Fukuda, M.N. (1992). Golgi retention of a trans-Golgi membrane protein, galactosyltransferase, requires cysteine and histidine residues within the membrane-anchoring domain. PNAS *89*, 4319–4323.
5. Appelqvist, H., Wäster, P., Kågedal, K., and Öllinger, K. (2013). The lysosome: from waste bag to potential therapeutic target. Journal of Molecular Cell Biology *5*, 214–226.
6. Archer, S.L. (2013). Mitochondrial Dynamics — Mitochondrial Fission and Fusion in Human Diseases. N Engl J Med *369*, 2236–2251.
7. Atkin, J.D., Farg, M.A., Soo, K.Y., Walker, A.K., Halloran, M., Turner, B.J., Nagley, P., and Horne, M.K. (2014). Mutant SOD1 inhibits ER-Golgi transport in amyotrophic lateral sclerosis. J. Neurochem. *129*, 190–204.
8. Banach-Latapy, A., He, T., Dardalhon, M., Vernis, L., Chanet, R., and Huang, M.-E. (2014). P37 - Monitoring dynamic changes of glutathione redox state in subcellular compartments of human cells – an approach based on rxYFP biosensor. Free Radical Biology and Medicine *75*, S33.

9. Baron, D.M., Kaushansky, L.J., Ward, C.L., Sama, R.R.K., Chian, R.-J., Boggio, K.J., Quaresma, A.J.C., Nickerson, J.A., and Bosco, D.A. (2013). Amyotrophic lateral sclerosis-linked FUS/TLS alters stress granule assembly and dynamics. Molecular Neurodegeneration *8*, 30.

10. Belaidi, A.A., and Bush, A.I. (2016). Iron neurochemistry in Alzheimer's disease and Parkinson's disease: targets for therapeutics. Journal of Neurochemistry *139*, 179–197.

11. Berchtold, D., Battich, N., and Pelkmans, L. (2018). A Systems-Level Study Reveals Regulators of Membrane-less Organelles in Human Cells. Molecular Cell *72*, 1035-1049.e5.

12. Bi, X., and Liao, G. (2010). Cholesterol in Niemann–Pick Type C disease. Subcell Biochem *51*, 319–335.

13. Boeynaems, S., Alberti, S., Fawzi, N.L., Mittag, T., Polymenidou, M., Rousseau, F., Schymkowitz, J., Shorter, J., Wolozin, B., Van Den Bosch, L., et al. (2018). Protein Phase Separation: A New Phase in Cell Biology. Trends Cell Biol *28*, 420–435.

14. Boncompain, G., Divoux, S., Gareil, N., de Forges, H., Lescure, A., Latreche, L., Mercanti, V., Jollivet, F., Raposo, G., and Perez, F. (2012). Synchronization of secretory protein traffic in populations of cells. Nat Methods *9*, 493–498.

15. Boncompain, G., Gareil, N., Tessier, S., Lescure, A., Jones, T.R., Kepp, O., Kroemer, G., Del Nery, E., and Perez, F. (2019). BML-265 and Tyrphostin AG1478 Disperse the Golgi Apparatus and Abolish Protein Transport in Human Cells. Front Cell Dev Biol *7*.

16. Braselmann, E., Rathbun, C., Richards, E.M., and Palmer, A.E. (2020). Illuminating RNA Biology: Tools for Imaging RNA in Live Mammalian Cells. Cell Chemical Biology *27*, 891–903.

17. Bulthuis, E.P., Adjobo-Hermans, M.J.W., Willems, P.H.G.M., and Koopman, W.J.H. (2019). Mitochondrial Morphofunction in Mammalian Cells. Antioxidants & Redox Signaling *30*, 2066–2109.

18. Caielli, S., Athale, S., Domic, B., Murat, E., Chandra, M., Banchereau, R., Baisch, J., Phelps, K., Clayton, S., Gong, M., et al. (2016). Oxidized mitochondrial nucleoids released by neutrophils drive type I interferon production in human lupus. Journal of Experimental Medicine *213*, 697–713.

19. Cao, C., Wei, P., Li, R., Zhong, Y., Li, X., Xue, F., Shi, Y., and Yi, T. (2019). Ribosomal RNA-Selective Light-Up Fluorescent Probe for Rapidly Imaging the Nucleolus in Live Cells. ACS Sens *4*, 1409–1416.

20. Caragine, C.M., Haley, S.C., and Zidovska, A. (2019). Nucleolar dynamics and interactions with nucleoplasm in living cells. ELife *8*, e47533.

21. Casey, J.R., Grinstein, S., and Orlowski, J. (2010). Sensors and regulators of intracellular pH. Nat Rev Mol Cell Biol *11*, 50–61.

22. Cawte, A.D., Unrau, P.J., and Rueda, D.S. (2020). Live cell imaging of single RNA molecules with fluorogenic Mango II arrays. Nature Communications *11*, 1283.

23. Chakraborty, K., Leung, K., and Krishnan, Y. (2017). High lumenal chloride in the lysosome is critical for lysosome function. ELife *6*, e28862.

24. Chandrasekharan, A., Varadarajan, S.N., Lekshmi, A., Lupitha, S.S., Darvin, P., Chandrasekhar, L., Pillai, P.R., Santhoshkumar, T.R., and Pillai, M.R. (2019). A high-throughput real-time in vitro assay using mitochondrial targeted roGFP for screening of drugs targeting mitochondria. Redox Biology *20*, 379–389.

25. Chang, H.R., Munkhjargal, A., Kim, M.-J., Park, S.Y., Jung, E., Ryu, J.-H., Yang, Y., Lim, J.-S., and Kim, Y. (2018). The functional roles of PML nuclear bodies in genome maintenance. Mutation Research/Fundamental and Molecular Mechanisms of Mutagenesis *809*, 99–107.

26. Chanséaume, E., and Morio, B. (2009). Potential Mechanisms of Muscle Mitochondrial Dysfunction in Aging and Obesity and Cellular Consequences. Int J Mol Sci *10*, 306–324.

27. Chazotte, B. (2011). Labeling Mitochondria with MitoTracker Dyes. Cold Spring Harbor Protocols *2011*, pdb.prot5648-pdb.prot5648.

28. Cheloha, R.W., Li, Z., Bousbaine, D., Woodham, A.W., Perrin, P., Volarić, J., and Ploegh, H.L. (2019). Internalization of Influenza Virus and Cell Surface Proteins Monitored by Site-Specific Conjugation of Protease-Sensitive Probes. ACS Chem. Biol. *14*, 1836–1844.

29. Chen, X., Bi, Y., Wang, T., Li, P., Yan, X., Hou, S., Bammert, C.E., Ju, J., Gibson, K.M., Pavan, W.J., et al. (2015). Lysosomal Targeting with Stable and Sensitive Fluorescent Probes (Superior LysoProbes): Applications for Lysosome Labeling and Tracking during Apoptosis. Sci Rep *5*, 9004.

30. Chia, J., Goh, G., Racine, V., Ng, S., Kumar, P., and Bard, F. (2012). RNAi screening reveals a large signaling network controlling the Golgi apparatus in human cells. Molecular Systems Biology *8*, 629.

31. Chin, M.Y., Patwardhan, A.R., Ang, K.K., Wang, A.L., Alquezar, C., Welch, M., Arkin, M.R., and Kao, A.W. (November 2020). Genetically encoded ratiometric biosensor for

probing lysosomal pH in mammalian cells and *C. elegans*. (BioRxiv pre-print). doi: https://doi.org/10.1101/2020.11.04.368654.

32. Chong, S., Dugast-Darzacq, C., Liu, Z., Dong, P., Dailey, G.M., Cattoglio, C., Heckert, A., Banala, S., Lavis, L., Darzacq, X., et al. (2018). Imaging dynamic and selective low-complexity domain interactions that control gene transcription. Science *361*.

33. Circu, M.L., Dykes, S.S., Carroll, J., Kelly, K., Galiano, F., Greer, A., Cardelli, J., and El-Osta, H. (2016). A Novel High Content Imaging-Based Screen Identifies the Anti-Helminthic Niclosamide as an Inhibitor of Lysosome Anterograde Trafficking and Prostate Cancer Cell Invasion. PLoS ONE *11*, e0146931.

34. Clarke, J.T.R., Mahuran, D.J., Sathe, S., Kolodny, E.H., Rigat, B.A., Raiman, J.A., and Tropak, M.B. (2011). An open-label Phase I/II clinical trial of pyrimethamine for the treatment of patients affected with chronic GM2 gangliosidosis (Tay–Sachs or Sandhoff variants). Mol Genet Metab *102*, 6–12.

35. Colacurcio, D.J., and Nixon, R.A. (2016). Disorders of lysosomal acidification—The emerging role of v-ATPase in aging and neurodegenerative disease. Ageing Research Reviews *32*, 75–88.

36. Colussi, D.J., and Jacobson, M.A. (2019). Patient-Derived Phenotypic High-Throughput Assay to Identify Small Molecules Restoring Lysosomal Function in Tay–Sachs Disease. SLAS DISCOVERY: Advancing the Science of Drug Discovery *24*, 295–303.

37. Conicella, A.E., Zerze, G.H., Mittal, J., and Fawzi, N.L. (2016). ALS mutations disrupt phase separation mediated by -helical structure in the TDP-43 low complexity C-terminal domain. Structure *24*, 1537–1549.

38. Crabtree, M., and Nott, T. (2018). These Organelles Have No Membranes.

39. Creed, S., and McKenzie, M. (2019). Measurement of Mitochondrial Membrane Potential with the Fluorescent Dye Tetramethylrhodamine Methyl Ester (TMRM). In Cancer Metabolism: Methods and Protocols, M. Haznadar, ed. (New York, NY: Springer), pp. 69–76.

40. Crouch, S.P.M., Kozlowski, R., Slater, K.J., and Fletcher, J. (1993). The use of ATP bioluminescence as a measure of cell proliferation and cytotoxicity. Journal of Immunological Methods *160*, 81–88.

41. Daemen, S., van Zandvoort, M.A.M.J., Parekh, S.H., and Hesselink, M.K.C. (2015). Microscopy tools for the investigation of intracellular lipid storage and dynamics. Mol Metab *5*, 153–163.

42. D'Autréaux, B., and Toledano, M.B. (2007). ROS as signalling molecules: mechanisms that generate specificity in ROS homeostasis. Nature Reviews Molecular Cell Biology *8*, 813–824.

43. De Biasi, S., Gibellini, L., Bianchini, E., Nasi, M., Pinti, M., Salvioli, S., and Cossarizza, A. (2016). Quantification of mitochondrial reactive oxygen species in living cells by using multi-laser polychromatic flow cytometry: Quantification of Mitochondrial Reactive Oxygen Species. Cytometry 89, 1106–1110.

44. Deschamps, A., Colinet, A.-S., Zimmermannova, O., Sychrova, H., and Morsomme, P. (2020). A new pH sensor localized in the Golgi apparatus of Saccharomyces cerevisiae reveals unexpected roles of Vph1p and Stv1p isoforms. Sci Rep *10*, 1881.

45. Deshwal, S., Antonucci, S., Kaludercic, N., and Di Lisa, F. (2018). Measurement of Mitochondrial ROS Formation. In Mitochondrial Bioenergetics, C.M. Palmeira, and A.J. Moreno, eds. (New York, NY: Springer New York), pp. 403–418.

46. Dilcher, M., Veith, B., Chidambaram, S., Hartmann, E., Schmitt, H.D., and Fischer von Mollard, G. (2003). Use1p is a yeast SNARE protein required for retrograde traffic to the ER. EMBO J *22*, 3664–3674.

47. Dundr, M., Misteli, T., and Olson, M.O.J. (2000). The Dynamics of Postmitotic Reassembly of the Nucleolus. J Cell Biol *150*, 433–446.

48. Elbaum-Garfinkle, S. (2019). Matter over mind: Liquid phase separation and neurodegeneration. J Biol Chem *294*, 7160–7168.

49. Elmore, S.P., Nishimura, Y., Qian, T., Herman, B., and Lemasters, J.J. (2004). Discrimination of depolarized from polarized mitochondria by confocal fluorescence resonance energy transfer. Archives of Biochemistry and Biophysics *422*, 145–152.

50. Ermakova, Y.G., Bilan, D.S., Matlashov, M.E., Mishina, N.M., Markvicheva, K.N., Subach, O.M., Subach, F.V., Bogeski, I., Hoth, M., Enikolopov, G., et al. (2014). Red fluorescent genetically encoded indicator for intracellular hydrogen peroxide. Nature Communications *5*, 5222.

51. Fam, T.K., Klymchenko, A.S., and Collot, M. (2018). Recent Advances in Fluorescent Probes for Lipid Droplets. Materials (Basel) *11*.

52. Fan, A.C., and Leung, A.K.L. (2016). RNA Granules and Diseases — A Case Study of Stress Granules in ALS and FTLD. Adv Exp Med Biol *907*, 263–296.

53. Fan, L., Wang, X., Ge, J., Li, F., Zhang, C., Lin, B., Shuang, S., and Dong, C. (2019). A Golgi-targeted off–on fluorescent probe for real-time monitoring of pH changes *in vivo*. Chem. Commun. *55*, 6685–6688.

54. Fei, J., Jadaliha, M., Harmon, T.S., Li, I.T.S., Hua, B., Hao, Q., Holehouse, A.S., Reyer, M., Sun, Q., Freier, S.M., et al. (2017). Quantitative analysis of multilayer organization of proteins and RNA in nuclear speckles at super resolution. J Cell Sci *130*, 4180–4192.

55. Feng, X., and Yang, J. (2016). Lysosomal Calcium in Neurodegeneration. Messenger (Los Angel) *5*, 56–66.

56. Filonov, G.S., Moon, J.D., Svensen, N., and Jaffrey, S.R. (2014). Broccoli: Rapid Selection of an RNA Mimic of Green Fluorescent Protein by Fluorescence-Based Selection and Directed Evolution. J. Am. Chem. Soc. *136*, 16299–16308.

57. Fleming, A., Noda, T., Yoshimori, T., and Rubinsztein, D.C. (2011). Chemical modulators of autophagy as biological probes and potential therapeutics. Nat Chem Biol *7*, 9–17.

58. de la Fuente-Herreruela, D., Gónzalez-Charro, V., Almendro-Vedia, V.G., Morán, M., Martín, M.Á., Lillo, M.P., Natale, P., and López-Montero, I. (2017). Rhodamine-based sensor for real-time imaging of mitochondrial ATP in living fibroblasts. Biochimica et Biophysica Acta (BBA) - Bioenergetics *1858*, 999–1006.

59. Galea, G., and Simpson, J.C. (2013). High-Content Screening and Analysis of the Golgi Complex. In Methods in Cell Biology, (Elsevier), pp. 281–295.

60. Galea, G., Bexiga, M.G., Panarella, A., O'Neill, E.D., and Simpson, J.C. (2015). A high-content screening microscopy approach to dissect the role of Rab proteins in Golgi-to-ER retrograde trafficking. Journal of Cell Science *128*, 2339–2349.

61. Galganski, L., Urbanek, M.O., and Krzyzosiak, W.J. (2017). Nuclear speckles: molecular organization, biological function and role in disease. Nucleic Acids Res *45*, 10350–10368.

62. Ganassi, M., Mateju, D., Bigi, I., Mediani, L., Poser, I., Lee, H.O., Seguin, S.J., Morelli, F.F., Vinet, J., Leo, G., et al. (2016). A Surveillance Function of the HSPB8-BAG3-HSP70 Chaperone Complex Ensures Stress Granule Integrity and Dynamism. Molecular Cell *63*, 796–810.

63. Giammarioli, A.M., Gambardella, L., Barbati, C., Pietraforte, D., Tinari, A., Alberton, M., Gnessi, L., Griffin, R.J., Minetti, M., and Malorni, W. (2012). Differential effects of the glycolysis inhibitor 2-deoxy-D-glucose on the activity of pro-apoptotic agents in metastatic melanoma cells, and induction of a cytoprotective autophagic response. Int. J. Cancer *131*, E337-347.

64. Guan, D., and Kao, H.-Y. (2015). The function, regulation and therapeutic implications of the tumor suppressor protein, PML. Cell & Bioscience *5*, 60.

65. Gurrieri, C., Capodieci, P., Bernardi, R., Scaglioni, P.P., Nafa, K., Rush, L.J., Verbel, D.A., Cordon-Cardo, C., and Pandolfi, P.P. (2004). Loss of the Tumor Suppressor PML in Human Cancers of Multiple Histologic Origins. J Natl Cancer Inst *96*, 269–279.

66. Gustafsson, M.G.L., Shao, L., Carlton, P.M., Wang, C.J.R., Golubovskaya, I.N., Cande, W.Z., Agard, D.A., and Sedat, J.W. (2008). Three-Dimensional Resolution Doubling in Wide-Field Fluorescence Microscopy by Structured Illumination. Biophysical Journal *94*, 4957–4970.

67. Gutscher, M., Pauleau, A.-L., Marty, L., Brach, T., Wabnitz, G.H., Samstag, Y., Meyer, A.J., and Dick, T.P. (2008). Real-time imaging of the intracellular glutathione redox potential. Nat Methods *5*, 553–559.

68. van Hameren, G., Campbell, G., Deck, M., Berthelot, J., Gautier, B., Quintana, P., Chrast, R., and Tricaud, N. (2019). In vivo real-time dynamics of ATP and ROS

production in axonal mitochondria show decoupling in mouse models of peripheral neuropathies. Acta Neuropathologica Communications *7*, 86.

69. Hanson, G.T., Aggeler, R., Oglesbee, D., Cannon, M., Capaldi, R.A., Tsien, R.Y., and Remington, S.J. (2004). Investigating Mitochondrial Redox Potential with Redox-sensitive Green Fluorescent Protein Indicators. J. Biol. Chem. *279*, 13044–13053.

70. Harguindey, S., Reshkin, S., Orive, G., Luis Arranz, J., and Anitua, E. (2007). Growth and Trophic Factors, pH and the Na+/H+ Exchanger in Alzheimers Disease, Other Neurodegenerative Diseases and Cancer: New Therapeutic Possibilities and Potential Dangers. CAR *4*, 53–65.

71. Harwig, M.C., Viana, M.P., Egner, J.M., Harwig, J.J., Widlansky, M.E., Rafelski, S.M., and Hill, R.B. (2018). Methods for imaging mammalian mitochondrial morphology: A prospective on MitoGraph. Analytical Biochemistry *552*, 81–99.

72. He, J.-S., Soo, P., Evers, M., Parsons, K.M., Hein, N., Hannan, K.M., Hannan, R.D., and George, A.J. (2018). High-Content Imaging Approaches to Quantitate Stress-Induced Changes in Nucleolar Morphology. ASSAY and Drug Development Technologies *16*, 320–332.

73. Hicks, S.W., and Machamer, C.E. (2005). Golgi structure in stress sensing and apoptosis. Biochimica et Biophysica Acta (BBA) - Molecular Cell Research *1744*, 406–414.

74. Hirayama, T., Inden, M., Tsuboi, H., Niwa, M., Uchida, Y., Naka, Y., Hozumi, I., and Nagasawa, H. (2019). A Golgi-targeting fluorescent probe for labile Fe(ii) to reveal an abnormal cellular iron distribution induced by dysfunction of VPS35. Chem. Sci. *10*, 1514–1521.

75. Hu, J., Dong, L., and Outten, C.E. (2008). The Redox Environment in the Mitochondrial Intermembrane Space Is Maintained Separately from the Cytosol and Matrix. J. Biol. Chem. *283*, 29126–29134.

76. Hussain, S., Le Guezennec, X., Yi, W., Dong, H., Chia, J., Yiping, K., Khoon, L.K., and Bard, F. (2017). Digging deep into Golgi phenotypic diversity with unsupervised machine learning. MBoC *28*, 3686–3698.

77. Iannetti, E.F., Smeitink, J.A.M., Beyrath, J., Willems, P.H.G.M., and Koopman, W.J.H. (2016). Multiplexed high-content analysis of mitochondrial morphofunction using live-cell microscopy. Nat Protoc *11*, 1693–1710.

78. Iannetti, E.F., Prigione, A., Smeitink, J.A.M., Koopman, W.J.H., Beyrath, J., and Renkema, H. (2019). Live-Imaging Readouts and Cell Models for Phenotypic Profiling of Mitochondrial Function. Front. Genet. *10*, 131.

79. Ilangumaran, S., and Hoessli, D.C. (1998). Effects of cholesterol depletion by cyclodextrin on the sphingolipid microdomains of the plasma membrane. Biochem J *335*, 433–440.

80. Imamura, H., Huynh Nhat, K.P., Togawa, H., Saito, K., Iino, R., Kato-Yamada, Y., Nagai, T., and Noji, H. (2009). Visualization of ATP levels inside single living cells with fluorescence resonance energy transfer-based genetically encoded indicators. PNAS *106*, 15651–15656.

81. Ishida, M., Watanabe, H., Takigawa, K., Kurishita, Y., Oki, C., Nakamura, A., Hamachi, I., and Tsukiji, S. (2013). Synthetic self-localizing ligands that control the spatial location of proteins in living cells. J. Am. Chem. Soc. *135*, 12684–12689.

82. Ishii, S., Matsuura, A., and Itakura, E. (2019). Identification of a factor controlling lysosomal homeostasis using a novel lysosomal trafficking probe. Scientific Reports *9*, 11635.

83. Jain, S., Wheeler, J.R., Walters, R.W., Agrawal, A., Barsic, A., and Parker, R. (2016). ATPase-Modulated Stress Granules Contain a Diverse Proteome and Substructure. Cell *164*, 487–498.

84. Jang, J.-W., Song, Y., Kim, K.M., Kim, J.-S., Choi, E.K., Kim, J., and Seo, H. (2016). Hepatocellular carcinoma-targeted drug discovery through image-based phenotypic screening in co-cultures of HCC cells with hepatocytes. BMC Cancer *16*, 810.

85. Jevtic, V., Kindle, P., and Avilov, S.V. (2018). SYBR Gold dye enables preferential labelling of mitochondrial nucleoids and their time-lapse imaging by structured illumination microscopy. PLoS ONE *13*, e0203956.

86. Ji, L.L., Yeo, D., Kang, C., and Zhang, T. (2020). The role of mitochondria in redox signaling of muscle homeostasis. Journal of Sport and Health Science S2095254620300089.

87. Joshi, G., Chi, Y., Huang, Z., and Wang, Y. (2014). Aβ-induced Golgi fragmentation in Alzheimer's disease enhances Aβ production. PNAS *111*, E1230–E1239.

88. Joshi, G., Bekier, M.I., and Wang, Y. (2015). Golgi Fragmentation in Alzheimer's Disease. Front. Neurosci. *9*.

89. Kallunki, T., Olsen, O.D., and Jäättelä, M. (2013). Cancer-associated lysosomal changes: friends or foes? Oncogene *32*, 1995–2004.

90. Kaludercic, N., Deshwal, S., and Di Lisa, F. (2014). Reactive oxygen species and redox compartmentalization. Front. Physiol. *5*.

91. Kasper, D., Planells-Cases, R., Fuhrmann, J.C., Scheel, O., Zeitz, O., Ruether, K., Schmitt, A., Poët, M., Steinfeld, R., Schweizer, M., et al. (2005). Loss of the chloride channel ClC-7 leads to lysosomal storage disease and neurodegeneration. EMBO J *24*, 1079–1091.

92. Kellokumpu, S., Sormunen, R., and Kellokumpu, I. (2002). Abnormal glycosylation and altered Golgi structure in colorectal cancer: dependence on intra-Golgi pH. FEBS Letters *516*, 217–224.

93. Kempfer, R., and Pombo, A. (2020). Methods for mapping 3D chromosome architecture. Nature Reviews Genetics *21*, 207–226.

94. Khacho, M., and Slack, R.S. (2018). Mitochondrial dynamics in the regulation of neurogenesis: From development to the adult brain. Developmental Dynamics *247*, 47–53.

95. Kimball, S.R., Horetsky, R.L., Ron, D., Jefferson, L.S., and Harding, H.P. (2003). Mammalian stress granules represent sites of accumulation of stalled translation initiation complexes. American Journal of Physiology-Cell Physiology *284*, C273–C284.

96. Kirkegaard, T., and Jäättelä, M. (2009). Lysosomal involvement in cell death and cancer. Biochimica et Biophysica Acta (BBA) - Molecular Cell Research *1793*, 746–754.

97. Koch, J., Feichtinger, R.G., Freisinger, P., Pies, M., Schrödl, F., Iuso, A., Sperl, W., Mayr, J.A., Prokisch, H., and Haack, T.B. (2016). Disturbed mitochondrial and peroxisomal dynamics due to loss of MFF causes Leigh-like encephalopathy, optic atrophy and peripheral neuropathy. J Med Genet *53*, 270–278.

98. Lafarga, M., Tapia, O., Romero, A.M., and Berciano, M.T. (2016). Cajal bodies in neurons. RNA Biol *14*, 712–725.

99. Lajoie, P., Fazio, E.N., and Snapp, E.L. (2014). Approaches to imaging unfolded secretory protein stress in living cells. Endoplasmic Reticulum Stress Dis *1*, 27–39.

100. Lallemand-Breitenbach, V., and de Thé, H. (2010). PML Nuclear Bodies. Cold Spring Harb Perspect Biol *2*.

101. Lashuel, H.A., and Hirling, H. (2006). Rescuing Defective Vesicular Trafficking Protects against α-Synuclein Toxicity in Cellular and Animal Models of Parkinson's Disease. ACS Chem. Biol. *1*, 420–424.

102. Lee, M.-C., Chen, Y.-K., Hsu, Y.-J., and Lin, B.-R. (2020). Niclosamide inhibits the cell proliferation and enhances the responsiveness of esophageal cancer cells to chemotherapeutic agents. Oncology Reports *43*, 549–561.

103. Leung, A.K.L., Gerlich, D., Miller, G., Lyon, C., Lam, Y.W., Lleres, D., Daigle, N., Zomerdijk, J., Ellenberg, J., and Lamond, A.I. (2004). Quantitative kinetic analysis of nucleolar breakdown and reassembly during mitosis in live human cells. J Cell Biol *166*, 787–800.

104. Leung, K., Chakraborty, K., Saminathan, A., and Krishnan, Y. (2019). A DNA nanomachine chemically resolves lysosomes in live cells. Nature Nanotech *14*, 176–183.

105. Li, P., Guo, X., Bai, X., Wang, X., Ding, Q., Zhang, W., Zhang, W., and Tang, B. (2019). Golgi Apparatus Polarity Indicates Depression-Like Behaviors of Mice Using in Vivo Fluorescence Imaging. Anal. Chem. *91*, 3382–3388.

106. Li, Q., Kim, Y., Namm, J., Kulkarni, A., Rosania, G.R., Ahn, Y.-H., and Chang, Y.-T. (2006). RNA-Selective, Live Cell Imaging Probes for Studying Nuclear Structure and Function. Chemistry & Biology *13*, 615–623.

107. Li, R.S., Gao, P.F., Zhang, H.Z., Zheng, L.L., Li, C.M., Wang, J., Li, Y.F., Liu, F., Li, N., and Huang, C.Z. (2017). Chiral nanoprobes for targeting and long-term imaging of the Golgi apparatus. Chem. Sci. *8*, 6829–6835.

108. Li, Z., Sun, S., Yang, Z., Zhang, S., Zhang, H., Hu, M., Cao, J., Wang, J., Liu, F., Song, F., et al. (2013). The use of a near-infrared RNA fluorescent probe with a large Stokes shift for imaging living cells assisted by the macrocyclic molecule CB7. Biomaterials *34*, 6473–6481.

109. Liao, P.-C., Franco-Iborra, S., Yang, Y., and Pon, L.A. (2020). Chapter 12 - Live cell imaging of mitochondrial redox state in mammalian cells and yeast. In Methods in Cell Biology, L.A. Pon, and E.A. Schon, eds. (Academic Press), pp. 295–319.

110. Little, D., Luft, C., Mosaku, O., Lorvellec, M., Yao, Z., Paillusson, S., Kriston-Vizi, J., Gandhi, S., Abramov, A.Y., Ketteler, R., et al. (2018). A single cell high content assay detects mitochondrial dysfunction in iPSC-derived neurons with mutations in SNCA. Sci Rep *8*, 9033.

111. Liu, W., Zhou, B., Niu, G., Ge, J., Wu, J., Zhang, H., Xu, H., and Wang, P. (2015). Deep-Red Emissive Crescent-Shaped Fluorescent Dyes: Substituent Effect on Live Cell Imaging. ACS Appl. Mater. Interfaces *7*, 7421–7427.

112. Liu, Y., Jin, M., Wang, Y., Zhu, J., Tan, R., Zhao, J., Ji, X., Jin, C., Jia, Y., Ren, T., et al. (2020). MCU-induced mitochondrial calcium uptake promotes mitochondrial biogenesis and colorectal cancer growth. Sig Transduct Target Ther *5*, 59.

113. Lu, Y.-J., Deng, Q., Hu, D.-P., Wang, Z.-Y., Huang, B.-H., Du, Z.-Y., Fang, Y.-X., Wong, W.-L., Zhang, K., and Chow, C.-F. (2015). A molecular fluorescent dye for

specific staining and imaging of RNA in live cells: a novel ligand integration from classical thiazole orange and styryl compounds. Chem. Commun. *51*, 15241–15244.

114. Lu, Y.-J., Deng, Q., Hou, J.-Q., Hu, D.-P., Wang, Z.-Y., Zhang, K., Luyt, L.G., Wong, W.-L., and Chow, C.-F. (2016). Molecular Engineering of Thiazole Orange Dye: Change of Fluorescent Signaling from Universal to Specific upon Binding with Nucleic Acids in Bioassay. ACS Chem. Biol. *11*, 1019–1029.

115. Luo, Y., Na, Z., and Slavoff, S.A. (2018). P-Bodies: Composition, Properties, and Functions. Biochemistry *57*, 2424–2431.

116. Maeda, Y., Beznoussenko, G.V., Van Lint, J., Mironov, A.A., and Malhotra, V. (2001). Recruitment of protein kinase D to the trans-Golgi network via the first cysteine-rich domain. EMBO J *20*, 5982–5990.

117. Magrané, J., Cortez, C., Gan, W.-B., and Manfredi, G. (2014). Abnormal mitochondrial transport and morphology are common pathological denominators in SOD1 and TDP43 ALS mouse models. Hum Mol Genet *23*, 1413–1424.

118. Major, A.T., Miyamoto, Y., Lo, C.Y., Jans, D.A., and Loveland, K.L. (2017). Development of a pipeline for automated, high-throughput analysis of paraspeckle proteins reveals specific roles for importin α proteins. Sci Rep *7*.

119. Markvicheva, K.N., Bilan, D.S., Mishina, N.M., Gorokhovatsky, A.Yu., Vinokurov, L.M., Lukyanov, S., and Belousov, V.V. (2011). A genetically encoded sensor for H2O2 with expanded dynamic range. Bioorganic & Medicinal Chemistry *19*, 1079–1084.

120. Marrone, L., Poser, I., Casci, I., Japtok, J., Reinhardt, P., Janosch, A., Andree, C., Lee, H.O., Moebius, C., Koerner, E., et al. (2018). Isogenic FUS-eGFP iPSC Reporter Lines

Enable Quantification of FUS Stress Granule Pathology that Is Rescued by Drugs Inducing Autophagy. Stem Cell Reports *10*, 375–389.

121. Mattson, M.P., Gleichmann, M., and Cheng, A. (2008). Mitochondria in Neuroplasticity and Neurological Disorders. Neuron *60*, 748–766.

122. McInnes, J. (2013). Mitochondrial-associated metabolic disorders: foundations, pathologies and recent progress. Nutr Metab (Lond) *10*, 63.

123. Medina, D.L., and Ballabio, A. (2015). Lysosomal calcium regulates autophagy. Autophagy *11*, 970–971.

124. Mindell, J.A. (2012). Lysosomal acidification mechanisms. Annu. Rev. Physiol. *74*, 69–86.

125. Mitrea, D.M., Chandra, B., Ferrolino, M.C., Gibbs, E.B., Tolbert, M., White, M.R., and Kriwacki, R.W. (2018). Methods for Physical Characterization of Phase-Separated Bodies and Membrane-less Organelles. Journal of Molecular Biology *430*, 4773–4805.

126. Moon, S.L., Morisaki, T., Khong, A., Lyon, K., Parker, R., and Stasevich, T.J. (2019). Multicolour single-molecule tracking of mRNA interactions with RNP granules. Nat Cell Biol *21*, 162–168.

127. Morris, G.E. (2008). The Cajal body. Biochimica et Biophysica Acta (BBA) - Molecular Cell Research *1783*, 2108–2115.

128. Murakami, T., Qamar, S., Lin, J.Q., Schierle, G.S.K., Rees, E., Miyashita, A., Costa, A.R., Dodd, R.B., Chan, F.T.S., Michel, C.H., et al. (2015). ALS/FTD Mutation-Induced Phase Transition of FUS Liquid Droplets and Reversible Hydrogels into Irreversible Hydrogels Impairs RNP Granule Function. Neuron *88*, 678–690.

129. Murphy, E., Ardehali, H., Balaban, R.S., DiLisa, F., Dorn, G.W., Kitsis, R.N., Otsu, K., Ping, P., Rizzuto, R., Sack, M.N., et al. (2016). Mitochondrial Function, Biology, and Role in Disease: A Scientific Statement From the American Heart Association. Circ Res *118*, 1960–1991.

130. Naslavsky, N., and Caplan, S. (2018). The enigmatic endosome – sorting the ins and outs of endocytic trafficking. J Cell Sci *131*, jcs216499.

131. Paige, J.S., Wu, K.Y., and Jaffrey, S.R. (2011). RNA Mimics of Green Fluorescent Protein. Science *333*, 642–646.

132. Panda, P.K., Fahrner, A., Vats, S., Seranova, E., Sharma, V., Chipara, M., Desai, P., Torresi, J., Rosenstock, T., Kumar, D., et al. (2019). Chemical Screening Approaches Enabling Drug Discovery of Autophagy Modulators for Biomedical Applications in Human Diseases. Front. Cell Dev. Biol. *7*, 38.

133. Paroutis, P., Touret, N., and Grinstein, S. (2004). The pH of the Secretory Pathway: Measurement, Determinants, and Regulation. Physiology *19*, 207–215.

134. Pederson, T. (2011). The Nucleolus. Cold Spring Harb Perspect Biol *3*, a000638.

135. Peng, Y., Gao, P., Shi, L., Chen, L., Liu, J., and Long, J. (2020). Central and Peripheral Metabolic Defects Contribute to the Pathogenesis of Alzheimer's Disease: Targeting Mitochondria for Diagnosis and Prevention. Antioxidants & Redox Signaling *32*, 1188–1236.

136. Perrin, D.D. (1965). Dissociation constants of organic bases in aqueous solution (London: Butterworths).

137. Petrosyan, A. (2015). Onco-Golgi: Is Fragmentation a Gate to Cancer Progression? Biochem Mol Biol J *1*.

138. Piattoni, C.V., Sardi, F., Klein, F., Pantano, S., Bollati-Fogolin, M., and Comini, M. (2019). New red-shifted fluorescent biosensor for monitoring intracellular redox changes. Free Radical Biology and Medicine *134*, 545–554.

139. Platani, M., Goldberg, I., Swedlow, J.R., and Lamond, A.I. (2000). In Vivo Analysis of Cajal Body Movement, Separation, and Joining in Live Human Cells. J Cell Biol *151*, 1561–1574.

140. Pohan, G., Espinosa, J.A., Chen, S., Ang, K.K., Arkin, M.R., and Markossian, S. (2020). Multiparametric High-Content Assays to Measure Cell Health and Oxidative Damage as a Model for Drug-Induced Liver Injury. Current Protocols in Chemical Biology 12, e90.

141. Policarpio-Nicolas, M.L.C., and Sirohi, D. (2013). Macrofollicular variant of papillary carcinoma, a potential diagnostic pitfall: A report of two cases including a review of literature. Cytojournal *10*.

142. Ponsford, A.H., Ryan, T.A., Raimondi, A., Cocucci, E., Wycislo, S.A., Fröhlich, F., Swan, L.E., and Stagi, M. (2020). Live imaging of intra-lysosome pH in cell lines and primary neuronal culture using a novel genetically encoded biosensor. Autophagy 1–19.

143. Pugach, E.K., Feltes, M., Kaufman, R.J., Ory, D.S., and Bang, A.G. (2018). High-content screen for modifiers of Niemann-Pick type C disease in patient cells. Hum Mol Genet *27*, 2101–2112.

144. Reineke, E.L., and Kao, H.-Y. (2009). PML: An emerging tumor suppressor and a target with therapeutic potential. Cancer Ther *7*, 219–226.

145. Rivinoja, A., Pujol, F.M., Hassinen, A., and Kellokumpu, S. (2012). Golgi pH, its regulation and roles in human disease. Annals of Medicine *44*, 542–554.

146. Rosania, G.R., Lee, J.W., Ding, L., Yoon, H.-S., and Chang, Y.-T. (2003). Combinatorial Approach to Organelle-Targeted Fluorescent Library Based on the Styryl Scaffold. J. Am. Chem. Soc. *125*, 1130–1131.

147. Rosenbaum, A.I., Zhang, G., Warren, J.D., and Maxfield, F.R. (2010). Endocytosis of beta-cyclodextrins is responsible for cholesterol reduction in Niemann-Pick type C mutant cells. Proc Natl Acad Sci U S A *107*, 5477–5482.

148. Ryu, H.-H., Jun, M.-H., Min, K.-J., Jang, D.-J., Lee, Y.-S., Kim, H.K., and Lee, J.-A. (2014). Autophagy regulates amyotrophic lateral sclerosis-linked fused in sarcoma-positive stress granules in neurons. Neurobiology of Aging *35*, 2822–2831.

149. Saha, S., Prakash, V., Halder, S., Chakraborty, K., and Krishnan, Y. (2015). A pH-independent DNA nanodevice for quantifying chloride transport in organelles of living cells. Nature Nanotechnology *10*, 645–651.

150. Scott, I., and Youle, R.J. (2010). Mitochondrial fission and fusion. Essays Biochem *47*, 85–98.

151. Scotto Rosato, A., Montefusco, S., Soldati, C., Di Paola, S., Capuozzo, A., Monfregola, J., Polishchuk, E., Amabile, A., Grimm, C., Lombardo, A., et al. (2019). TRPML1 links lysosomal calcium to autophagosome biogenesis through the activation of the CaMKKβ/VPS34 pathway. Nat Commun *10*.

152. Settembre, C., Fraldi, A., Medina, D.L., and Ballabio, A. (2013). Signals for the lysosome: a control center for cellular clearance and energy metabolism. Nat Rev Mol Cell Biol *14*, 283–296.

153. Shlevkov, E., Basu, H., Bray, M.-A., Sun, Z., Wei, W., Apaydin, K., Karhohs, K., Chen, P.-F., Smith, J.L.M., Wiskow, O., et al. (2019). A High-Content Screen Identifies TPP1

and Aurora B as Regulators of Axonal Mitochondrial Transport. Cell Reports *28*, 3224-3237.e5.

154. Shorter, J., Beard, M.B., Seemann, J., Dirac-Svejstrup, A.B., and Warren, G. (2002). Sequential tethering of Golgins and catalysis of SNAREpin assembly by the vesicle-tethering protein p115. J Cell Biol *157*, 45–62.

155. Shu, C.-W., Liu, P.-F., and Huang, C.-M. (2012). High Throughput Screening for Drug Discovery of Autophagy Modulators. CCHTS *15*, 721–729.

156. Song, G., Sun, Y., Liu, Y., Wang, X., Chen, M., Miao, F., Zhang, W., Yu, X., and Jin, J. (2014). Low molecular weight fluorescent probes with good photostability for imaging RNA-rich nucleolus and RNA in cytoplasm in living cells. Biomaterials *35*, 2103–2112.

157. Soo, K.Y., Halloran, M., Sundaramoorthy, V., Parakh, S., Toth, R.P., Southam, K.A., McLean, C.A., Lock, P., King, A., Farg, M.A., et al. (2015). Rab1-dependent ER–Golgi transport dysfunction is a common pathogenic mechanism in SOD1, TDP-43 and FUS-associated ALS. Acta Neuropathol *130*, 679–697.

158. Spang, A. (2013). Retrograde Traffic from the Golgi to the Endoplasmic Reticulum. Cold Spring Harb Perspect Biol *5*, a013391.

159. Spector, D.L., and Lamond, A.I. (2011). Nuclear Speckles. Cold Spring Harb Perspect Biol *3*.

160. Steffan, J.J., Snider, J.L., Skalli, O., Welbourne, T., and Cardelli, J.A. (2009). Na+/H+ Exchangers and RhoA Regulate Acidic Extracellular pH-Induced Lysosome Trafficking in Prostate Cancer Cells. Traffic *10*, 737–753.

161. Steffan, J.J., Coleman, D.T., and Cardelli, J.A. (2011). The HGF-met signaling axis: emerging themes and targets of inhibition. Curr. Protein Pept. Sci. *12*, 12–22.

162. Stoka, V., Turk, V., and Turk, B. (2016). Lysosomal cathepsins and their regulation in aging and neurodegeneration. Ageing Research Reviews *32*, 22–37.

163. Thompson, A.D., Bewersdorf, J., Toomre, D., and Schepartz, A. (2017). HIDE Probes: A New Toolkit for Visualizing Organelle Dynamics, Longer and at Super-Resolution. Biochemistry *56*, 5194–5201.

164. To, T.-L., Piggott, B.J., Makhijani, K., Yu, D., Jan, Y.N., and Shu, X. (2015). Rationally designed fluorogenic protease reporter visualizes spatiotemporal dynamics of apoptosis in vivo. Proc Natl Acad Sci USA *112*, 3338–3343.

165. Tomas, A., Futter, C.E., and Eden, E.R. (2014). EGF receptor trafficking: consequences for signaling and cancer. Trends Cell Biol *24*, 26–34.

166. Tommasino, C., Gambardella, L., Buoncervello, M., Griffin, R.J., Golding, B.T., Alberton, M., Macchia, D., Spada, M., Cerbelli, B., d'Amati, G., et al. (2016). New derivatives of the antimalarial drug Pyrimethamine in the control of melanoma tumor growth: an in vitro and in vivo study. J Exp Clin Cancer Res *35*.

167. Tomsic, J., He, H., Akagi, K., Liyanarachchi, S., Pan, Q., Bertani, B., Nagy, R., Symer, D.E., Blencowe, B.J., and Chapelle, A. de la (2015). A germline mutation in SRRM2 , a splicing factor gene, is implicated in papillary thyroid carcinoma predisposition. Scientific Reports *5*, 10566.

168. Tripathi, V., Song, D.Y., Zong, X., Shevtsov, S.P., Hearn, S., Fu, X.-D., Dundr, M., and Prasanth, K.V. (2012). SRSF1 regulates the assembly of pre-mRNA processing factors in nuclear speckles. Mol Biol Cell *23*, 3694–3706.

169. Tuma, R.S., Beaudet, M.P., Jin, X., Jones, L.J., Cheung, C.-Y., Yue, S., and Singer, V.L. (1999). Characterization of SYBR Gold Nucleic Acid Gel Stain: A Dye Optimized for Use with 300-nm Ultraviolet Transilluminators. Analytical Biochemistry *268*, 278–288.

170. Valm, A.M., Cohen, S., Legant, W.R., Melunis, J., Hershberg, U., Wait, E., Cohen, A.R., Davidson, M.W., Betzig, E., and Lippincott-Schwartz, J. (2017). Applying systems-level spectral imaging and analysis to reveal the organelle interactome. Nature *546*, 162–167.

171. Varkuti, B.H., Liu, Z., Kepiro, M., Pacifico, R., Gai, Y., Kamenecka, T., and Davis, R.L. (2020). High-Throughput Small Molecule Screen Identifies Modulators of Mitochondrial Function in Neurons. IScience *23*, 100931.

172. Vila, M.C., Rayavarapu, S., Hogarth, M.W., Van der Meulen, J.H., Horn, A., Defour, A., Takeda, S., Brown, K.J., Hathout, Y., Nagaraju, K., et al. (2017). Mitochondria mediate cell membrane repair and contribute to Duchenne muscular dystrophy. Cell Death & Differentiation *24*, 330–342.

173. Vringer, E., and Tait, S.W.G. (2019). Mitochondria and Inflammation: Cell Death Heats Up. Front. Cell Dev. Biol. *7*, 100.

174. Wang, C., Lu, T., Emanuel, G., Babcock, H.P., and Zhuang, X. (2019). Imaging-based pooled CRISPR screening reveals regulators of lncRNA localization. PNAS *116*, 10842–10851.

175. Wang, L.-H., Xu, M., Fu, L.-Q., Chen, X.-Y., and Yang, F. (2018). The Antihelminthic Niclosamide Inhibits Cancer Stemness, Extracellular Matrix Remodeling, and Metastasis through Dysregulation of the Nuclear β-catenin/c-Myc axis in OSCC. Scientific Reports *8*, 12776.

176. Wang, W., Li, L., Lin, W.-L., Dickson, D.W., Petrucelli, L., Zhang, T., and Wang, X. (2013). The ALS disease-associated mutant TDP-43 impairs mitochondrial dynamics and function in motor neurons. Hum Mol Genet *22*, 4706–4719.

177. Waris, S., Wilce, M.C.J., and Wilce, J.A. (2014). RNA Recognition and Stress Granule Formation by TIA Proteins. Int J Mol Sci *15*, 23377–23388.

178. Waterham, H.R., Koster, J., van Roermund, C.W.T., Mooyer, P.A.W., Wanders, R.J.A., and Leonard, J.V. (2007). A Lethal Defect of Mitochondrial and Peroxisomal Fission. N Engl J Med *356*, 1736–1741.

179. Webb, B. A., Aloisio, F. M., Charafeddine, R. A., Cook, J., Wittmann, T., & Barber, D. L. (2020). pHLARE: A New Biosensor Reveals Decreased Lysosome pH in Cancer Cells. *Molecular Biology of the Cell*, mbc.E20-06-0383.

180. Weber, S.C., and Brangwynne, C.P. (2012). Getting RNA and Protein in Phase. Cell *149*, 1188–1191.

181. Weinert, S., Jabs, S., Supanchart, C., Schweizer, M., Gimber, N., Richter, M., Rademann, J., Stauber, T., Kornak, U., and Jentsch, T.J. (2010). Lysosomal pathology and osteopetrosis upon loss of H+-driven lysosomal Cl- accumulation. Science *328*, 1401–1403.

182. Weiss, L.E., Naor, T., and Shechtman, Y. (2018). Observing DNA in live cells. Biochem Soc Trans *46*, 729–740.

183. Werley, C.A., Boccardo, S., Rigamonti, A., Hansson, E.M., and Cohen, A.E. (2020). Multiplexed Optical Sensors in Arrayed Islands of Cells for multimodal recordings of cellular physiology. Nat Commun *11*, 3881.

184. Wolfe, D.M., Lee, J., Kumar, A., Lee, S., Orenstein, S.J., and Nixon, R.A. (2013). Autophagy failure in Alzheimer's disease and the role of defective lysosomal acidification. Eur J Neurosci *37*, 1949–1961.

185. Wolozin, B., and Ivanov, P. (2019). Stress granules and neurodegeneration. Nat Rev Neurosci *20*, 649–666.

186. Xu, D., Joglekar, A.P., Williams, A.L., and Hay, J.C. (2000). Subunit Structure of a Mammalian ER/Golgi SNARE Complex. J. Biol. Chem. *275*, 39631–39639.

187. Xu, M., Liu, K., Swaroop, M., Sun, W., Dehdashti, S.J., McKew, J.C., and Zheng, W. (2014). A Phenotypic Compound Screening Assay for Lysosomal Storage Diseases. J Biomol Screen *19*, 168–175.

188. Yatsuzuka, K., Sato, S., Pe, K.B., Katsuda, Y., Takashima, I., Watanabe, M., and Uesugi, M. (2018). Live-cell imaging of multiple endogenous mRNAs permits the direct observation of RNA granule dynamics. Chem. Commun. *54*, 7151–7154.

189. Yip, K.W., Cuddy, M., Pinilla, C., Giulanotti, M., Heynen-Genel, S., Matsuzawa, S., and Reed, J.C. (2011). A High Content Screening (HCS) Assay for the Identification of Chemical Inducers of PML Oncogenic Domains (PODs). J Biomol Screen *16*, 251–258.

190. Yue, Y., Huo, F., Lee, S., Yin, C., and Yoon, J. (2016). A review: the trend of progress about pH probes in cell application in recent years. Analyst *142*, 30–41.

191. Zhang, B., Wang, D., Guo, F., and Xuan, C. (2015). Mitochondrial membrane potential and reactive oxygen species in cancer stem cells. Familial Cancer *14*, 19–23.

192. Zhang, R., Niu, G., Li, X., Guo, L., Zhang, H., Yang, R., Chen, Y., Yu, X., and Tang, B.Z. (2019). Reaction-free and MMP-independent fluorescent probes for long-term mitochondria visualization and tracking. Chem. Sci. *10*, 1994–2000.

193. Zhang, T., Mishra, P., Hay, B.A., Chan, D., and Guo, M. (2017). Valosin-containing protein (VCP/p97) inhibitors relieve Mitofusin-dependent mitochondrial defects due to VCP disease mutants. ELife *6*.

194. Zhou, B., Liu, W., Zhang, H., Wu, J., Liu, S., Xu, H., and Wang, P. (2015). Imaging of nucleolar RNA in living cells using a highly photostable deep-red fluorescent probe. Biosensors and Bioelectronics *68*, 189–196.

195. Zhu, H., Fan, J., Du, J., and Peng, X. (2016). Fluorescent Probes for Sensing and Imaging within Specific Cellular Organelles. Acc. Chem. Res. *49*, 2115–2126.

CHAPTER 2: A GENETICALLY ENCODED, PH-SENSITIVE MTFP1 BIOSENSOR FOR PROBING LYSOSOMAL PH

Marcus Y. Chin[1,2†], Anand R. Patwardhan[1†], Kean-Hooi Ang[2], Austin L. Wang[1], Carolina Alquezar[1], Mackenzie Welch[1], Phi T. Nguyen[3], Michael Grabe[4], Anna V. Molofsky[3], Michelle R. Arkin[2*] and Aimee W. Kao[1*]

[1]Memory and Aging Center, Department of Neurology, University of California, San Francisco, California, CA 94158, USA

[2]Small Molecule Discovery Center, Department of Pharmaceutical Chemistry, University of California, San Francisco, CA 94143, USA

[3]Weill Institute for Neurosciences, Department of Psychiatry, University of California, San Francisco, CA 94158, USA

[4]Cardiovascular Research Institute, Department of Pharmaceutical Chemistry, University of California, San Francisco, CA 94158, USA

[†] Both authors contributed equally to this manuscript

[*] Corresponding authors: aimee.kao@ucsf.edu and michelle.arkin@ucsf.edu

Key words: pH biosensor, lysosomes, ratiometric imaging, high-content analysis, neurons

ABSTRACT

Lysosomes are important sites for macromolecular degradation, defined by an acidic lumenal pH of ~4.5. To better understand lysosomal pH, we designed a novel, genetically encoded, fluorescent protein (FP) based pH biosensor called FIRE-pHLy (Fluorescence Indicator REporting pH in Lysosomes). This biosensor was targeted to lysosomes with lysosomal-associated membrane protein 1 (LAMP1) and reported lumenal pH between 3.5 and 6.0 with monomeric teal fluorescent protein 1 (mTFP1), a bright cyan pH sensitive FP variant with a pKa of 4.3. Ratiometric quantification was enabled with cytosolically oriented mCherry using high-content quantitative imaging. We expressed FIRE-pHLy in several cellular models and quantified the alkalinizing response to bafilomycin A1, a specific V-ATPase inhibitor. In summary, we have engineered FIRE-pHLy, a specific, robust and versatile lysosomal pH biosensor that has broad applications for investigating pH dynamics in aging and lysosome-related diseases, as well as in lysosome-based drug discovery.

INTRODUCTION

Lysosomes support diverse cellular functions by acting as sites of macromolecular degradation, nutrient recycling, pathogen clearance and signaling events that regulate cellular functions (Huynh et al., 2007; Lawrence & Zoncu, 2019; Mony et al., 2016; Settembre et al., 2013). Mammalian cells eliminate misfolded proteins using either the ubiquitin-proteasome system or autophagy-*lysosome pathway*. Both play indispensable roles in protein quantity and quality control in the cell (Ballabio & Bonifacino, 2020; Rousseau & Bertolotti, 2018). The degradative abilities of lysosomes are conferred by an acidic lumen (pH ~4.5-4.7) (Casey et al., 2010; Ohkuma, 1989) which contains more than fifty hydrolytic enzymes, also known as "acid hydrolases" that break down major macromolecules into building blocks that are recycled for cellular reuse (de Duve & Wattiaux, 1966; Ishida et al., 2013; Rudnick, 1987). Lysosomal acidity is maintained through the vacuolar-type H^+-ATPase (V-ATPase) proton pump, an evolutionarily conserved electrogenic pump that generates a proton gradient across membranes by coupling proton translocation with ATP hydrolysis (Beyenbach & Wieczorek, 2006). Additional contributions to lysosomal pH setpoint are made by a number of counter-ion channels and transporters (Mindell, 2012).

Lysosomal pH dynamics are broadly implicated in biological and disease pathways. Loss-of-function mammalian V-ATPase mutations are embryonic lethal (Inoue et al., 1999), highlighting the significance of lysosomal function, in particular pH, to the sustainment of life. In cancer, aberrant V-ATPase activity is linked to hyper-acidic lysosomes that promote tumor proliferation and invasion (Kallunki et al., 2013; Liu et al., 2018; Webb et al., 2011). Even relatively small alterations in the proton concentration (~0.5 – 0.9 pH units) can have dramatic effects on tumor aggressiveness (Anderson et al., 2016; Gallagher et al., 2008). In contrast, loss

of lysosomal acidity is observed in aging. Yeast vacuoles (metazoan homolog of lysosomes) and *C. elegans* lysosomes lose their acidity with increasing age (Baxi et al., 2017; Hughes & Gottschling, 2012; Sun et al., 2020), but can be rescued with caloric restriction that upregulates V-ATPase activity (Hughes & Gottschling, 2012). Additionally, neuronal health is highly regulated by lysosomal function, as demonstrated by insights from human genetics that link lysosomal dysfunction to a wide range of neurological diseases (Malik et al., 2019; Platt et al., 2012). Notably, reduced lysosomal pH is a probable key factor in the pathogenesis of familial forms of Alzheimer's disease, Parkinson's disease, prion diseases and amyotrophic lateral sclerosis (Bourdenx et al., 2016; Coffey et al., 2014; Van Acker et al., 2019; Wolfe et al., 2013). Furthermore, Alzheimer's disease-related presenilin-1 mutations have been shown to prevent proper acidification of lysosomes by inhibiting assembly of V-ATPase subunits (Fang et al., 2010; Lee et al., 2015; Wolfe et al., 2013). These studies highlight the importance of investigating lysosomal pH regulatory mechanisms in disease. Collectively, these findings have transformed our understanding of lysosomes from passive waste receptacles to dynamic participants in regulating cellular health and disease, thus making them salient therapeutic targets (Appelqvist et al., 2013).

Given the central role of pH in lysosomal function and overall cellular homeostasis, numerous types of lysosomal probes have been developed. Several small-molecule pH-sensitive dyes, organic fluorophores and synthetic probes (e.g. LysoSensor, LysoTracker, FITC-dextran, pHrodo-dextran, DAMP, quantum dots) label and measure lysosomal pH within cells (Han & Burgess, 2010; Jin et al., 2010; Ohkuma, 1989; Wan et al., 2014; X. Wang et al., 2020; Wolfe et al., 2013; Zhang et al., 2013). Wolfe *et al.*, 2013, compared the most frequently used pH probes for their sensitivity, localization and reported the limitations encountered for accurately

quantifying the very low pH values of lysosomes. However, these probes have disadvantages due to their poor specificity of subcellular targeting and cytotoxicity (e.g. LysoSensor Yellow/Blue DND-160 function at shorter wavelengths, excitation-329nm/emission-440nm) that lead to autofluorescence and imaging artifacts, modification of cellular metabolic activity, and leakage from cells (Han & Burgess, 2010; Pierzyńska-Mach et al., 2014; Tantama et al., 2011; Wolfe et al., 2013).

On the other hand, genetically encoded pH biosensors based on fluorescent proteins (FP) have many advantages such as (i) controlled expression in different cell types and tissues, (ii) enhanced intracellular specificity and (iii) bypassing of dye-incubation steps to (iv) enable long-term, live imaging studies in cells and animals. The first genetically encoded intracellular pH biosensors (called 'pHluorins') were developed through directed mutations of specific residues of green fluorescent protein (GFP) to pH-sensitive histidine residues (Miesenböck et al., 1998). The chromophores of FP are sensitive to protons revealing correlations between pH and fluorescent readout (Ashby et al., 2004). Genetically encoded biosensors have emerged as essential tools for probing cellular ions including Ca^{++} (Miyawaki et al., 1997), H^{+} (Miesenböck et al., 1998), Zn^{2+} [42], Cl^{-} (Arosio et al., 2010), Mg^{2+} (Lindenburg et al., 2013), and K^{+} (Bischof et al., 2017). Several pH-sensitive FPs have been described and targeted to inaccessible environments such as organelle lumens to measure the pH of various intracellular compartments within the secretory-endocytic pathway. Previously characterized biosensors include EGFP (pKa 6.0) to map endosomal acidification (Serresi et al., 2009), pHRed (pKa 6.6) to measure intracellular pH (Tantama et al., 2011), pHuji (pKa 7.7) for imaging exo- and endocytosis (Shen et al., 2014), and Keima (pKa 7.7) (Katayama et al., 2011), GFP-LC3 (pKa 6) or mRFP-LC3 (pKa 4.5) for detection of autophagy (Kimura et al., 2007). Additionally, Burgstaller *et al.* utilized the cyan FP

variant mTurquoise2 (pKa = 3.1) to develop a Förster resonance energy transfer (FRET) based biosensor to measure pH throughout the endomembrane system (Burgstaller et al., 2019).

Recently, two ratiometric biosensors targeted to lysosomes using lysosomal-associated membrane protein 1 (LAMP1) have been published with the following expression cassettes: (i) mCherry-pHluorin-mouseLAMP1 (Ponsford et al., 2020) and (ii) sfGFP- ratLAMP1-mCherry fusions (Webb et al., 2020). Both biosensors used LAMP1 for lysosomal targeting, but different topologies of FPs for pH sensing. The described probes have a reported pKa of ~6.5 and ~5.9, respectively. Topologically, the Ponsford *et al.* probe positioned both FP domains within the lysosome lumen while in the design of Webb *et al*. the pH-sensing sfGFP and the mCherry domain face the lumen and cytosol, respectively. Because the physiological pH of the lysosome is ~4.5, a sensor with a more acidic pKa could be more suitable for reporting the acidic pH range of lysosomes for wide-range applications.

Using the diverse toolkit of FPs (Lambert, 2019; Rodriguez et al., 2017), we engineered a mTFP1-humanLAMP1-mCherry construct, which is a dual-fluorescent cyan/red fusion protein that is targeted to lysosomes to report lysosomal pH. We call this biosensor **F**luorescence **I**ndicator **RE**porting **pH** in **Ly**sosomes, or '**FIRE-pHLy**' (Chin, Patwardhan, et al., 2021a). FIRE-pHLy showed specificity with respect to lysosomal localization and for measuring pH within a range of 3.5 to 6.0, with a calculated pKa of 4.4. The biosensor responded to *lysosome alkalinizing agents and* demonstrated *a dynamic pH response in a variety of cell types. High-content imaging of FIRE-pHLy allowed us to measure thousands of cells per condition and precisely quantify these responses.* Given the emerging attention to lysosomal pH in neurodegeneration and aging, we explored the utility of FIRE-pHLy in the context of primary neurons, human induced pluripotent stem cells (iPSCs), and neuroblastoma cells. To our

knowledge, FIRE-pHLy is the first lysosome-targeted pH biosensor that incorporates mTFP1 as its pH-sensing domain, allowing for pH measurements within the highly acidic range of physiological lysosomes. FIRE-pHLy was adapted to *in vitro* cellular models using both traditional imaging and high-content analysis.

RESULTS AND DISCUSSION

Design principles for a ratiometric lysosomal pH biosensor

To develop a reliable lysosomal pH biosensor, we have selected a ratiometric system in which the relative brightness of two reporters is used to quantify pH measurements. In this type of ratiometric, dual-reporter system, one fluorophore changes its signal in response to proton concentration while the other serves as a stable reference point for identifying lysosomes and normalizing fluorescent signals. This capability represents a significant advantage over single fluorophore biosensors that can lead to biased measurements between samples or experiments (Grillo-Hill et al., 2014; O'Connor & Silver, 2013).

For our purposes, a ratiometric lysosomal pH reporter required the following features: (1) a domain for lysosomal targeting, (2) a cytosolically facing fluorescent protein that exhibits stable brightness at physiological intracellular pH (pH range 6.8 to 7.2) (Casey et al., 2010) and (3) a lysosomal lumen-facing fluorescent protein that provides dynamic lysosomal pH sensing at highly acidic pH (pH <5.0). For lysosomal targeting, we utilized LAMP1, a type 1 membrane protein harboring a tyrosine-based lysosomal sorting motif in its short cytoplasmic tail (last 5 amino acids 'GYQTI') (Braulke & Bonifacino, 2009; Rohrer et al., 1996). For the cytosolic, pH-insensitive domain of the reporter, we tested a number of candidates and ultimately chose mCherry for its brightness and fluorescent stability at physiological intracellular pH ranges and is described in previous ratiometric studies (Cho et al., 2017; Choi et al., 2013; Grillo-Hill et al., 2014; Shaner et al., 2004).

The success of a lysosomal pH biosensor depends upon identifying a fluorescent protein that accurately reflects the highly acidic pH of the lysosome. The ideal fluorescent protein for this purpose required a low pKa to allow for pH sensing within the anticipated lysosomal pH

range from ~3.5 to 6.0. Additional major attributes in choosing a pH-sensitive fluorescent protein include high brightness, photostability and the ability to maintain proper protein folding and integrity within the acidic lysosomal environment. After testing different candidates, we selected mTFP1 (monomeric teal fluorescent protein 1). A variant of cyan fluorescent protein, mTFP1 possesses a pKa of 4.3 as well as a robust sigmoidal pH response, as measured in cell-free conditions, across a broad acidic and alkaline pH range (Ai et al., 2006). Additionally, mTFP1 resists common FP pitfalls such as photobleaching and aggregation (Shinoda et al., 2018). Thus, mTFP1 offers a suitable balance of favorable attributes for the pH-sensitive aspect of a ratiometric pH biosensor. The physicochemical properties of mTFP1 and mCherry are described in **Table 2.1** (Ai et al., 2006; Cranfill et al., 2016; Shaner et al., 2004).

Table 2.1. Physicochemical properties of mTFP1 and mCherry.

	mTFP1	**mCherry**
Excitation Maximum λ_{max} (ex) (nm) (a)	462	587
Emission Maximum λ_{max} (em) (nm) (b)	492	610
Extinction Coefficient ε ($M^{-1}cm^{-1}$) max(c)	64,000	72,000
Quantum Yield (QY) (d)	0.85	0.22
Filter set (e)	FITC, GFP, Alexa488	TRITC, mCherry, CY3
Brightness (f)	54.4	15.84
pKa (g)	4.3	4.5
Photostability t1/2 (s) (h)	163.0	68.0
Oligomerization	Monomer	Monomer
Origin	*Clavularia sp.*	*Discosoma sp.*
References	53, 63	53, 62

FITC, fluorescein isothiocyanate; GFP, green fluorescent protein; TRITC, tetramethylrhodamine; CY3: cyanine-3.

(a) Excitation wavelength in nanometers
(b) Emission wavelength in nanometers
(c) A measure of how strongly the protein absorbs light at a given wavelength
(d) Ratio of photons emitted to photons absorbed
(e) Fluorescence filter cubes compatible for measurements
(f) Product of Extinction Coefficient and Quantum Yield
(g) pH at which fluorescence intensity drops to 50% of its maximum value
(h) Time (seconds, s) to bleach to 50% emission intensity, at an illumination level that causes each molecule to emit 1,000 photons/s initially, that is, before any bleaching has occurred

The assembled chimeric fluorescent protein construct consisted of an N-terminal, lysosomal lumen-facing, pH-sensitive mTFP1 fused to the transmembrane portion of human LAMP1 (hLAMP1) and a C-terminal, pH-insensitive mCherry outside the lysosome (**Fig. 2.1A, 2.1B**). A flexible linker (GGSGGGSGSGGGSG), rich in small and polar amino acids, was added between mTFP1 and LAMP1 to promote correct protein folding and retention of biological and fluorescence properties (X. Chen et al., 2013). To allow correct sorting, maintain a fixed distance between the two proteins and minimize mCherry aggregation, a rigid linker (PAPAPAP) was placed between LAMP1 and mCherry (X. Chen et al., 2013; Shemiakina et al., 2012). Expression of the construct was driven by the human cytomegalovirus (CMV) or human ubiquitin C (UbC) promoter cloned within pLJM1 lentivirus backbone. We designated the resulting chimeric fluorescent protein as FIRE-pHLy, for Fluorescence Indicator REporting pH in Lysosomes.

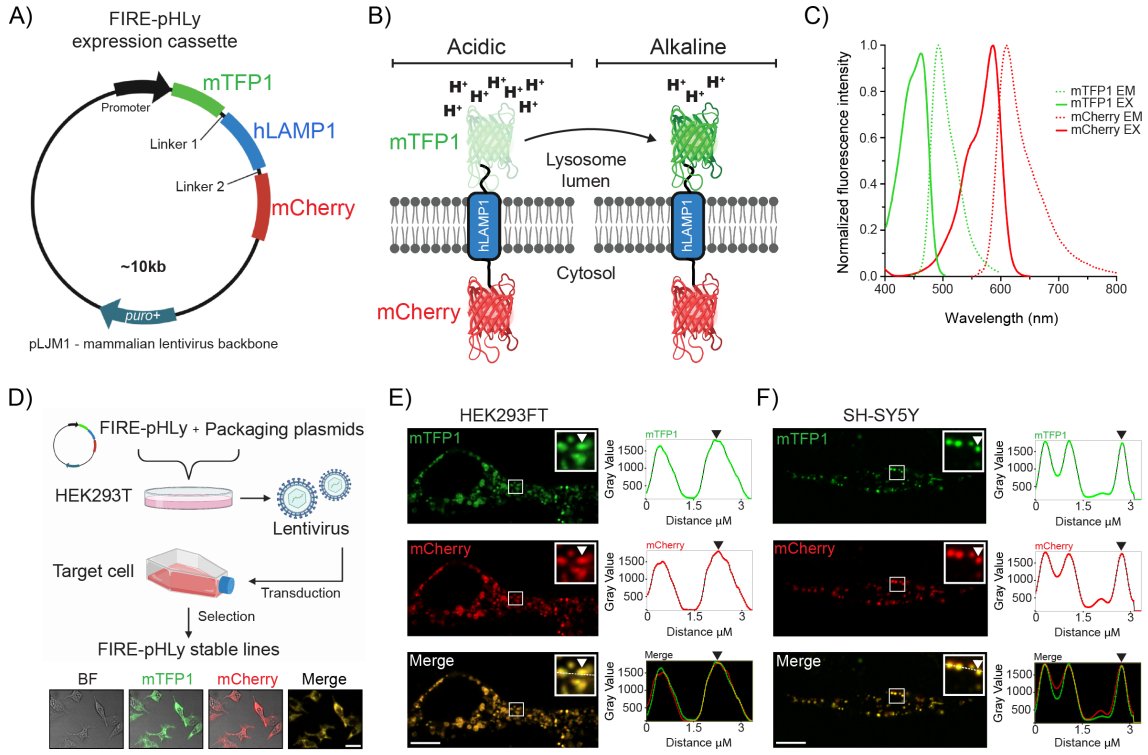

Figure 2.1. Design of FIRE-pHLy, a ratiometric lysosomal pH biosensor
(A) Design of FIRE-pHLy expression cassette driven by the CMV promoter (in HEK293FT cells) or human UbC promoter (in SH-SY5Y cells) cloned in the lentiviral pJLM puromycin-resistant plasmid. Chimeric protein (N- to C-terminus) mTFP1-hLAMP1-mCherry is targeted to lysosomes via the type-I transmembrane human LAMP1 peptide sequence. Linker regions 1 (GGSGGGSGSGGGSG) and 2 (PAPAPAP) allow proper folding and expression of each protein portion. (B) Representation of FIRE-pHLy expressed on lysosomal membranes and mTFP1 fluorescence levels in acidic and alkaline conditions. Lysosomal pH-sensitive mTFP1 located within the lumen and lysosomal pH-insensitive mCherry is located on the cytosolic side. (C) Excitation (solid lines) and emission spectra (dashed lines) for mTFP1 and mCherry. The 470 nm and 587 nm laser lines were used to excite mTFP1 and mCherry, respectively. Spectra values were obtained and adapted from FPbase (Lambert, 2019). Refer to **Table 2.1** for physicochemical properties of FIRE-pHLy FPs. (D) Workflow of generating stable FIRE-pHLy cell lines using lentiviral vectors. Representative low magnification confocal fluorescence images of brightfield (BF), mTFP1 (green), mCherry (red) and merged channels (yellow) in stable FIRE-pHLy-expressing HEK293FT cells. Scale bar = 25 μm (E-F) Live imaging frames of FIRE-pHLy expressing stable cells (E) HEK293FT and (F) SH-SY5Y with zoomed inset highlighting mTFP1 and mCherry puncta (white arrowhead) and corresponding linescan intensity profile measured along the white line (right panel). Scale bars = 10 μm.

Spectral compatibility is important in dual-color, ratiometric reporters. **Fig. 2.1C** shows the reported peak excitation and emission wavelengths for mTFP1 (462 and 492 nm, respectively) and mCherry (587 and 610 nm, respectively) (Ai et al., 2006; Lambert, 2019; Shaner et al., 2004). To assess bleed-through, we experimentally compared the crosstalk and cross-excited mTFP1 and mCherry with both 470 nm and 587 nm laser lines. mTFP1 was excited at 470 nm and detected in the mCherry channel. Similarly, mCherry was excited at 587 nm and detected in the mTFP1 (green) channel (**Fig. 2.2**). In both the cases, the results show minimal crosstalk, demonstrating that mTFP1 and mCherry exhibited suitable spectral compatibility for ratiometric imaging.

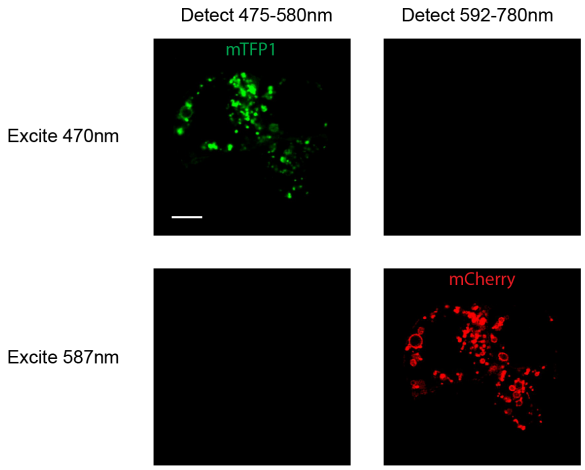

Figure 2.2. Cross excitation of mTFP1 and mCherry.
Confocal images of FIRE-pHLy-expressing HEK293FT cells. mTFP1 is excited at 470 nm and detected between 475-580 nm, but not between 592-780 nm. Conversely, mCherry is excited at 587 nm and detected between 592-780 nm, but not between 475-580 nm. Scale bar = 10 μm.

Using lentiviral transduction, FIRE-pHLy was stably expressed in human embryonic kidney 293 (HEK293FT) cells and SH-SY5Y neuroblastoma cells (**Fig. 2.1D)**. We then investigated the subcellular expression pattern with live imaging (**Fig. 2.1E, 2.1F**). Live imaging frames of the basolateral imaging section showed that mTFP1 puncta localized to the same structures as mCherry as highlighted by line scan analysis (**Fig. 2.1E, 2.1F**). Furthermore, simultaneous two-channel live acquisition video shows colocalization of mTFP1 and mCherry-positive structures and their concomitant movement over time (**Fig. 2.3**). Finally, we probed the lysates of FIRE-pHLy-expressing cells with an anti-LAMP1 antibody to confirm the size of the sensor between ~130-160kD (**Fig. 2.4**). The two broad bands seen in the LAMP1 immunoblot suggest that the sensor is glycosylated, which was also seen in the sensor by Webb and colleagues(Webb et al., 2020). Taken together, the microscopic and biochemical evaluation results confirm successful expression of the FIRE-pHLy cassette in HEK293FT and SH-SY5Y cells.

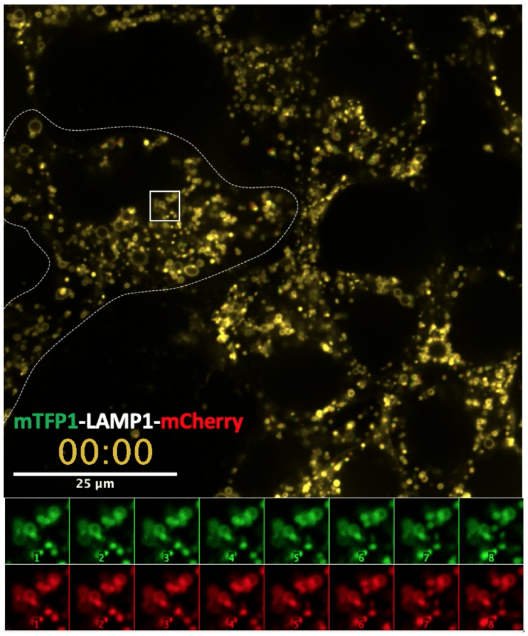

Figure 2.3. Expression and live imaging of FIRE-pHly in HEK293FT stable cells.
Time-lapse merged video stills acquired using spinning-disc confocal microscopy on HEK293FT stable cells expressing chimeric construct encoding FIRE-pHLy. Note the consecutive time-lapse images (first 8 frames, lower panel) where mTFP1 (green) positive dynamic structures colocalize and show concomitant movements with mCherry (red) labeled LAMP1 positive lysosomes. Simultaneous acquisition using GFP/mCherry channel with 100 ms exposure, video was shown at 7 frames/s. Scale bar = 25 µm.

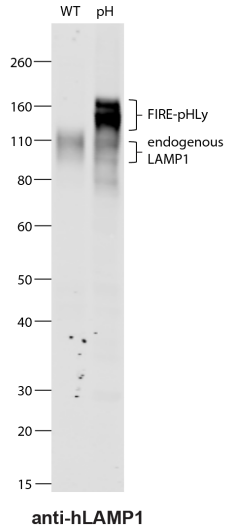

Figure 2.4. Western blot analysis of FIRE-pHLy expression in HEK293FT cell lysates.
Lysates from wild-type (WT) and FIRE-pHLy-expressing (pH) HEK293FT cells were immunoblotted with an anti-hLAMP1 antibody to detect pH sensor expression levels. The observed FIRE-pHLy molecular weight (MW) is ~130-160 kD. The observed MW of LAMP1 due to glycosylation is ~90-120 kD (note: calculated MW of LAMP1 is ~40 kD). The MWs mTFP1 and mCherry are 27 kD each. Protein loading: 20 ug/lane.

FIRE-pHLy specifically localized to lysosomal compartments

We first investigated whether FIRE-pHLy expressed in HEK293FT cells sorted to lysosomal compartments. To do so, we tested colocalization of FIRE-pHLy with lysosomal, endosomal and mitochondrial sub-cellular markers (**Fig. 2.5A-E**). Cells were imaged using immunofluorescence confocal microscopy with three laser channels. Subsequently, we quantified the colocalization of FIRE-pHLy (using mCherry as reference) with existing markers for various sub-cellular organelles. We first assessed lysosomal markers by immunostaining for endogenous LAMP1 or LAMP2 or using LysoTracker Deep Red dye (Lyso-647). LAMP1 and LAMP2 are among the most abundant lysosome-associated membrane proteins (Eskelinen, 2006; Saftig & Klumperman, 2009). Endogenous LAMP1 and mCherry showed a strong positive correlation ($r = 0.74 \pm 0.03$) (**Fig. 2.5A, 2.5F**). Similarly, LAMP2, a well characterized regulator of autophagy (Tekirdag & Cuervo, 2018), colocalized with mCherry ($r = 0.67 \pm 0.04$) (**Fig. 2.5B, 2.5G**). Lyso-647 is a widely used commercially available fluorescent probe that preferentially accumulates in acidic vesicular compartments, such as late endosomes and lysosomes (Chazotte, 2011). Co-localization of Lyso-647 and mCherry was similar to LAMP2 ($r = 0.63 \pm 0.03$) (**Fig. 2.5C, 2.5H**). On the contrary, early endosome antigen 1 (EEA1) is a membrane-bound protein found specifically on early endosomes (Mu et al., 1995) and its labeling is characterized by large distinct ring-like structures (Wilson et al., 2000). In contrast to the lysosomal markers, a lower fraction of mCherry associated with EEA1 ($r = 0.41 \pm 0.02$) (**Fig. 2.5D, 2.5I**) likely reflecting the maturation of FIRE-pHLy through the highly dynamic endolysosomal continuum (Jovic et al., 2010). Finally, MitoTracker Deep Red (Mito-647) was used to stain mitochondria as a negative control (**Fig. 2.5E, 2.5J**). Most Mito-647 exhibited minimal colocalization with FIRE-pHLy ($r = 0.26 \pm 0.03$). The small percentage of colocalization was anticipated because mitochondria-

lysosome crosstalk is known to occur (Deus et al., 2020; Lahuerta et al., 2018).

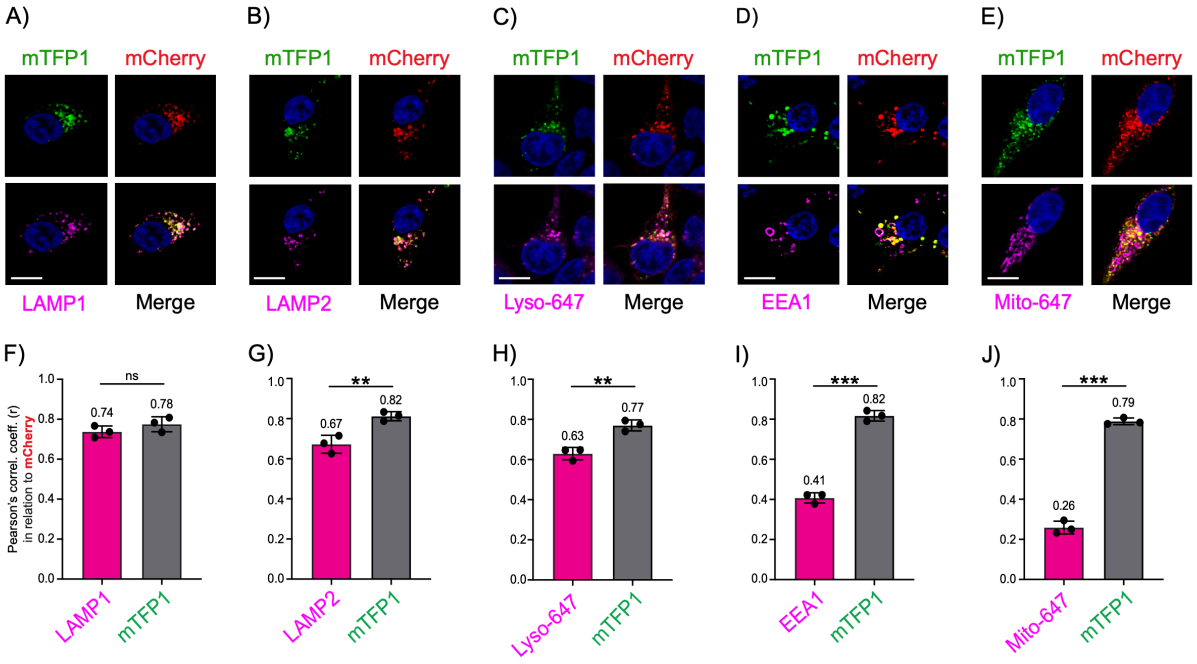

Figure 2.5. FIRE-pHLy localizes to lysosomal compartments.
(A-E) Representative images of FIRE-pHLy-expressing HEK293FT cells stained with various markers (shown in magenta). (A) LAMP1 (lysosomal membranes), (B) LAMP2 (lysosomal membranes), (C) LysoTracker Deep Red or Lyso-647 (acidic compartments), (D) EEA1 (early endosomes), (E) MitoTracker Deep Red or Mito-647 (mitochondria). Nuclei are shown in blue. Scale bars = 10 µm. (F-J) Pearson's correlation coefficients (r) calculated using the ImageJ plugin JACoP (Just Another Colocalization Plugin). Each graph shows a different marker colocalized with mCherry (magenta bars) and mTFP1 colocalized with mCherry (gray bars). Data points represents mean ± S.D. (3 independent replicates; n = 15 cells/replicate. Statistical analysis was performed using two-tailed, unpaired Student's t-test. **p ≤ 0.01; ***p ≤ 0.001; ns = not significant).

As expected, since they are co-expressed as the same fusion protein, mTFP1 and mCherry showed consistently strong positive Pearson's correlation coefficient values (within the range r = 0.78 – 0.82) across all images (**Fig. 2.5F-J**, gray bars). These coefficient values are less than 1.0 possibly due to mTFP1 quenching at physiological pH in lysosomes. Taken together, we concluded that mTFP1 and mCherry highly colocalizes with each other, as well as that FIRE-pHLy traffics through the endolysosomal sorting pathways to localize predominantly in lysosomal membranes.

Quantification & visualization of pH-dependent, mTFP1 fluorescence in live cells

After confirming correct localization of FIRE-pHLy, we sought to demonstrate its pH sensitivity. Measuring intracellular and intralumenal pH of lysosomes using the ionophores, nigericin and monensin, is well established in previous protocols (Canton & Grinstein, 2017; Grillo-Hill et al., 2014; Harned et al., 1951; Ma et al., 2017; Ponsford et al., 2020; Webb et al., 2020; Wolfe et al., 2013) and is currently the standard in the field (**Fig. 2.6A**). Nigericin (K^+/H^+) and monensin (Na^+/H^+) exchange K^+ (and to a lesser extent Na^+) for H^+ across cell membranes, thus equilibrating external pH with that of the lysosomal lumen (Harned et al., 1951; Wolfe et al., 2013). Adapting these methods, we first used glass bottom chamber slides to qualitatively assess mTFP1 and mCherry fluorescence (using standard 488/561 nm filter sets) changes in HEK293FT cells at the applied pH values from 3.0 to 7.0. The fluorescence of mTFP1 increased from pH 3.0 to 7.0 while mCherry fluorescence remained relatively stable (**Fig. 2.6B**).

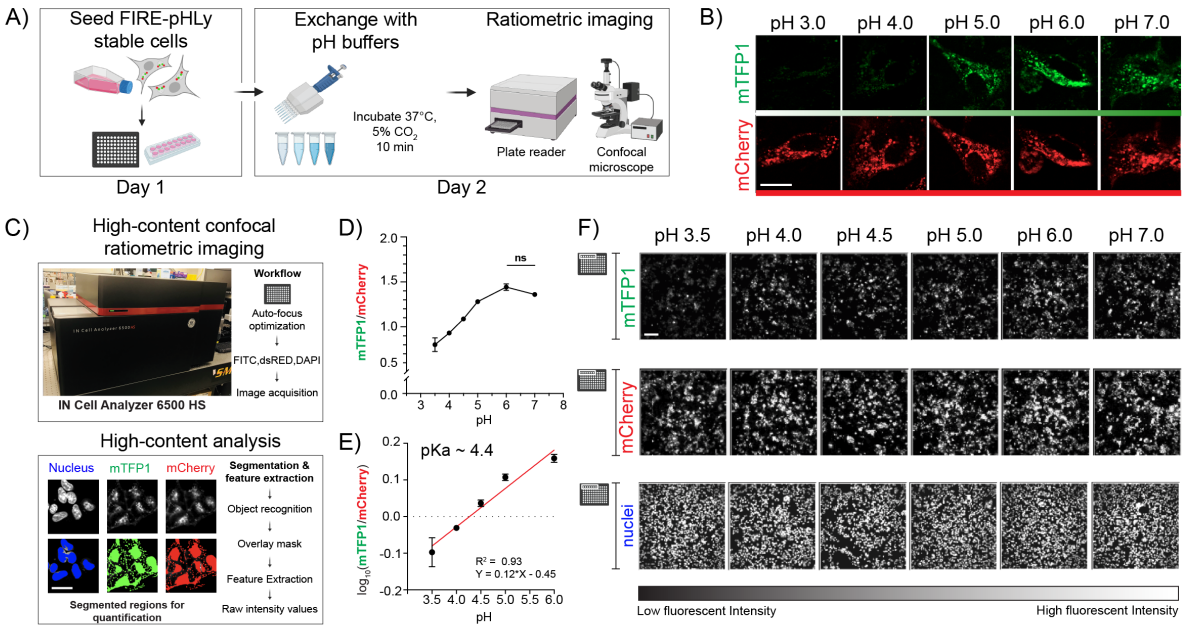

Figure 2.6. FIRE-pHLy biosensor responds to pH changes and is quantifiable with high-content analysis.
(A) Workflow for pH calibration protocol. FIRE-pHLy-expressing cells were seeded into assay wells. Media was exchanged with pH buffers (at indicated values) supplemented with 10 μM nigericin and 1X monensin and was allowed to incubate for 10 min. Cells can be imaged live on either a confocal microscope or high-content plate reader. (B) Representative individual channel images of FIRE-pHLy-expressing HEK293FT cells imaged live by spinning disk confocal microscopy. Scale bar = 20 μm. (C) High-content analysis to quantify FIRE-pHLy fluorescence. Images were acquired on a plate-based confocal imager and analyzed on a custom-built segmentation protocol (see Methods). Masks for nucleus and FIRE-pHLy fluorescence were created and average mTFP1/mCherry ratios were calculated. (D) Cells were analyzed according to (C) and mTFP1/mCherry ratios were plotted against pH. Data points are presented as mean ± S.D., from 4 independent replicates; n = ~10,000 cells quantified per pH value. Tukey's test for multiple stepwise comparisons indicated significance between all pH groups, except 6.0 and 7.0. (E) Log_{10}(mTFP1/mCherry) values between pH 3.5 and 6.0 were fit to a linear equation ($R^2 = 0.93$). The pKa of FIRE-pHLy (in cells) was calculated to be ~4.4. (F) Grayscale images of mTFP1, mCherry and nuclei taken from one random field of one representative assay well (of 96 well plate) at indicated pH values. Scale bar = 50 μm.

In order to increase the precision of measuring pH in a larger cell population, we adapted the assay to a high-content plate-based format. We built a lysosomal segmentation protocol (see Methods) that extracted fluorescence intensities of mTFP1 and mCherry, as well as nucleus count (**Fig. 2.6C**). From this analysis, we captured data from over 10,000 cells across four independent replicates at the applied pH values of 3.5 to 7.0 in 96-well plates (**Fig. 2.6C-F**) (see Methods). To quantify lysosomal pH, fluorescence intensity ratios for mTFP1 and mCherry (mTFP1/mCherry) were calculated and plotted according to the pH of the buffer. The ratio curve exhibited a significant positive relationship with pH, showing a ~1.7-fold change in fluorescence ratio between pH 3.5 and 6.0 (**Fig. 2.6D**). Additional data indicates that mTFP1 fluorescence was the sole driver of the pH-dependent FIRE-pHLy ratio change (**Fig. 2.7**). Log_{10} transformation of ratios is linear from pH 3.5 to 6.0 ($R^2 = 0.93$) (**Fig. 2.6E**).

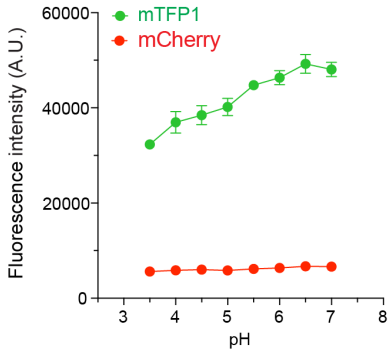

Figure 2.7. Measured fluorescence intensities of FIRE-pHLy FPs in cells calibrated with pH buffers.
Individual mTFP1 and mCherry fluorescence intensities plotted against pH (3.5-7.0). FIRE-pHLy-expressing HEK293FT cells were incubated with pH buffers (3.5-7.0) supplemented with 10 μM nigericin and 1X monensin and imaged with a high-content plate reader. Data points are presented as mean ± S.D., from 6 independent wells; n = ~10,000 cells quantified per pH value.

It is noteworthy that though commonly used, the nigericin method has limitations. Equilibrating pH across membranes may affect the fluorescence intensity of both fluorophores. This sets a lower bound for pH calibration because the mCherry fluorophore is exposed to low pH. Furthermore, this method assumes that the applied pH represents the same pH to which mTFP1 was exposed. To validate the environment of mTFP1, we calculated the pKa of our ratiometric sensor to be ~4.4 using a modified Henderson-Hasselbalch equation (Hoffmann & Kosegarten, 1995). This was in concordance with the *in vitro* mTFP1 pKa of ~4.3 (Ai et al., 2006), suggesting that the pH of the lysosome was very similar to the pH of the applied buffer. Given the calibration challenges at low pH, we can establish that the fluorescence of FIRE-pHLy is sensitive to the applied pH in the range of 3.5 to 6.0; this range is appropriate for measuring pH in lysosomes under physiological conditions. Taken together, FIRE-pHLy fluorescence correlates with lumenal pH values in lysosomes.

Functional validation of FIRE-pHLy in different cell types

Next, we evaluated the ability of FIRE-pHLy to monitor lysosomal pH under physiological conditions and pharmacological perturbations in widely used neurodegenerative disease cell models. We quantified the alkalinizing response to bafilomycin A1 (BafA1), a specific V-ATPase inhibitor, which functions by binding to the V0c subunit, thus blocking proton translocation (Dröse & Altendorf, 1996). To select an appropriate BafA1 dose, we first tested multiple doses (30 nM to 1000 nM) in FIRE-pHLy-expressing HEK293FT cells and compared the sensor fluorescence to a pH calibration curve (**Fig. 2.8A-C**).

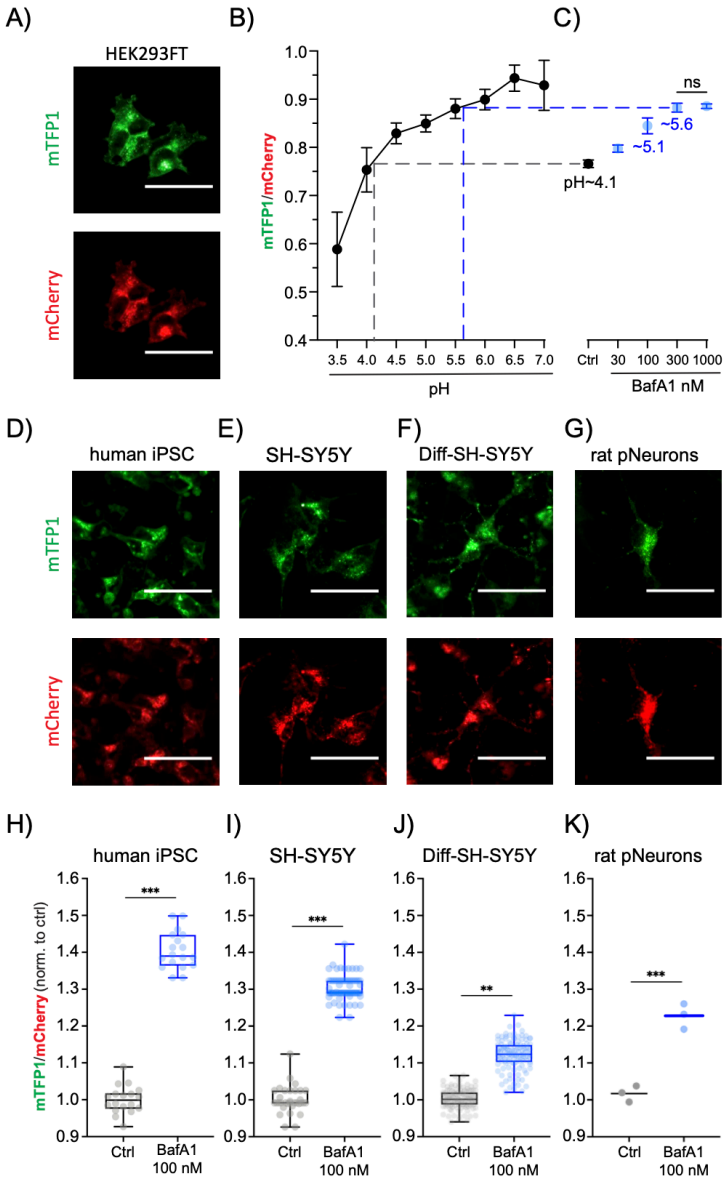

Figure 2.8. ***In vitro*** **FIRE-pHLy models and relative pH measurements with bafilomycin A1.**
(A) Ratiometric images of 2% PFA-fixed FIRE-pHLy-expressing HEK293FT cells taken on a high-content imaging system (described in Fig. 3). (B) pH calibration curve generated from cells incubated with pH buffer (pH 3.5 – 7.0) and fixed with 2% PFA post 10min of treatment. Data points are presented as mean ± S.D., from 4 independent replicates; n = 10,000 quantified cells per pH value. (C) mTFP1/mCherry ratios of FIRE-pHLy-expressing HEK293FT cells treated with bafilomycin (BafA1 30 nM to 1000 nM) and 0.1% DMSO solvent control (Ctrl) for 6 hours prior to fixation and imaging. Data points are presented as mean ± S.D., from 6 independent replicates; n = 10,000 quantified cells per condition. Tukey's test for multiple stepwise comparisons indicated significance between all groups including control, except BafA1 300 nM and 1000 nM. (D-G) Individual channel images (left to right) of FIRE-pHLy stably expressed in human iPSCs, SH-SY5Y, differentiated SH-SY5Y, and late embryonic rat hippocampal neuronal cells. All cells were fixed with 2%PFA prior to image acquisition. (H-K) 100 nM bafilomycin A1 was treated on cells for 6 hours and compared to 0.1% DMSO. Box-and-whisker plots show median, interquartile range (25th-75th percentile) and maximum/minimum values of mean ratios per well. (H) human iPSC; 18 independent wells in 96-well format; n = ~15,000 quantified cells per well. 3 biological replicates. (I) SH-SY5Y; 76 independent wells in 384-well format; n = 2,500 cells per well. 2 biological replicates (J) RA-differentiated SH-

SY5Y; 120 independent wells; n = 5,000 quantified cells per well. 4 biological replicates. (K) primary rat hippocampal neurons; 3 independent wells; n = 6,500 quantified cells per well. 1 biological replicate. Statistical analysis was performed using two-tailed, unpaired Student's t-test. **p ≤ 0.01; ***p ≤ 0.001; ns = not significant. All scale bars = 25 μm.

To enable comparisons between samples (or potential high-throughput drug screening applications), we adapted the pH calibration protocol to fixed cells. Fixation led to 33.3% reduction of mTFP1 fluorescence and 10.6% reduction of mCherry fluorescence (**Fig. 2.9**), but did not change the overall ability to sense pH in the range of 3.5 to 6.0. For this experiment, the calibration dynamic range became tighter showing a 1.59-fold change instead of 1.7-fold (**Fig. 2.8D**). Lysosomal pH increased dose-dependently with BafA1 concentration, plateauing at 300 nM with a pH~5.6 compared to the control-treatment group pH of ~4.1. Analysis of individual mTFP1 and mCherry fluorescence intensities under BafA1 treatment, confirmed that only mTFP1 fluorescence varies with lysosomal pH change (**Fig. 2.10**). A similar alkalinizing trend was observed in HEK293FT cells treated for 6 hours with 0.5 μM concanamycin A, another specific V-ATPase inhibitor (Li et al., 2013) and with 30 μM chloroquine, a lysosomotropic drug known to inhibit autophagy and enlarge lysosomes (Mauthe et al., 2018) (**Fig. 2.11**).

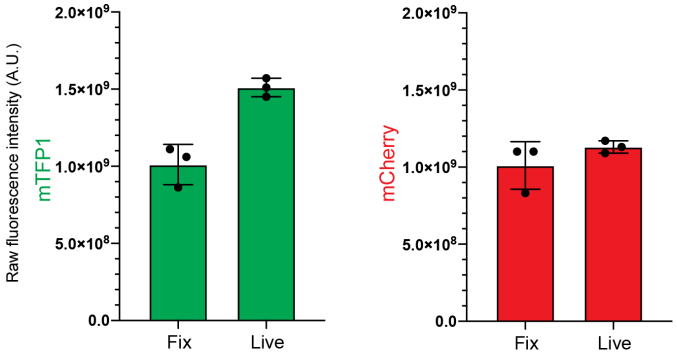

Figure 2.9. Fixed- and live-cell fluorescence measurements for mTFP1 and mCherry FPs.
Raw mTFP1 and mCherry fluorescence intensities measured from FIRE-pHLy-expressing HEK293FT cells that were either imaged live (in culture media, pH 7.4) or post-PFA fixation (in PBS, pH 7.4). Data points are presented as mean ± S.D., from 3 independent wells; n = ~5,000 quantified cells per well.

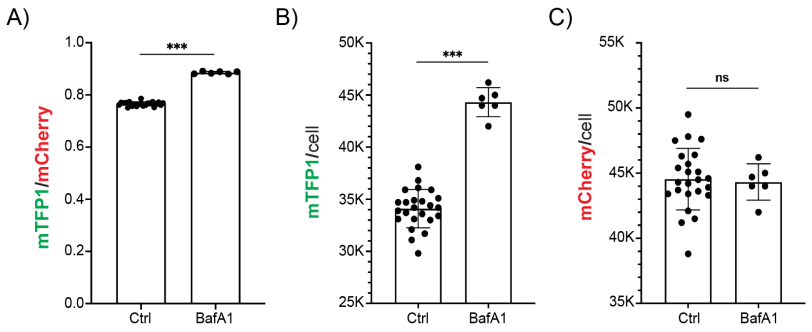

Figure 2.10. Ratiometric validation of individual FIRE-pHLy fluorophores under BafA1 conditions.
(A) mTFP1/mCherry ratio quantified from FIRE-pHLy-expressing HEK293FT cells treated with 1 µM bafilomycin for 6 hours compared to 0.1% DMSO solvent control. (B) mTFP1 mean fluorescence intensity normalized by cell count. (C) mCherry mean fluorescence intensity normalized by cell count. Data points are presented as mean ± S.D., from 6 independent replicates; n=quantified 7,500 cells per replicate. Statistical analysis was performed using two-tailed, unpaired Welch's t-test for unequal variances. ***$p \leq 0.001$; ns = not significant.

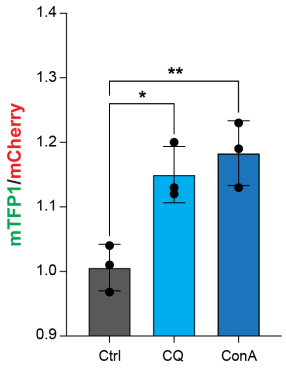

Figure 2.11. pH elevation with lysosomal pharmacological inhibitors.
Ratiometric measurements (mTFP1/mCherry) taken from FIRE-pHLy-expressing HEK293FT cells treated with 0.1% DMSO (Ctrl), 30 µM chloroquine (CQ) and 0.5 µM concanamycin A (ConA) for 6 hours before fixation. Data points are presented as mean ± S.D., from 3 independent wells; n = ~5,000 quantified cells per well. Statistics were conducted with one-way ANOVA for multiple comparisons. *$p \leq 0.05$; **$p \leq 0.01$.

Having established 100 nM as an appropriate BafA1 dose, we then probed for pH changes in induced pluripotent stem cells (iPSCs), SH-SY5Y neuroblastoma cells, retinoic acid-differentiated SH-SY5Y neuron-like cells and primary rat neurons (**Fig. 2.8D-G**), which were generated using lentiviral transduction of FIRE-pHLy. For transduction into these cells, the CMV promoter was exchanged for an UbC promoter-driven lentiviral FIRE-pHLy construct, since CMV is silenced by DNA methylation during differentiation and shows weak activity in certain cell types including iPSCs (Brooks et al., 2004; Meilinger et al., 2009). Cells were treated

with 100 nM BafA1 for 6 hours, fixed and subjected to high content analysis. Comparisons of mTFP1/mCherry fluorescence ratios with and without BafA1 treatment confirmed that FIRE-pHLy detected lysosomal alkalization across all cell lines tested (**Fig. 2.8H-K)**. The iPSCs had the largest ratio change of ~40.4 ± 1.4% compared to control. On the other hand, differentiated SH-SY5Y cells had the smallest change. Though the change in ratio was only ~11.9 ± 0.43%, using high-content analysis of over 5,000 cells, this change was statistically significant ($p \leq 0.01$). Potential explanations for the observed cell type differences in the extent of relative pH response include differential BafA1 sensitivity or basal pH set point. For example, the expression and activity of V-ATPases is regulated differentially in mammalian cells (Toei et al., 2010). Cell type-dependent pH regulatory and compensatory mechanisms warrant further investigation.

Overall, our data demonstrates that FIRE-pHLy can be targeted to lysosomes in multiple neurodegenerative disease cell models. This opens future avenues to profile lysosomal pH dynamics in cellular systems harboring different genetic mutations and further use for applications in lysosome-based drug discovery.

CONCLUSIONS

In summary, we have developed FIRE-pHLy, a genetically encoded ratiometric pH biosensor that localizes to lysosomal membranes and measures lumenal pH within physiological ranges (3.5 to 6.0). FIRE-pHLy responds robustly to pH changes and is amenable to stable integration to multiple cellular models, including differentiated and primary cells. Moreover, FIRE-pHLy is amenable to live- and fixed-cell assays, as well as both high-resolution confocal microscopy and quantitative high-content imaging. We anticipate that FIRE-pHLy will be applied to elucidate pH dynamics in basic lysosomal biology and disease. Moreover, the ability to quantifiy the sensor in 96-well plates with high-content analysis enables its translation to phenotypic-screening platforms for drug discovery in fields such as neuroscience, immunology and cancer biology. Finally, this study opens new avenues to profile lysosomal functions in animal models of childhood or age-associated neurological diseases.

METHODS

Construction of Fluorescence Indicator REporting pH in Lysosomes (FIRE-pHLy)

The genetically encoded FIRE-pHLy reporter cassette consists of the following coding segments, from the N-terminus: CMV-human LAMP1 signal peptide (84bp) – mTFP1 – flexible linker 1 (GGSGGGSGSGGGSG) – human LAMP1 – rigid linker 2 (PAPAPAP) - mCherry. Source of different elements are as follows: LAMP1 signal peptide and human LAMP1 were PCR amplified from LAMP1-mGFP (Addgene Plasmid #34831, kind gift from the Mark Von Zastrov lab, University of California, San Francisco, UCSF), mTFP1 amplified from mTFP1-pBAD (Addgene Plasmid #54553), mCherry amplified from pcDNA3.1-mCherry (Addgene Plasmid #128744). The DNA segments were PCR amplified (Phusion High-Fidelity PCR Master Mix, NEB, UK, #M0531) and fused with Gibson recombination cloning method (Gibson Assembly Master Mix, NEB, UK, #E2611) in pEGFP-N3 empty backbone. The linker sequences were incorporated into the primer sequences. The FIRE-pHLy expression cassette was cloned into lentiviral vectors with CMV promoter (pLJM1-EGFP; Addgene Plasmid #19319) and hUbC promoter (FUGW; Addgene Plasmid #14883) by Epoch Life Science services (Sugar Land,Texas, USA).

Cell culture and lentiviral transduction

All cells were cultured at 37°C with 5% CO_2 atmosphere and maintained under standard procedures. HEK293FT cells (Thermo Fisher Scientific; Carlsbad, CA, USA, #R70007) were cultured in Dulbecco's Modified Eagle medium (DMEM; Life Technologies, Carlsbad, CA, USA, #11-995-073) with 10% heat-inactivated fetal bovine serum (FBS; Gemini Bio, Sacramento, CA, USA, #GEMZR039) containing 1% penicillin and streptomycin (pen/strep)

(Gibco; Thermo Fisher Scientific, Inc., Waltham, MA, USA, #15140122) with 500 μg/mL G418 sulfate antibiotic (Thermo Fisher Scientific, #11811031). SH-SY5Y cells (American Type Culture Collection; ATCC, Maryland, USA, #CRL-2266) were maintained in 1:1 Eagle's Minimum Essential Medium (EMEM; ATCC, #30-2003) and F12 medium (Life Technologies; Carlsbad, CA, USA, #11765062) with 10% FBS and 1% pen/strep. Cells were trypsinized with 0.05% Trysin-EDTA solution (Sigma, St. Louis, MO, USA, #T4049) during routine passaging. Lentivirus production and titer assessments of FIRE-pHLy-lentivirus were performed by the UCSF ViraCore facility. For lentivirus transduction, HEK293FT and SH-SY5Y cells were plated in 6-well plates and cultured to ~70% confluence. Protocol was modified for iPSCs and primary rat neurons (see below). Lentivirus infections were carried out in the presence of 10 μg/mL of polybrene (Sigma, St. Louis, MO, USA, #S2667) in complete media. 48 hours post-transduction, cells were selected with 1 μg/mL puromycin (Millipore; Carlsbad, CA, USA, #540411) to generate stable transgene-expressing cell lines. Long-term transgene expression was maintained by selecting for resistance to puromycin at a final concentration of 1 μg/mL. SH-SY5Y cells were sorted for green and red positive fluorescence signal on a SH800S Cell Sorter (Sony Biotechnology) at the UCSF Laboratory of Cell Analysis.

Generation of FIRE-pHLy-expressing iPSCs

The F11350 iPSC line was obtained from the laboratory of Celeste Karch at Washington University School of Medicine (Karch et al., 2019). Cells were maintained in matrigel (Corning, #354277) coated plates using mTSER media (StemCell Technologies, Vancouver, Canada, #05850), which was replaced every day. During passaging, cells were lifted using Accutase (ThermoFisher Scientific, #A1110501) and then replated in media supplemented with 10 μM

ROCK inhibitor (Y-27632, StemCell Technologies, #72304). For the transduction of the virus, iPSCs were plated onto matrigel-coated 24-well plates at a density of 50,000 cells per well. Serial dilutions of the UbC promoter FIRE-pHLy lentiviral vector were prepared in mTSER media with 4 μg/ml polybrene (Sigma, #S2667) Lentivirus media was allowed to transduce cells for 24 hours and then fresh media changes were performed every day until 80% confluence was reached. Clonal populations of green/red fluorescence positive cells were manually selected and transferred into separate wells for expansion.

Isolation of primary rat neurons and FIRE-pHLy lentivirus transduction

Wildtype SAS Sprague Dawley rats (Charles River Laboratories, Wilmington, MA, USA) and isolation reagents were a kind gift from the Molofsky Lab (UCSF). Embryos staged at day 18 were dissected from one pregnant rat and immediately placed in chilled brain dissection buffer (HBSS-Ca^{2+}/Mg^{2+}-free with 10 mM HEPES buffer, pH 7.3). Brains were removed from 5 individual embryos and hippocampi halves were isolated after removal of the meninges. Hippocampi were digested with trypsin/EDTA solution and DNAase at 37°C incubation for 25 min. Quenching buffer (HI-OVO diluted 1:5 in HBSS-Ca^{2+}/Mg^{2+}-free, with 50% glucose, ovomucoid, bovine serum albumin, and DNAase) was subsequently added to inhibit trypsin digestion. Following centrifugation and buffer removal, culture medium I (DMEM-high glucose, L-glutamine-sodium pyruvate free) supplemented with 10% fetal calf serum (FCS) (not heat activated) was added to partially digested hippocampi. Cells were then manually dissociated and plated in poly-D-lysine coated 96-well plates (Greiner Bio-One, Kremsmünster, Austria, #655956) at a density of 15,000 cells per well. After 24 hours, media was replaced with culture medium II (Neurobasal medium, 1% heat inactivated FCS, 2% B27 supplement, 1X Glutamax I,

1X MycoZap plus, and 15mM NaCl). At DIV 5 (5 days in vitro), 5 μM 5-Fluorouracil was added to curb glial cell proliferation. At DIV 7, neurons were transduced with UbC-FIRE-pHLy lentivirus for 24 hours. Half media changes were performed every two days until DIV 14.

RA-differentiation of FIRE-pHLy SH-SY5Y neuroblastoma cells

SH-SY5Y cells were seeded in collagen type I-coated μClear 96-well plates (Greiner Bio-One, #655956) at a density of 10,000 cells/cm^2 24 hours before start of differentiation. Differentiation media was composed of 10 μM of retinoic acid (RA) (Sigma, #R2625) in EMEM/F12 media supplemented with 10% FBS and 1% P/S. After 6 days of RA treatment, cells were treated for 4 days with 50 ng/mL of brain-derived growth factor (BDNF) (Peprotech, Rocky Hill, NJ, USA, #450-02B) in serum-depleted EMEM/F12 media supplemented with 1% pen/strep (Alquezar et al., 2020; Encinas et al., 2000).

Antibodies & reagents

Immunofluorescence. AlexaFluor 647 mouse-anti-hLAMP1 (1:500, Biolegend, Carlsbad, CA, USA; #328611), AlexaFluor 647 mouse-anti-hLAMP2 (1:500, Biolegend, Carlsbad, CA, USA; #354311), mouse-anti-EEA1 (1:1000, BD Biosciences; Franklin Lakes, NJ, USA; #610457), AlexaFluor 647 goat anti-mouse (1:500, Life Technologies; #A21206). *Western blot.* hLAMP1 (1:1000, DSHB, University of Iowa, USA, #2296838). *Reagents.* LysoTracker Deep Red (Life Technologies; #L12492), MitoTracker Deep Red FM (Invitrogen; Carlsbad, CA, USA, #M22426), Monensin solution 1000X (Invitrogen; #501129057), Nigericin solution (Sigma Aldrich, USA, #SML1779), paraformaldehyde (PFA) solution (Fisher Scientific; #50980494),

glycine (Sigma; #G7126), bovine serum albumin (BSA) (Fisher Scientific; #BP1605100), D-PBS (Sigma; #D8662), Saponin (Sigma; #S7900).

Western blotting

Lysates from FIRE-pHLy-expressing HEK293FT cells were collected from 1X RIPA buffer (Fisher Scientific, #89900) supplemented with a cocktail of phosphatase and protease inhibitors (Roche, Basel, Switzerland, #4693116001) and 1 ug/mL peps

tatin A (Thermo Scientific, #78436). Sample protein concentrations were determined using the Pierce BCA Protein Assay kit (Thermo Scientific, #PI23225). Samples were loaded onto a Novex NuPAGE SDS-PAGE gel system with MOPS running buffer (Life Technologies, #NP001). Proteins were transferred onto nitrocellulose membranes and blotted with indicated antibodies. Imaging of band intensities were performed on a LI-COR Odyssey Infrared System (LI-COR Biosciences, Lincoln, NE, USA).

Live imaging, Immunofluorescence microscopy and colocalization analysis

FIRE-pHLy-expressing HEK293FT cells were plated in TC-grade chamber slides (μ-Slide 8-well chamber slide, Ibidi, Gräfelfing, Germany, #50305795) at a density of 30,000 cells per well for 24 hours. For live uptake of organelle markers, cells were incubated with 30 nM LysoTracker Deep Red or 30 nM MitoTracker Deep Red FM along with 1:1000 Hoechst dye (10mg/mL Hoescht 33342 solution, ThermoFisher, #H3570) in culture medium at 37°C/5% CO_2 for 10 min. For live microscopy, FIRE-pHLy-expressing HEK293FT stable cells were grown on μ-Slide 8-well chamber slide (Ibidi, Gräfelfing, Germany, #50305795) with culture medium supplemented with 10mM HEPES. Time-lapse imaging was performed at 37°C using a spinning-disk microscope, NikonTi (Inverted), UCSF Facility through a Plan Apo VC 100x/1.4 Oil objective

lens. The apparatus is composed of a Andor Borealis CSU-W1 spinning disk confocal, Andor 4-line laser launch (100 mW at 405, 561, and 640 nm; 150 mW at 488 nm), equipped with an Andor Zyla sCMOS camera (5.5 megapixels) for image acquisition, and Micro-Manager 2.0 beta 3 software to control the setup. The images were acquired simultaneously with configuration parameters (100ms exposure) GFP and mCherry channels with 25% laser power. For immunofluorescence staining (LAMP1, LAMP2, and EEA1), cells were washed once with 1X D-PBS (with $MgCl_2$ and $CaCl_2$) and fixed with 2% PFA for 15 min at room temperature (RT). Then, cells were washed once with glycine, blocked for 2 min with 2% BSA/D-PBS, and permeabilized with 0.01% saponin/2% BSA for 1 min at RT. Cells were incubated with primary antibodies for 1 hour at RT, secondary antibodies for 1 hour at RT shielded from light, and washed twice. Cells were imaged using an inverted confocal line-scanning microscope (DMi8 CS Bino, Leica Microsystems Inc., Wetzlar, Germany) with a 63x/1.40 oil-immersion objective lens at 2048x2048 pixel resolution. Fluorescence images was acquired with sequential scanning between frames on the LAS X SP8 Control Software system using preset channel settings (Blue Ex/Em: 405 nm/410-464nm; Green Ex/Em: 470 nm/474-624nm; Red Ex/Em: 587 nm/592-646 nm; Far Red Ex/Em: 653 nm/658-775 nm). Randomly imaged fields were processed (background subtraction, thresholding) and the cytosolic green/red values with Pearson's correlation coefficients were calculated using ImageJ (NIH, Maryland, USA) (Schneider et al., 2012) plugin, JACoP (Just Another Co-localization Plugin) (Bolte & Cordelières, 2006) and linescan analysis performed using ImageJ (NIH, Maryland, USA) (Schneider et al., 2012).

pH calibration buffers, generation of standard curve and pKa calculation

pH calibration buffers and procedures were adapted from a previously described study with few modifications (Wolfe et al., 2013). Buffer recipe is described below, composed of 5 mM NaCl, 115 mM KCl, and 1.3 mM $MgSO_4 \bullet 7H_2O$, 25 mM MES buffer with pH adjusted in the range 2.0 – 7.0. Freshly made buffers were supplemented with 10µM nigericin and 1X monensin.

Stock Conc.	5M NaCl	1M KCl	1M $MgSO_4 \bullet 7H_2O$	0.5M MES	6.7mM Nigericin	Monensin (1000X)	1N KOH/ 1N HCl *	Final volume
Volume	10 µl	1150 µl	13 µl	500 µl	15 µl	10 µl	*	10ml
Final Conc.	5 mM	115 mM	1.3 mM	25 mM	10 µM	1X		(H_2O)

***pH values are adjusted using pH meter with appropriate acid/base. (conc., concentration)**

On day 1, FIRE-pHLy-expressing HEK293FT cells were seeded at a density of 10,000 cells/well resuspended in 100 µl media in collagen type-1 coated, black-bottom 96-well plates (µClear, Greiner Bio-One; #655956). Plates were left in the culture hood at room temperature for 45 min to allow for even cell distribution before incubating at 37°C/5.0% CO_2 overnight. On day 2, cell nuclei were stained with 1:1000 (vol/well) Hoechst dye (10 mg/mL Hoescht 33342 solution, ThermoFisher, #H3570) diluted in cell culture media for 20 min at 37°C/5.0% CO_2. After one wash with 50 µl of 1X D-PBS, 50 µl of each pH titration buffer supplemented with 10 µM nigericin and 1X monensin were added to wells and incubated at 37°C/5.0% CO_2 for 10 min. Note: to attain uniform exposure to pH buffers including ionophores, samples should be (i) imaged within 10-15 min after buffer addition (Canton & Grinstein, 2017; Grillo-Hill et al.,

2014; Lin et al., 2003; Wolfe et al., 2013), (ii) fixed after 10-15 min, or (iii) manually imaged one at a time. Plates were then immediately imaged (total imaging time > 5 min) live on the IN Cell Analyzer 6500 HS (General Electric Life Sciences/Cytiva, Marlborough, MA, USA) and processed (see *High-content confocal microscopy, feature extraction and ratiometric image analysis)*. Liquid dispensing and aspiration were performed using an automatic multichannel pipette (Voyager II, INTEGRA Biosciences Corp, Hudson, NH, USA; #4722). After raw mTFP1 and mCherry intensity values were obtained, log10(mTFP1/mCherry) values were fit with a linear regression. A modified Henderson-Hasselbalch equation, as previously used (Hoffmann & Kosegarten, 1995), was used to calculate pKa.

Lysosomal inhibitor assay in cells

Cells were seeded and cultured on 96-well plates prior to addition of inhibitors - 100 nM bafilomycin A1 (LC Laboratories, Woburn, MA #B-1080), 30 μM chloroquine (Sigma, #C6628), and 0.5 μM concanamycin A (Sigma, #C9705). After 6 hours, cells were fixed with 2% PFA at room temperature (RT) for 15 min and washed once with 1X D-PBS. Cells were stained with 1X Hoechst dye for 20 min at RT protected from light and washed once with 1X D-PBS. Plates were imaged on the IN Cell Analyzer 6500 HS and processed (see *High-content confocal microscopy, feature extraction and ratiometric image analysis)*.

High-content confocal microscopy, feature extraction and ratiometric image analysis

Black 96-well assay plates (μClear bottom, Greiner Bio-One; #655956) were imaged using a fully automated laser-scanning confocal cell imaging system (IN Cell Analyzer 6500HS, GE Life Sciences) with a NIKON 20X/0.75, Plan Apo, CFI/60 objective lens and preset excitation lasers (Blue 405 nm; Green: 488 nm; Red: 561 nm) with simultaneous acquisition setting. Laser

and software autofocus settings were applied to determine a single optimal focus position. The EDGE confocal setting was used to increase image resolution and improve downstream visualization and segmentation of lysosomes. Nine images were acquired per well and were distributed in a 3X3 equidistant grid positioned in the well center. Wells were imaged sequentially in a vertical orientation. Image stack files were analyzed on a high-content image analysis software (IN Cell Developer Toolbox v1.9, GE Life Sciences). Target set segmentation and quantification measures were developed for individual channels and applied onto all sample images. Cell nuclei were segmented using a preset nucleus type segmentation module. The size of nuclear mask was adjusted according to the cell type. Visual inspection of several reference fields across multiple wells confirmed segmentation accuracy. Total number of segmented nuclei was quantified per well. To quantify FIRE-pHLy fluorescence, mCherry was used as the reference channel for segmenting lysosomes. mCherry fluorescence provided a robust representation of FIRE-pHLy localization for the purposes of delineating lysosomal objects, compared to mTFP1 fluorescence, whose signal varies with lysosomal pH. A preset vesicle segmentation module was applied on the 561nm source images with acceptance criteria (Dens-levels>300), min/max granule size (1-10um), scales = 2, sensitivity = 33, low background, and no shape constraints settings. These settings created an object “mask” for lysosomes, which was directly applied to 488nm source images to segment mTFP1 identically as mCherry. Mean fluorescence intensities of mCherry and mTFP1 channels were generated and the ratios calculated. All measures were outputted as a Microsoft Excel file for further analysis.

Data presentation, statistical analysis, and illustrations

All data were generated from randomly selected sample populations from at least three independent experiments represented unless otherwise mentioned in corresponding figure legends. Statistical data were either presented in box–and-whisker plots with median, interquartile range, and maximum & minimum values or bar graphs with mean ± S.E.M. Multiple comparisons between groups were analyzed by one-way ANOVA with Tukey's test and statistical significance for two sets of data was determined by two-tailed, unpaired Student's t-test. All data plots and statistical analyses were performed using GraphPad Prism 8 with no samples excluded. Significant differences between experimental groups were indicated as *P<0.05; **P<0.01; ***P<0.001; Only P <0.05 was considered as statistically significant. NS = not significant. Pre-processing of data was organized in Microsoft Excel. Cartoon schematics were created on Biorender.com. Figures were assembled on Adobe Illustrator.

DATA AND REAGENT AVAILABLE

The authors declare that all relevant data supporting the findings of this study are available within the paper. Any data or reagents can be obtained from the corresponding authors (A.W.K. and M.R.A.) on reasonable request.

ACKNOWLEDGEMENTS

We thank the Mark Von Zastrov lab (UCSF) for providing us with the hLAMP1-GFP plasmid. We also acknowledge the UCSF Small Molecule Discovery Center for their tremendous support and advice on our high-content imaging and analysis protocols. Additionally, we thank members of the Kao and Arkin labs for their thoughtful discussions. This work has received support from the NIH/NIA (R01 AG058447).

AUTHOR CONTRIBUTIONS

M.Y.C., A.R.P., M.G, M.R.A. and A.W.K for conceptualization and design; M.Y.C., A.R.P., K.A., A.L.W., C.A. and M.W. for experimental design and data acquisition; P.T.N. and A.V.M for conceptualization, design and data acquisition of primary rat neuron experiments; all authors analyzed and interpreted data; M.Y.C., A.R.P., M.R.A. and A.W.K. wrote the manuscript; all authors edited the manuscript.

COMPETING INTERESTS STATEMENT

The authors declare no competing financial interests.

REFERENCES

1. Ai, H., Henderson, J. N., Remington, S. J., & Campbell, R. E. (2006). Directed evolution of a monomeric, bright and photostable version of Clavularia cyan fluorescent protein: Structural characterization and applications in fluorescence imaging. *Biochemical Journal*, *400*(Pt 3), 531–540. https://doi.org/10.1042/BJ20060874
2. Alquezar, C., Felix, J. B., McCandlish, E., Buckley, B. T., Caparros-Lefebvre, D., Karch, C. M., Golbe, L. I., & Kao, A. W. (2020). Heavy metals contaminating the environment of a progressive supranuclear palsy cluster induce tau accumulation and cell death in cultured neurons. *Scientific Reports*, *10*. https://doi.org/10.1038/s41598-019-56930-w
3. Anderson, M., Moshnikova, A., Engelman, D. M., Reshetnyak, Y. K., & Andreev, O. A. (2016). Probe for the measurement of cell surface pH in vivo and ex vivo. *Proceedings of the National Academy of Sciences*, *113*(29), 8177–8181. https://doi.org/10.1073/pnas.1608247113
4. Appelqvist, H., Wäster, P., Kågedal, K., & Öllinger, K. (2013). The lysosome: From waste bag to potential therapeutic target. *Journal of Molecular Cell Biology*, *5*(4), 214–226. https://doi.org/10.1093/jmcb/mjt022
5. Arosio, D., Ricci, F., Marchetti, L., Gualdani, R., Albertazzi, L., & Beltram, F. (2010). Simultaneous intracellular chloride and pH measurements using a GFP-based sensor. *Nature Methods*, *7*(7), 516–518. https://doi.org/10.1038/nmeth.1471
6. Ashby, M. C., Ibaraki, K., & Henley, J. M. (2004). It's green outside: Tracking cell surface proteins with pH-sensitive GFP. *Trends in Neurosciences*, *27*(5), 257–261. https://doi.org/10.1016/j.tins.2004.03.010

7. Ballabio, A., & Bonifacino, J. S. (2020). Lysosomes as dynamic regulators of cell and organismal homeostasis. *Nature Reviews Molecular Cell Biology*, *21*(2), 101–118. https://doi.org/10.1038/s41580-019-0185-4

8. Baxi, K., Ghavidel, A., Waddell, B., Harkness, T. A., & Carvalho, C. E. de. (2017). Regulation of Lysosomal Function by the DAF-16 Forkhead Transcription Factor Couples Reproduction to Aging in Caenorhabditis elegans. *Genetics*, *207*(1), 83–101. https://doi.org/10.1534/genetics.117.204222

9. Beyenbach, K. W., & Wieczorek, H. (2006). The V-type H+ ATPase: Molecular structure and function, physiological roles and regulation. *Journal of Experimental Biology*, *209*(4), 577–589. https://doi.org/10.1242/jeb.02014

10. Bischof, H., Rehberg, M., Stryeck, S., Artinger, K., Eroglu, E., Waldeck-Weiermair, M., Gottschalk, B., Rost, R., Deak, A. T., Niedrist, T., Vujic, N., Lindermuth, H., Prassl, R., Pelzmann, B., Groschner, K., Kratky, D., Eller, K., Rosenkranz, A. R., Madl, T., … Malli, R. (2017). Novel genetically encoded fluorescent probes enable real-time detection of potassium in vitro and in vivo. *Nature Communications*, *8*(1), 1422. https://doi.org/10.1038/s41467-017-01615-z

11. Bolte, S., & Cordelières, F. P. (2006). A guided tour into subcellular colocalization analysis in light microscopy. *Journal of Microscopy*, *224*(3), 213–232. https://doi.org/10.1111/j.1365-2818.2006.01706.x

12. Bourdenx, M., Daniel, J., Genin, E., Soria, F. N., Blanchard-Desce, M., Bezard, E., & Dehay, B. (2016). Nanoparticles restore lysosomal acidification defects: Implications for Parkinson and other lysosomal-related diseases. *Autophagy*, *12*(3), 472–483. https://doi.org/10.1080/15548627.2015.1136769

13. Braulke, T., & Bonifacino, J. S. (2009). Sorting of lysosomal proteins. *Biochimica Et Biophysica Acta*, *1793*(4), 605–614. https://doi.org/10.1016/j.bbamcr.2008.10.016

14. Brooks, A. R., Harkins, R. N., Wang, P., Qian, H. S., Liu, P., & Rubanyi, G. M. (2004). Transcriptional silencing is associated with extensive methylation of the CMV promoter following adenoviral gene delivery to muscle. *The Journal of Gene Medicine*, *6*(4), 395–404. https://doi.org/10.1002/jgm.516

15. Burgstaller, S., Bischof, H., Gensch, T., Stryeck, S., Gottschalk, B., Ramadani-Muja, J., Eroglu, E., Rost, R., Balfanz, S., Baumann, A., Waldeck-Weiermair, M., Hay, J. C., Madl, T., Graier, W. F., & Malli, R. (2019). PH-Lemon, a Fluorescent Protein-Based pH Reporter for Acidic Compartments. *ACS Sensors*, *4*(4), 883–891. https://doi.org/10.1021/acssensors.8b01599

16. Canton, J., & Grinstein, S. (2017). Measuring Phagosomal pH by Fluorescence Microscopy. In R. Botelho (Ed.), *Phagocytosis and Phagosomes: Methods and Protocols* (pp. 185–199). Springer. https://doi.org/10.1007/978-1-4939-6581-6_12

17. Casey, J. R., Grinstein, S., & Orlowski, J. (2010). Sensors and regulators of intracellular pH. *Nature Reviews Molecular Cell Biology*, *11*(1), 50–61. https://doi.org/10.1038/nrm2820

18. Chazotte, B. (2011). Labeling Lysosomes in Live Cells with LysoTracker. *Cold Spring Harbor Protocols*, *2011*(2), pdb.prot5571. https://doi.org/10.1101/pdb.prot5571

19. Chen, X., Zaro, J., & Shen, W.-C. (2013). Fusion Protein Linkers: Property, Design and Functionality. *Advanced Drug Delivery Reviews*, *65*(10), 1357–1369. https://doi.org/10.1016/j.addr.2012.09.039

20. Chin, M. Y., Patwardhan, A. R., Ang, K.-H., Wang, A. L., Alquezar, C., Welch, M., Nguyen, P. T., Grabe, M., Molofsky, A. V., Arkin, M. R., & Kao, A. W. (2021a). A genetically encoded, pH-sensitive mTFP1 biosensor for probing lysosomal pH. *BioRxiv*, 2020.11.04.368654. https://doi.org/10.1101/2020.11.04.368654

21. Cho, J.-H., Swanson, C. J., Chen, J., Li, A., Lippert, L. G., Boye, S. E., Rose, K., Sivaramakrishnan, S., Chuong, C.-M., & Chow, R. H. (2017). The GCaMP-R Family of Genetically Encoded Ratiometric Calcium Indicators. *ACS Chemical Biology*, *12*(4), 1066–1074. https://doi.org/10.1021/acschembio.6b00883

22. Choi, C.-H., Webb, B. A., Chimenti, M. S., Jacobson, M. P., & Barber, D. L. (2013). PH sensing by FAK-His58 regulates focal adhesion remodeling. *The Journal of Cell Biology*, *202*(6), 849–859. https://doi.org/10.1083/jcb.201302131

23. Coffey, E. E., Beckel, J. M., Laties, A. M., & Mitchell, C. H. (2014). Lysosomal alkalization and dysfunction in human fibroblasts with the Alzheimer's disease-linked presenilin 1 A246E mutation can be reversed with cAMP. *Neuroscience*, *263*, 111–124. https://doi.org/10.1016/j.neuroscience.2014.01.001

24. Cranfill, P. J., Sell, B. R., Baird, M. A., Allen, J. R., Lavagnino, Z., de Gruiter, H. M., Kremers, G.-J., Davidson, M. W., Ustione, A., & Piston, D. W. (2016). Quantitative Assessment of Fluorescent Proteins. *Nature Methods*, *13*(7), 557–562. https://doi.org/10.1038/nmeth.3891

25. de Duve, C., & Wattiaux, R. (1966). Functions of Lysosomes. *Annual Review of Physiology*, *28*(1), 435–492. https://doi.org/10.1146/annurev.ph.28.030166.002251

26. Deus, C. M., Yambire, K. F., Oliveira, P. J., & Raimundo, N. (2020). Mitochondria–Lysosome Crosstalk: From Physiology to Neurodegeneration. *Trends in Molecular Medicine*, *26*(1), 71–88. https://doi.org/10.1016/j.molmed.2019.10.009

27. Dröse, S., & Altendorf, K. (1996). *BAFILOMYCINS AND CONCANAMYCINS AS INHIBITORS OF V-ATPases AND*. 8.

28. Encinas, M., Iglesias, M., Liu, Y., Wang, H., Muhaisen, A., Ceña, V., Gallego, C., & Comella, J. X. (2000). Sequential Treatment of SH-SY5Y Cells with Retinoic Acid and Brain-Derived Neurotrophic Factor Gives Rise to Fully Differentiated, Neurotrophic Factor-Dependent, Human Neuron-Like Cells. *Journal of Neurochemistry*, *75*(3), 991–1003. https://doi.org/10.1046/j.1471-4159.2000.0750991.x

29. Eskelinen, E.-L. (2006). Roles of LAMP-1 and LAMP-2 in lysosome biogenesis and autophagy. *Molecular Aspects of Medicine*, *27*(5), 495–502. https://doi.org/10.1016/j.mam.2006.08.005

30. Fang, B., Wang, D., Huang, M., Yu, G., & Li, H. (2010). Hypothesis on the Relationship Between the Change in Intracellular pH and Incidence of Sporadic Alzheimer's Disease or Vascular Dementia. *International Journal of Neuroscience*, *120*(9), 591–595. https://doi.org/10.3109/00207454.2010.505353

31. Gallagher, F. A., Kettunen, M. I., Day, S. E., Hu, D.-E., Ardenkjær-Larsen, J. H., Zandt, R. in 't, Jensen, P. R., Karlsson, M., Golman, K., Lerche, M. H., & Brindle, K. M. (2008). Magnetic resonance imaging of pH in vivo using hyperpolarized 13C-labelled bicarbonate. *Nature*, *453*(7197), 940–943. https://doi.org/10.1038/nature07017

32. Grillo-Hill, B. K., Webb, B. A., & Barber, D. L. (2014). Ratiometric Imaging of pH Probes. In *Methods in Cell Biology* (Vol. 123, pp. 429–448). Elsevier. https://doi.org/10.1016/B978-0-12-420138-5.00023-9

33. Han, J., & Burgess, K. (2010). Fluorescent Indicators for Intracellular pH. *Chemical Reviews*, *110*(5), 2709–2728. https://doi.org/10.1021/cr900249z

34. Harned, R. L., Hidy, P. H., Corum, C. J., & Jones, K. L. (1951). Nigericin a new crystalline antibiotic from an unidentified Streptomyces. *Antibiotics & Chemotherapy (Northfield, Ill.)*, *1*(9), 594–596.

35. Hoffmann, B., & Kosegarten, H. (1995). FITC-dextran for measuring apoplast pH and apoplastic pH gradients between various cell types in sunflower leaves. *Physiologia Plantarum*, *95*(3), 327–335. https://doi.org/10.1111/j.1399-3054.1995.tb00846.x

36. Hughes, A. L., & Gottschling, D. E. (2012). An early age increase in vacuolar pH limits mitochondrial function and lifespan in yeast. *Nature*, *492*(7428), 261–265. https://doi.org/10.1038/nature11654

37. Huynh, K., Eskelinen El, Cc, S., A, M., P, S., & S, G. (2007). LAMP proteins are required for fusion of lysosomes with phagosomes. *The EMBO Journal*, *26*(2), 313–324. https://doi.org/10.1038/sj.emboj.7601511

38. Inoue, H., Noumi, T., Nagata, M., Murakami, H., & Kanazawa, H. (1999). Targeted disruption of the gene encoding the proteolipid subunit of mouse vacuolar H+-ATPase leads to early embryonic lethality. *Biochimica et Biophysica Acta (BBA) - Bioenergetics*, *1413*(3), 130–138. https://doi.org/10.1016/S0005-2728(99)00096-1

39. Ishida, Y., Nayak, S., Mindell, J. A., & Grabe, M. (2013). A model of lysosomal pH regulation. *The Journal of General Physiology*, *141*(6), 705–720. https://doi.org/10.1085/jgp.201210930

40. Jin, T., Sasaki, A., Kinjo, M., & Miyazaki, J. (2010). A quantum dot-based ratiometric pH sensor. *Chemical Communications*, *46*(14), 2408–2410. https://doi.org/10.1039/B921602B

41. Jovic, M., Sharma, M., Rahajeng, J., & Caplan, S. (2010). The early endosome: A busy sorting station for proteins at the crossroads. *Histology and Histopathology*, *25*(1), 99–112.

42. Kallunki, T., Olsen, O. D., & Jäättelä, M. (2013). Cancer-associated lysosomal changes: Friends or foes? *Oncogene*, *32*(16), 1995–2004. https://doi.org/10.1038/onc.2012.292

43. Karch, C. M., Kao, A. W., Karydas, A., Onanuga, K., Martinez, R., Argouarch, A., Wang, C., Huang, C., Sohn, P. D., Bowles, K. R., Spina, S., Silva, M. C., Marsh, J. A., Hsu, S., Pugh, D. A., Ghoshal, N., Norton, J., Huang, Y., Lee, S. E., … Tau Consortium Stem Cell Group. (2019). A Comprehensive Resource for Induced Pluripotent Stem Cells from Patients with Primary Tauopathies. *Stem Cell Reports*, *13*(5), 939–955. https://doi.org/10.1016/j.stemcr.2019.09.006

44. Katayama, H., Kogure, T., Mizushima, N., Yoshimori, T., & Miyawaki, A. (2011). A sensitive and quantitative technique for detecting autophagic events based on lysosomal delivery. *Chemistry & Biology*, *18*(8), 1042–1052. https://doi.org/10.1016/j.chembiol.2011.05.013

45. Kimura, S., Noda, T., & Yoshimori, T. (2007). Dissection of the autophagosome maturation process by a novel reporter protein, tandem fluorescent-tagged LC3. *Autophagy*, *3*(5), 452–460. https://doi.org/10.4161/auto.4451

46. Lahuerta, M., Aguado, C., Sánchez-Martín, P., Sanz, P., & Knecht, E. (2018). Degradation of altered mitochondria by autophagy is impaired in Lafora disease. *The FEBS Journal*, *285*(11), 2071–2090. https://doi.org/10.1111/febs.14468

47. Lambert, T. J. (2019). FPbase: A community-editable fluorescent protein database. *Nature Methods*, *16*(4), 277–278. https://doi.org/10.1038/s41592-019-0352-8

48. Lawrence, R. E., & Zoncu, R. (2019). The lysosome as a cellular centre for signalling, metabolism and quality control. *Nature Cell Biology*, *21*(2), 133–142. https://doi.org/10.1038/s41556-018-0244-7

49. Lee, J.-H., McBrayer, M. K., Wolfe, D. M., Haslett, L. J., Kumar, A., Sato, Y., Lie, P. P. Y., Mohan, P., Coffey, E. E., Kompella, U., Mitchell, C. H., Lloyd-Evans, E., & Nixon, R. A. (2015). Presenilin 1 Maintains Lysosomal Ca2+ Homeostasis via TRPML1 by Regulating vATPase-Mediated Lysosome Acidification. *Cell Reports*, *12*(9), 1430–1444. https://doi.org/10.1016/j.celrep.2015.07.050

50. Li, M., Khambu, B., Zhang, H., Kang, J.-H., Chen, X., Chen, D., Vollmer, L., Liu, P.-Q., Vogt, A., & Yin, X.-M. (2013). Suppression of Lysosome Function Induces Autophagy via a Feedback Down-regulation of MTOR Complex 1 (MTORC1) Activity. *The Journal of Biological Chemistry*, *288*(50), 35769–35780. https://doi.org/10.1074/jbc.M113.511212

51. Lin, H.-J., Herman, P., & Lakowicz, J. R. (2003). Fluorescence Lifetime-Resolved pH Imaging of Living Cells. *Cytometry. Part A : The Journal of the International Society for Analytical Cytology*, *52*(2), 77–89. https://doi.org/10.1002/cyto.a.10028

52. Lindenburg, L. H., Vinkenborg, J. L., Oortwijn, J., Aper, S. J. A., & Merkx, M. (2013). MagFRET: The first genetically encoded fluorescent Mg2+ sensor. *PloS One*, *8*(12), e82009. https://doi.org/10.1371/journal.pone.0082009

53. Liu, B., Palmfeldt, J., Lin, L., Colaço, A., Clemmensen, K. K. B., Huang, J., Xu, F., Liu, X., Maeda, K., Luo, Y., & Jäättelä, M. (2018). STAT3 associates with vacuolar H + -ATPase and regulates cytosolic and lysosomal pH. *Cell Research*, *28*(10), 996–1012. https://doi.org/10.1038/s41422-018-0080-0

54. Ma, L., Ouyang, Q., Werthmann, G. C., Thompson, H. M., & Morrow, E. M. (2017). Live-cell Microscopy and Fluorescence-based Measurement of Luminal pH in Intracellular Organelles. *Frontiers in Cell and Developmental Biology*, *5*, 71. https://doi.org/10.3389/fcell.2017.00071

55. Malik, B. R., Maddison, D. C., Smith, G. A., & Peters, O. M. (2019). Autophagic and endo-lysosomal dysfunction in neurodegenerative disease. *Molecular Brain*, *12*(1), 100. https://doi.org/10.1186/s13041-019-0504-x

56. Mauthe, M., Orhon, I., Rocchi, C., Zhou, X., Luhr, M., Hijlkema, K.-J., Coppes, R. P., Engedal, N., Mari, M., & Reggiori, F. (2018). Chloroquine inhibits autophagic flux by decreasing autophagosome-lysosome fusion. *Autophagy*, *14*(8), 1435–1455. https://doi.org/10.1080/15548627.2018.1474314

57. Meilinger, D., Fellinger, K., Bultmann, S., Rothbauer, U., Bonapace, I. M., Klinkert, W. E. F., Spada, F., & Leonhardt, H. (2009). Np95 interacts with de novo DNA

methyltransferases, Dnmt3a and Dnmt3b, and mediates epigenetic silencing of the viral CMV promoter in embryonic stem cells. *EMBO Reports*, *10*(11), 1259–1264. https://doi.org/10.1038/embor.2009.201

58. Miesenböck, G., De Angelis, D. A., & Rothman, J. E. (1998). Visualizing secretion and synaptic transmission with pH-sensitive green fluorescent proteins. *Nature*, *394*(6689), 192–195. https://doi.org/10.1038/28190

59. Mindell, J. A. (2012). Lysosomal Acidification Mechanisms. *Annual Review of Physiology*, *74*(1), 69–86. https://doi.org/10.1146/annurev-physiol-012110-142317

60. Miyawaki, A., Llopis, J., Heim, R., McCaffery, J. M., Adams, J. A., Ikura, M., & Tsien, R. Y. (1997). Fluorescent indicators for Ca2+ based on green fluorescent proteins and calmodulin. *Nature*, *388*(6645), 882–887. https://doi.org/10.1038/42264

61. Mony, V. K., Benjamin, S., & O'Rourke, E. J. (2016). A lysosome-centered view of nutrient homeostasis. *Autophagy*, *12*(4), 619–631. https://doi.org/10.1080/15548627.2016.1147671

62. Mu, F.-T., Callaghan, J. M., Steele-Mortimer, O., Stenmark, H., Parton, R. G., Campbell, P. L., McCluskey, J., Yeo, J.-P., Tock, E. P. C., & Toh, B.-H. (1995). EEA1, an Early Endosome-Associated Protein. EEA1 is a conserved α-helical peripheral membrane protein flanked by cysteine "fingers" and contains a calmodulin-binding IQ motif. *Journal of Biological Chemistry*, *270*(22), 13503–13511. https://doi.org/10.1074/jbc.270.22.13503

63. O'Connor, N., & Silver, R. B. (2013). Ratio Imaging. In *Methods in Cell Biology* (Vol. 114, pp. 387–406). Elsevier. https://doi.org/10.1016/B978-0-12-407761-4.00016-6

64. Ohkuma, S. (1989). Use of fluorescein isothiocyanate-dextran to measure proton pumping in lysosomes and related organelles. In *Methods in Enzymology* (Vol. 174, pp. 131–154). Elsevier. https://doi.org/10.1016/0076-6879(89)74015-5

65. Pierzyńska-Mach, A., Janowski, P. A., & Dobrucki, J. W. (2014). Evaluation of acridine orange, LysoTracker Red, and quinacrine as fluorescent probes for long-term tracking of acidic vesicles. *Cytometry Part A*, *85*(8), 729–737. https://doi.org/10.1002/cyto.a.22495

66. Platt, F. M., Boland, B., & van der Spoel, A. C. (2012). Lysosomal storage disorders: The cellular impact of lysosomal dysfunction. *The Journal of Cell Biology*, *199*(5), 723–734. https://doi.org/10.1083/jcb.201208152

67. Ponsford, A. H., Ryan, T. A., Raimondi, A., Cocucci, E., Wycislo, S. A., Fröhlich, F., Swan, L. E., & Stagi, M. (2020). Live imaging of intra-lysosome pH in cell lines and primary neuronal culture using a novel genetically encoded biosensor. *Autophagy*, 1–19. https://doi.org/10.1080/15548627.2020.1771858

68. Rodriguez, E. A., Campbell, R. E., Lin, J. Y., Lin, M. Z., Miyawaki, A., Palmer, A. E., Shu, X., Zhang, J., & Tsien, R. Y. (2017). The growing and glowing toolbox of fluorescent and photoactive proteins. *Trends in Biochemical Sciences*, *42*(2), 111–129. https://doi.org/10.1016/j.tibs.2016.09.010

69. Rohrer, J., Schweizer, A., Russell, D., & Kornfeld, S. (1996). The targeting of Lamp1 to lysosomes is dependent on the spacing of its cytoplasmic tail tyrosine sorting motif relative to the membrane. *The Journal of Cell Biology*, *132*(4), 565–576.

70. Rousseau, A., & Bertolotti, A. (2018). Regulation of proteasome assembly and activity in health and disease. *Nature Reviews Molecular Cell Biology*, *19*(11), 697–712. https://doi.org/10.1038/s41580-018-0040-z

71. Rudnick, G. (1987). The Vacuolar ATPase Is Responsible for Acidifying Secretory Organelles. *Annals of the New York Academy of Sciences*, *493*(1 Cellular and), 259–263. https://doi.org/10.1111/j.1749-6632.1987.tb27206.x

72. Saftig, P., & Klumperman, J. (2009). Lysosome biogenesis and lysosomal membrane proteins: Trafficking meets function. *Nature Reviews Molecular Cell Biology*, *10*(9), 623–635. https://doi.org/10.1038/nrm2745

73. Schneider, C. A., Rasband, W. S., & Eliceiri, K. W. (2012). NIH Image to ImageJ: 25 years of Image Analysis. *Nature Methods*, *9*(7), 671–675.

74. Serresi, M., Bizzarri, R., Cardarelli, F., & Beltram, F. (2009). Real-time measurement of endosomal acidification by a novel genetically encoded biosensor. *Analytical and Bioanalytical Chemistry*, *393*(4), 1123–1133. https://doi.org/10.1007/s00216-008-2489-7

75. Settembre, C., Fraldi, A., Medina, D. L., & Ballabio, A. (2013). Signals for the lysosome: A control center for cellular clearance and energy metabolism. *Nature Reviews. Molecular Cell Biology*, *14*(5), 283–296. https://doi.org/10.1038/nrm3565

76. Shaner, N. C., Campbell, R. E., Steinbach, P. A., Giepmans, B. N. G., Palmer, A. E., & Tsien, R. Y. (2004). Improved monomeric red, orange and yellow fluorescent proteins derived from Discosoma sp. Red fluorescent protein. *Nature Biotechnology*, *22*(12), 1567–1572. https://doi.org/10.1038/nbt1037

77. Shemiakina, I. I., Ermakova, G. V., Cranfill, P. J., Baird, M. A., Evans, R. A., Souslova, E. A., Staroverov, D. B., Gorokhovatsky, A. Y., Putintseva, E. V., Gorodnicheva, T. V., Chepurnykh, T. V., Strukova, L., Lukyanov, S., Zaraisky, A. G., Davidson, M. W., Chudakov, D. M., & Shcherbo, D. (2012). A monomeric red fluorescent protein with low cytotoxicity. *Nature Communications*, *3*(1), 1204. https://doi.org/10.1038/ncomms2208

78. Shen, Y., Rosendale, M., Campbell, R. E., & Perrais, D. (2014). PHuji, a pH-sensitive red fluorescent protein for imaging of exo- and endocytosis. *The Journal of Cell Biology*, *207*(3), 419–432. https://doi.org/10.1083/jcb.201404107

79. Shinoda, H., Shannon, M., & Nagai, T. (2018). Fluorescent Proteins for Investigating Biological Events in Acidic Environments. *International Journal of Molecular Sciences*, *19*(6). https://doi.org/10.3390/ijms19061548

80. Sun, Y., Li, M., Zhao, D., Li, X., Yang, C., & Wang, X. (2020). Lysosome activity is modulated by multiple longevity pathways and is important for lifespan extension in C. elegans. *ELife*, *9*, e55745. https://doi.org/10.7554/eLife.55745

81. Tantama, M., Hung, Y. P., & Yellen, G. (2011). Imaging Intracellular pH in Live Cells with a Genetically-Encoded Red Fluorescent Protein Sensor. *Journal of the American Chemical Society*, *133*(26), 10034–10037. https://doi.org/10.1021/ja202902d

82. Tekirdag, K., & Cuervo, A. M. (2018). Chaperone-mediated autophagy and endosomal microautophagy: Jointed by a chaperone. *The Journal of Biological Chemistry*, *293*(15), 5414–5424. https://doi.org/10.1074/jbc.R117.818237

83. Toei, M., Saum, R., & Forgac, M. (2010). Regulation and isoform function of the V-ATPases. *Biochemistry*, *49*(23), 4715–4723. https://doi.org/10.1021/bi100397s

84. Van Acker, Z. P., Bretou, M., & Annaert, W. (2019). Endo-lysosomal dysregulations and late-onset Alzheimer's disease: Impact of genetic risk factors. *Molecular Neurodegeneration*, *14*. https://doi.org/10.1186/s13024-019-0323-7

85. Vinkenborg, J. L., Nicolson, T. J., Bellomo, E. A., Koay, M. S., Rutter, G. A., & Merkx, M. (2009). Genetically encoded FRET sensors to monitor intracellular Zn2+ homeostasis. *Nature Methods*, *6*(10), 737–740. https://doi.org/10.1038/nmeth.1368

86. Wan, Q., Chen, S., Shi, W., Li, L., & Ma, H. (2014). Lysosomal pH rise during heat shock monitored by a lysosome-targeting near-infrared ratiometric fluorescent probe. *Angewandte Chemie (International Ed. in English)*, *53*(41), 10916–10920. https://doi.org/10.1002/anie.201405742

87. Wang, X., Fan, L., Wang, Y., Zhang, C., Liang, W., Shuang, S., & Dong, C. (2020). Visual monitoring of the lysosomal pH changes during autophagy with a red-emission fluorescent probe. *Journal of Materials Chemistry B*, *8*(7), 1466–1471. https://doi.org/10.1039/C9TB02551K

88. Webb, B. A., Aloisio, F. M., Charafeddine, R. A., Cook, J., Wittmann, T., & Barber, D. L. (2020). pHLARE: A New Biosensor Reveals Decreased Lysosome pH in Cancer Cells. *Molecular Biology of the Cell*, mbc.E20-06-0383. https://doi.org/10.1091/mbc.E20-06-0383

89. Webb, B. A., Chimenti, M., Jacobson, M. P., & Barber, D. L. (2011). Dysregulated pH: A perfect storm for cancer progression. *Nature Reviews Cancer*, *11*(9), 671–677. https://doi.org/10.1038/nrc3110

90. Wilson, J. M., de Hoop, M., Zorzi, N., Toh, B.-H., Dotti, C. G., & Parton, R. G. (2000). EEA1, a Tethering Protein of the Early Sorting Endosome, Shows a Polarized Distribution in Hippocampal Neurons, Epithelial Cells, and Fibroblasts. *Molecular Biology of the Cell*, *11*(8), 2657–2671.

91. Wolfe, D. M., Lee, J., Kumar, A., Lee, S., Orenstein, S. J., & Nixon, R. A. (2013). Autophagy failure in Alzheimer's disease and the role of defective lysosomal acidification. *The European Journal of Neuroscience*, *37*(12), 1949–1961. https://doi.org/10.1111/ejn.12169

92. Zhang, X.-X., Wang, Z., Yue, X., Ma, Y., Kiesewetter, D. O., & Chen, X. (2013). pH-Sensitive Fluorescent Dyes: Are They Really pH-Sensitive in Cells? *Molecular Pharmaceutics*, *10*(5), 1910–1917. https://doi.org/10.1021/mp3006903

CHAPTER 3: PHENOTYPIC SCREENING USING HIGH-CONTENT IMAGING TO IDENTIFY LYSOSOMAL PH MODULATORS IN A NEURONAL CELL MODEL

Marcus Y. Chin[1,2], Kean-Hooi Ang[2], Julia Davies[2], Carolina Alquezar[1], Virginia G. Garda[1,2], Brendan Rooney[3], Kun Leng[3,4,5], Martin Kampmann[3], Michelle R. Arkin[2*] and Aimee W. Kao[1*]

[1]Memory and Aging Center, Department of Neurology, University of California, San Francisco, California, CA 94158, USA

[2]Small Molecule Discovery Center, Department of Pharmaceutical Chemistry, University of California, San Francisco, CA 94143, USA

[3]Institute for Neurodegenerative Diseases, Department of Biochemistry and Biophysics, University of California, San Francisco, CA 94158, USA

[4]Biomedical Sciences Graduate Program, University of California, San Francisco, CA 94158, USA

[5]Medical Scientist Training Program, University of California, San Francisco, CA 94158, USA

[*] Corresponding authors: michelle.arkin@ucsf.edu and aimee.kao@ucsf.edu

Key words: lysosomes, lysosomal pH, pH biosensor, high-content analysis, neurons, phenotypic screening

ABSTRACT

Lysosomes are intracellular organelles responsible for the degradation of diverse macromolecules in a cell. A highly acidic pH is required for the optimal functioning of lysosomal enzymes. Loss of lysosomal intralumenal acidity can disrupt cellular protein homeostasis and is linked to age-related diseases such as neurodegeneration. Using a new robust lysosomal pH biosensor (FIRE-pHLy), we have developed a cell-based fluorescence assay for high-throughput screening (HTS) and applied it to differentiated SH-SY5Y neuroblastoma cells. The goal of this study was two-fold: 1) to screen for small molecules that acidify lysosomal pH and 2) to identify molecular targets and pathways that regulate lysosomal pH. We conducted a screen of 1,835 bioactive compounds with annotated target information to identify lysosomal pH modulators (both acidifiers and alkalinizers). Forty-five compounds passed initial hit selection criteria, using a combined analysis approach of population-based and object-based data. Twenty-three compounds were retested in dose response assays and two compounds, OSI-027 and PP242, were identified as top acidifying hits. Overall, data from this phenotypic HTS screen may be used to explore novel regulatory pathways of lysosomal pH regulation. Additionally, OSI-027 and PP242 may serve as useful tool compounds to enable mechanistic studies of autophagy activation and lysosomal acidification as potential therapeutic pathways for neurodegenerative diseases.

INTRODUCTION

Lysosomes are specialized membrane-bound organelles that participate in many crucial cellular functions such as macromolecular degradation, nutrient sensing and secretion (Ballabio & Bonifacino, 2020; Lawrence & Zoncu, 2019; Mony et al., 2016). They are intimately involved in autophagy, which serves as a key pathway for maintaining protein homeostasis within the cell. Lysosomes derive their degradative function by possessing a very acidic lumen (pH~4.5-4.7) (Casey et al., 2010; Ohkuma, 1989), allowing the optimal activation of hydrolytic enzymes that are ultimately responsible for substrate breakdown. The lysosomal pH is tightly regulated through the vacuolar-type H^+-ATPase (V-ATPase) proton pump and other counter-ion channels (Mindell, 2012).

Defective lysosomes are a common feature of age-related and neurodegenerative disorders. Numerous mutations have been found in genes directly involved in the endolysosomal pathway (Koh et al., 2019; Settembre et al., 2013). Pathological accumulation of proteins is also seen across various neurodegenerative diseases (Monaco & Fraldi, 2020; Ross & Poirier, 2004), implicating a role in aberrant cellular clearance. While the exact mechanisms causing neurodegeneration remain elusive, these observations suggest an overall breakdown in protein homeostatis stemming from lysosomal dysfunction. Indeed, lysosomal acidity has been described to be impaired in studies of age-related neurodegenerative disease (Baxi et al., 2017; Colacurcio & Nixon, 2016; Hughes & Gottschling, 2012; Lee et al., 2015; Sun et al., 2020; Tong et al., 2021).

With increasing evidence underscoring its critical role in neurodegenerative disease, correcting lysosomal function and pH regulation may be therapeutically tractable strategies for future drug development. However, relatively few phenotypic screens have been conducted with

a specific focus on lysosomes. High-throughput screening (HTS) studies have explored lysosomal morphology, positioning and calcium regulation, in regard to lysosomal storage disorders and cancer (Chin, Espinosa, et al., 2021). Importantly, to our knowledge, no group has conducted a phenotypic screen on lysosomal pH. Such is the focus in the current study.

Novel lysosomal pH probes that specifically target lysosomes and accurately measure intralumenal pH have been described by various groups (Chin, Espinosa, et al., 2021; Ponsford et al., 2020; Webb et al., 2020). Recently, we engineered FIRE-pHLy, a genetically encoded ratiometric lysosomal pH biosensor with a reported pKa of ~4.4 (Chin, Patwardhan, et al., 2021). FIRE-pHLy presents advantages in automated, high-throughput screening including stable expression in cells, accurate targeting to lysosomal compartments, and resistance to fluorescence quenching during fixation. Here, we utilized FIRE-pHLy to develop a cell-based phenotypic assay for lysosomal pH. FIRE-pHLy fluorescence was collected via high-content imaging and analyzed in a neuronal cell model. The overall goal of this study was two-fold: 1) to identify small molecules that acidify lysosomes and 2) to gain mechanistic insight on the pathways regulating lysosomal pH. Ultimately, modulation of lysosomal acidity may restore protein homeostasis defects and serve as a novel therapeutic strategy for neurodegenerative disease-related drug discovery.

RESULTS AND DISCUSSION

High-content imaging screen to identify modulators of lysosomal pH

To identify small molecules and biological pathways that regulate lysosomal pH, we developed a cell-based high-content imaging screen that measured relative changes in intralumenal pH of lysosomes through fluorescence detection **(Figure 3.1)**. We utilized the previously validated genetically encoded pH biosensor, FIRE-pHLy or Fluorescence Indicator Reporting pH of Lysosomes (Chin, Patwardhan, et al., 2021b). FIRE-pHLy is composed of monomeric teal fluorescent protein 1 (mTFP1), mCherry, and lysosome-associated membrane protein 1 (LAMP1) that targets the fusion protein to lysosomal membranes. The fluorescence of mTFP1 is pH-dependent, while mCherry serves as an expression control and internal lysosome marker. Ratiometric imaging of mTFP1 and mCherry reports relative changes (herein referred to as the FIRE-pHLy ratio or mTFP1/mCherry) in the lysosomal pH environment.

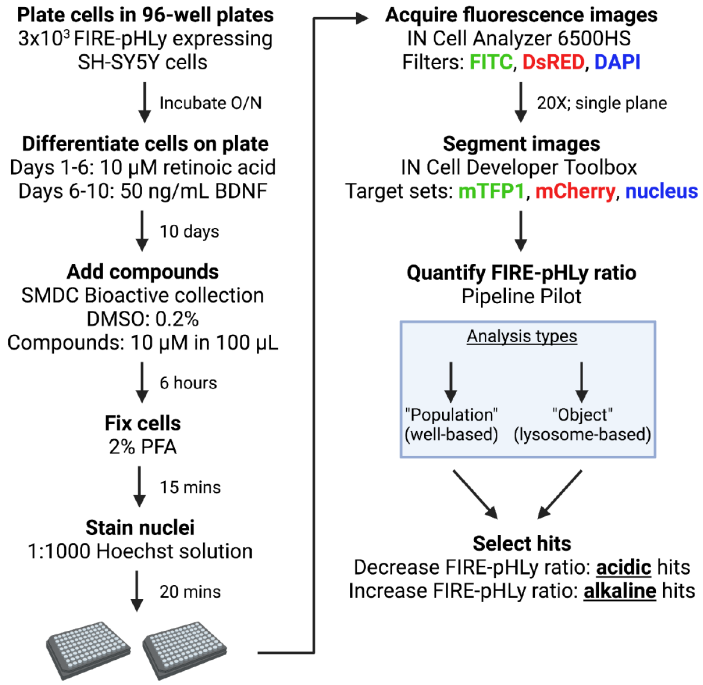

Figure 3.1. HTS flowchart for identifying lysosomal pH modulators.
FIRE-pHLy expressing SH-SY5Y cells were differentiated on 96-well microplates for 10 days and treated with bioactive compounds (10 μM/0.2% DMSO) for their potential ability to decrease (acidify) or increase (alkalinize) lysosomal pH, as measured by change in the FIRE-pHLy ratio. Compound ratios were calculated through ratiometric quantification of mTFP1 and mCherry fluorescence intensities. Data was analyzed in parallel through two distinct pipelines (population-based and object-based quantification) and compared to select hits.

FIRE-pHLy can be stably expressed in a variety of cell models including human neuroblastoma SH-SY5Y cells, which was selected for this HTS study due to their ability to be differentiated into neuron-like cells (Encinas et al., 2000). Because terminally differentiated SH-SY5Y cells have qualities appropriate to model aspects of neurodegenerative diseases, including endogenous expression of the aggregation-prone proteins such as tau (Forster et al., 2016; Xicoy et al., 2017), they may provide enhanced therapeutic relevance over actively dividing cells in drug screening campaigns. Cells were differentiated within 96-well microplates and then treated with a 1,835-member library of bioactive compounds at the UCSF Small Molecule Discovery Center (SMDC). The final screening concentration was 10 μM with a DMSO concentration of 0.2%, which did not artificially alter FIRE-pHLy ratio measurements **(Figure 3.2A)** and was non-toxic to cells **(Figure 3.2B)**. Multi-stack images were acquired and analyzed through a custom segmentation protocol for mTFP1, mCherry and nuclei target sets **(Figure 3.1)** (Chin, Patwardhan, et al., 2021b).

First, we designed a population-based analysis approach that quantified the FIRE-pHLy ratio averaged across the entire well. Screening data variability was measured by the percent coefficient of variation (CV) of the FIRE-pHLy ratio. The CV of 5% in negative controls indicated that the assay was consistent across all assay plates **(Figure 3.2C)**, with a mean FIRE-pHLy ratio of 0.36 ± 0.02. The CV for cell count was also acceptable (CV = 22%) with a mean of 1,163 ± 261 quantified cells per well **(Figure 3.2D)**. Compounds that decreased the FIRE-

pHLy ratio (i.e. decreased pH) were considered acidic hits, while any that increased the FIRE-pHLy ratio (i.e. increased pH) were labeled as alkaline hits.

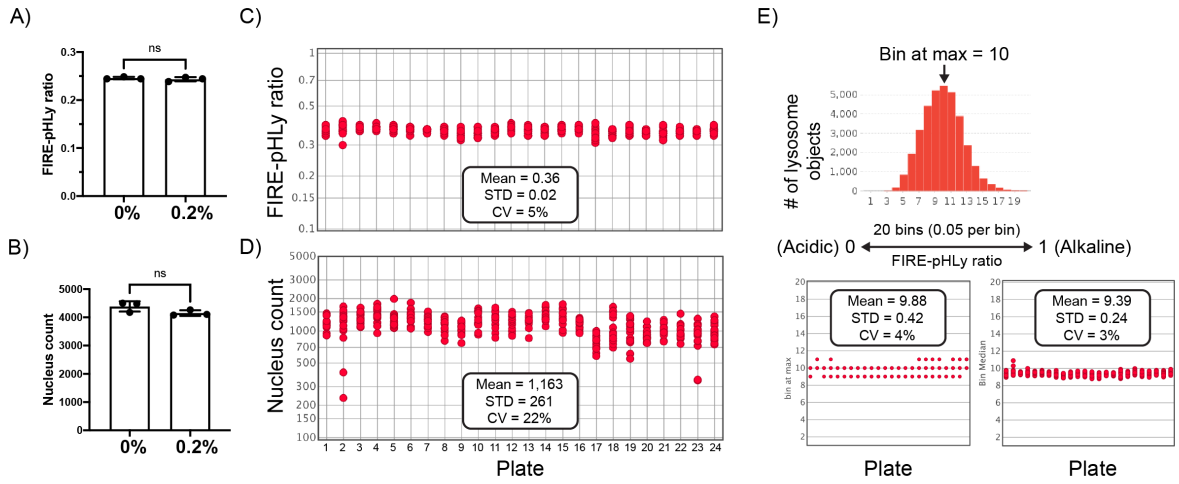

Figure 3.2. Assay performance for negative controls.
(A) FIRE-pHLy ratio (lysosomal pH change) and (B) cell count (measurement for cell toxicity) was unaffected at the screening DMSO concentration of 0.2%. (C-D) Population-based analysis. (C) FIRE-pHLy ratios and (D) nucleus count displayed across 24 assay plates, with combined mean, standard deviation (STD) and percent coefficient of variation (CV) for the entire screen. (E) Lysosomal object-based analysis. (Top) Representative frequency distribution of lysosomal objects and their quantified FIRE-pHLy ratio binned from 0 to 1 (0.05 increment per bin; 20 total bins). (Bottom left) Bin at max and (bottom right) Bin median displayed across 24 assay plates, with combined mean, STD and CV. Each red circle represents 1 negative control well (n = 16 per plate).

As a secondary method for hit selection, we developed an object-based analysis approach in order to focus on lysosomes, optimize sensitivity, and account for different populations of lysosomes based on coordinate location (Bright et al., 2016; Cabukusta & Neefjes, 2018). FIRE-pHLy ratios from individually segmented lysosomes in the DMSO controls were binned according to their ratio values, normalized from 0.0 to 1.0 with an increment of 0.05 per bin, and plotted as a histogram. FIRE-pHLy ratios from compound-treated wells were then normalized to the DMSO bins **(Methods)**. The data were normally distributed in the negative control DMSO-treated wells; assay means of 'bin at max' and 'median bin' were 9.88 ± 0.42 and 9.39 ± 0.24, respectively **(Figure 3.2E)**. Shifts in the distribution caused by modulators of lysosomal pH would result in acidic (leftward curve shift) or alkaline (rightward curve shift) phenotypes; skew in the distribution could indicate that a subset of lysosomes were affected by compound

treatment. The CVs of 'bin at max' and 'median bin' were 4% and 3%, supporting the consistency of our assay. Hits were selected from both population- and object-based approaches in tandem and compared to generate the primary hit list.

Primary hit selection, filtering and comparison of analysis approaches

Thresholding for primary hits was performed using both parallel quantification pipelines, which will herein be referred to as "Population-based analysis" **(Figures 3.3A-C)** and "Object-based analysis" **(Figures 3.3D-H)**. With population-based analysis, controls were visualized along a two-dimensional plot of FIRE-pHLy ratio fold change (FC) and nuclear count ("nucleus") FC to define the boundaries for determining hits **(Figure 3.3A)**. Compounds that exhibited a nucleus FC of less than 0.48 (-3 standard deviations; SD) were considered cytotoxic and excluded. Compounds with FIRE-pHLy ratio FCs within ± 3SD of control were considered inactive **(Figure 3.3B, 3.4A)**. Primary alkaline hits were identified based on FIRE-pHLy ratio FC of at least 1.12 and nucleus FC of at least 0.48 **(Figure 3.4B)**. Conversely, acidic hits were identified based on FIRE-pHLy ratio FC of less than or equal to 0.88 and nucleus FC of at least 0.48 **(Figure 3.3C)**. Importantly, we note that the FIRE-pHLy ratio could be artificially altered by changes in mCherry fluorescence. This may be caused by compound autofluorescence or off-target pH changes in the cytosolic environment where mCherry resides. To exclude these artifacts, a filter of mCherry fluorescence intensity FC was applied. Alkaline compounds with mCherry fluorescence FC > 0.7 and acidic compounds with FC < 1.5 were shortlisted. Overall, the population-based analysis approach identified 29 filtered alkaline hits **(Figure 3.4B)** and 13 filtered acidic hits **(Figure 3.3C)**.

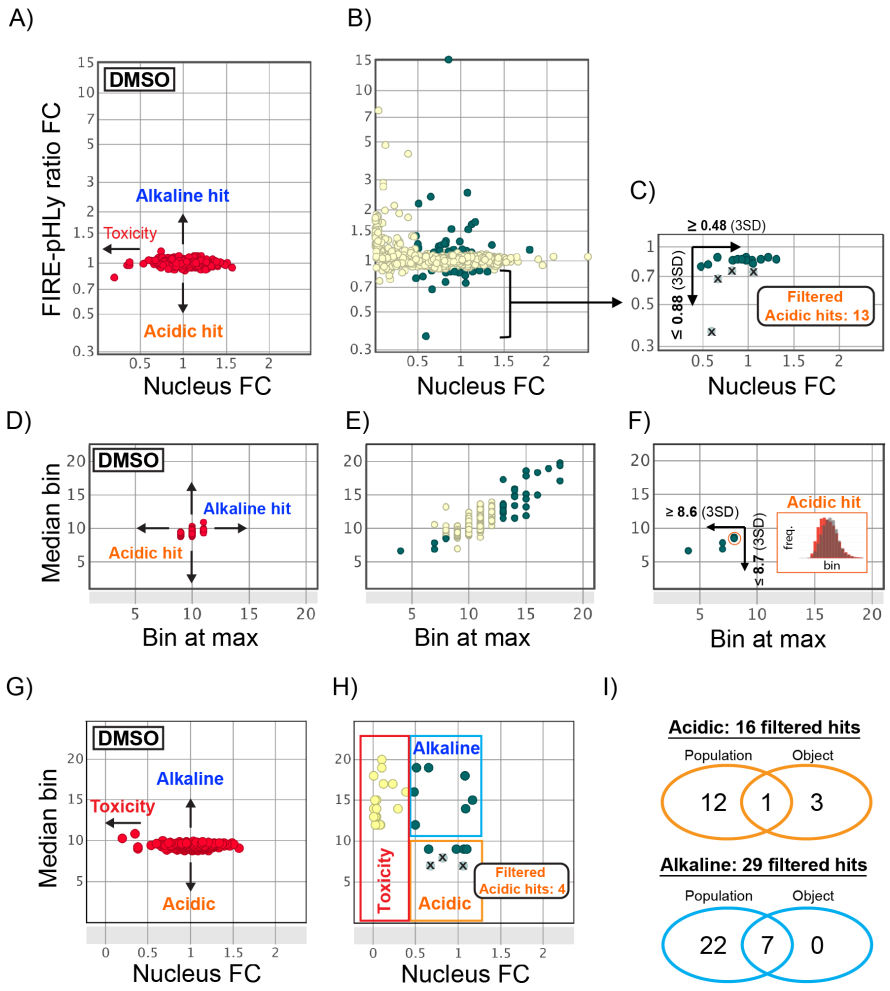

Figure 3.3. Hit selection for lysosomal acidifiers.
(A-C) Population-based analysis. (A) Two-dimensional (2D) plot of FIRE-pHLy ratio fold change (FC) vs. nuclei FC (i.e. cell count) for all DMSO negative controls (shown in red dots; n = 384 wells across all assay plates). (B) 2D FIRE-pHLy ratio FC vs. nuclei FC plot for all test compounds (n = 1 per compound; 1,835 total compounds). Green dots represent primary hit compounds; yellow dots represent toxic or inactive compounds. (C) Expanded inset of acidic hits from Figure 2B. Acidic hits were selected using nucleus FC ≤ 3SD and FIRE-pHLy ratio FC ≤ 3SD compared to controls. Compounds that artificially altered the FIRE-pHLy ratio FC through mCherry fluorescence were excluded (green dots with black cross marks). (D-H) Lysosomal object-based analysis. (D) 2D plot of median bin vs. bin at max for DMSO negative controls (shown in red dots; n = 384 wells across all assay plates). (E) 2D plot of median bin vs. bin at max for all test compounds (shown in yellow dots; n = 1 per compound; 1,835 total compounds). Green dots represent primary hit compounds. (F) Lysosomal object-based acidic hits from Figure 2E. Acidic hits were selected using median bin ≤ 3SD and bin at max ≤ 3SD. (Inset) Frequency distribution for hit compound highlighted with a red circle. Grey bars represent negative control distribution. Red bars represent hit compound distribution. (G) Filtering hits for cell toxicity. 2D plot of median bin vs. nucleus FC for all DMSO negative controls. (H) 2D plot of median bin vs. nucleus FC for test compounds. Compounds highighted in the red box were excluded due to cell toxicity; alkaline hits are highlighted by the blue box; acidic hits are highlighted in the orange box. Compounds that altered mCherry fluorescence were excluded (green dots with black cross marks). (I) Venn diagram showing overlap of final filtered alkaline and acidic hits selected from population-based and lysosomal object-based analyses. Data in this figure was visualized in DataWarrior.

A similar thresholding paradigm was used for object-based analysis. Compared to controls **(Figure 3.3D)**, compounds that increased or decreased median bin and bin at max by 3SD were considered as hits **(Figure 3.3E)**. Alkaline hits were identified based on a bin at max and median of at least 13 and 11.5, respectively, and were selected **(Figure 3.4C)**. Acidic hits were identified based on a bin at max and median of less than or equal to 8.7 and 8.6, respectively **(Figure 3.3F)**. Subsequently, compounds that reduced nucleus FC compared to control **(Figures 3.3G, 3.3H)** were eliminated. Finally, compounds that artificially altered mCherry fluorescence intensity were also removed **(Figure 3.3H)**.

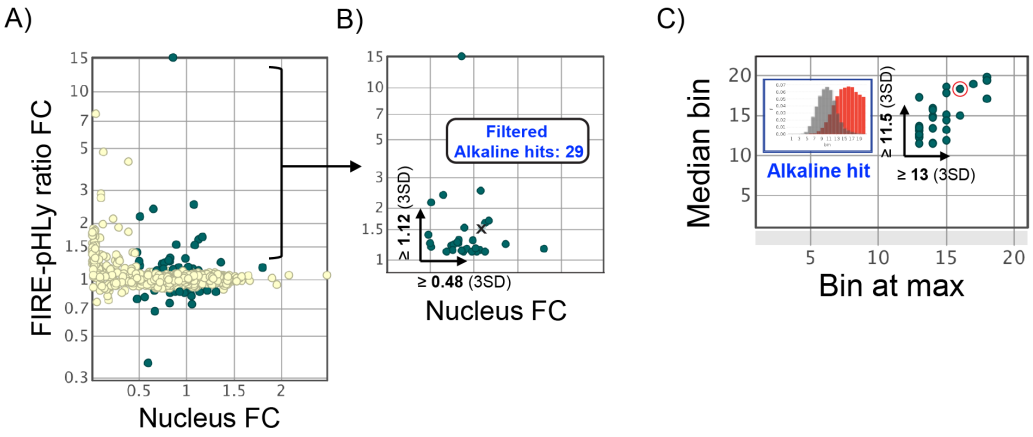

Figure 3.4. Hit selection for lysosomal alkalinizers.
(A-B) Population-based analysis. (A) 2D FIRE-pHLy ratio FC vs. nuclei FC plot for all test compounds (n = 1 per compound; 1,835 total compounds). Green dots represent primary hit compounds; yellow dots represent toxic or inactive compounds. (B) Expanded inset of alkaline hits from Figure S2A. Alkaline hits were selected using nucleus FC ≥ 3SD and FIRE-pHLy ratio FC ≥ 3SD compared to controls. Compounds that artificially altered the FIRE-pHLy ratio FC through mCherry fluorescence were excluded (green dot with black cross marks). (C) Lysosomal object-based analysis. 2D plot of median bin vs. bin at max for primary alkaline hits (shown in green). Thresholded alkaline hits from median bin ≥ 3SD and bin at max ≥ 3SD. Frequency distribution of example hit compounds are highlighted in red circles. Grey bars represent negative control distribution. Orange bars represent an example of an alkaline compound distribution. Data was visualized in DataWarrior software.

Hits were compiled from population-based and object-based analyses to generate the finalized filtered hit list. Thirteen acidic hits were identified from population-based analysis **(Table 3.1)**, while four hits were identified from object-based analysis **(Table 3.2)**. One compound, OSI-027, was found in both analysis pipelines. For alkaline hits, twenty-nine

compounds were identified from population-based methods **(Table 3.3)**, all seven of which overlapped with object-based methods **(Table 3.4)**. No additional alkaline hits were identified by object-based analysis. Overall, the population-based analysis method identified more hits than object-based analysis **(Figure 3.3I)** in both acidic and alkaline hit types. More alkalinizing hits were identified than acidifying hits.

Table 3.1. Primary Filtered Acidifying Compounds Identified from Population-based Analysis

Hit No.	SMDC ID	Compound	Ratio FC	Nuclei FC
1	972531	OSI-027*	0.88	0.98
2	972462	AZ 960	0.79	0.48
3	972875	3,4-Methylenedioxy-β-nitrostyrene	0.81	0.56
4	751824	Erlotinib	0.82	1.05
5	972846	LY2835219	0.85	0.98
6	131834	Nocodazole	0.85	1.04
7	972322	BMS-707035	0.85	0.83
8	972264	ABT-751 (E7010)	0.86	1.14
9	973076	Vinblastine	0.86	0.93
10	972537	Buparlisib	0.86	0.88
11	972406	Teniposide	0.86	1.31
12	972458	NVP-BHG712	0.88	1.22
13	130715	Nifedipine	0.88	0.66

Table 3.2. Primary Filtered Acidifying Compounds Identified from Object-based Analysis

Hit No.	SMDC ID	Compound	Bin Median	Bin Max
1	972531	OSI-027*	8.50	8
2	972562	WAY-600	8.51	8
3	972465	PP242	8.66	8
4	972508	Ibrutinib	8.64	8

*OSI-027 was identified as a hit in both population- and object-based analysis. Compounds highlighted in red passed dose-response restesting in differentiated SH-SH5Y cells.

Table 3.3. Primary alkaline hit list for population-based analysis.

Hit No.	SMDC ID	Compound	Ratio FC	Nuclei FC
1	972581	PHA-665752*	15.2	0.86
2	129934	Reserpine*	2.52	1.08
3	973105	Daptomycin*	2.38	0.65
4	754466	GW5074*	2.16	0.51
5	972356	MC1568*	1.69	1.17
6	735544	Curcumin*	1.4	0.48
7	754395	Ro 31-8220 Mesylate*	1.25	0.5
8	972202	PI-103	1.64	1.13
9	253094	2,6-Dihydroanthra/1,9-Cd/Pyrazol-6-One	1.54	0.89
10	972198	Motesanib Diphosphate	1.31	0.83
11	754441	U0126-EtOH	1.3	0.99
12	972712	Semaxanib	1.27	0.81
13	131804	Physcion	1.25	0.82
14	957604	Tazarotene	1.24	1.36
15	972346	Orantinib	1.23	0.77
16	914975	Lapatinib	1.21	0.74
17	131341	Mitoxantrone	1.19	0.51
18	973128	4-(3-Pyridin-2-Yl-1h-Pyrazol-4-Yl)Quinoline	1.17	1.02
19	734929	(+)-Usniacin	1.16	0.92
20	130795	Dipyridamole	1.16	1.8
21	255714	Clofazimine	1.14	1.07
22	972350	SB525334	1.14	0.76
23	255752	Carbimazole	1.13	1.02
24	972416	Shikimic Acid	1.13	0.86
25	972605	Tubastatin A HCl	1.12	1.03
26	285792	Ipriflavone	1.12	0.88
27	973097	Lomeguatrib	1.12	0.98
28	972275	Danoprevir	1.12	1.13
29	972717	Otilonium Bromide	1.12	0.69

Table 3.4. Primary alkaline hit list for object-based analysis.

Hit No.	SMDC ID	Compound	Bin Median	Bin Max
1	972581	PHA-665752*	37.3	19
2	129934	Reserpine*	18.3	16
3	973105	Daptomycin*	19.4	18
4	754466	GW5074*	18.6	15
5	972356	MC1568*	14.7	14
6	735544	Curcumin*	15.9	14
7	754395	Ro 31-8220 Mesylate*	11.5	14

*Compounds identified as hits in both population- and object-based analysis

Hit confirmation with dose response re-testing

Twenty-three compounds (i.e. all sixteen acidic hits and the seven alkaline hits identified in both population- and object-based analysis) were retested in a two-fold dose response over a range of 80 µM to 0.156 µM in differentiated SH-SY5Y cells. Among the sixteen primary acidic hits, five were reproduced and were re-tested in undifferentiated cells to support broader hit confirmation in differing cellular states. Two compounds, OSI-027 and PP242, reproducibly lowered lysosomal pH in a dose-dependent manner in both undifferentiated and differentiated cells. The EC_{50} values for OSI-027 in differentiated and undifferentiated cells were similar **(Figure 3.5A)**. For PP242, there appears to be a ten-fold EC_{50} decrease post-differentiation **(Figure 3.5B**), though the narrow range for differentiated SH-SY5Y makes it difficult to precisely measure EC_{50}. In the alkaline direction, reserpine robustly increased lysosomal pH, with a ~8.3-fold decrease in EC_{50} post-differentiation **(Figure 3.6)**.

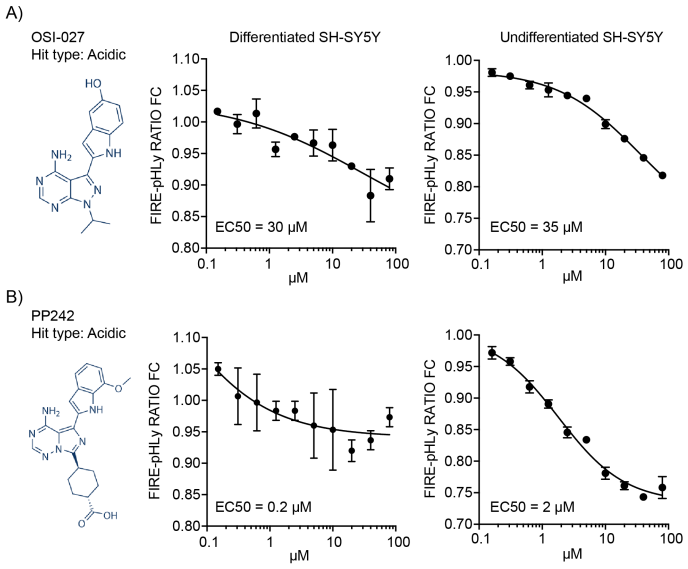

Figure 3.5. Top acidic hits tested in differentiated and undifferentiated SH-SY5Y cells.
Ten-point dose-response curves (2-fold serial dilution) from 0.15 µM to 80 µM. Cells were treated with compounds for 6 hours before imaging. FIRE-pHLy ratios were calculated by dividing total mTFP1 and mCherry fluorescence, displayed as a fold change relative to control, and plotted according to dose. (A) OSI-027 exhibited an EC_{50} of 30 µM and 35 µM in differentiated and undifferentiated SH-SY5Y cells, respectively. (B) PP242 exhibited an EC_{50} of 0.2 µM and 2 µM in differentiated and undifferentiated SH-SY5Y cells, respectively. Data points are presented as mean ± SD, from 3 biological replicates; n = ~3,000-5,000 differentiated or ~15,000-20,000 undifferentiated cells quantified per dose per time point.

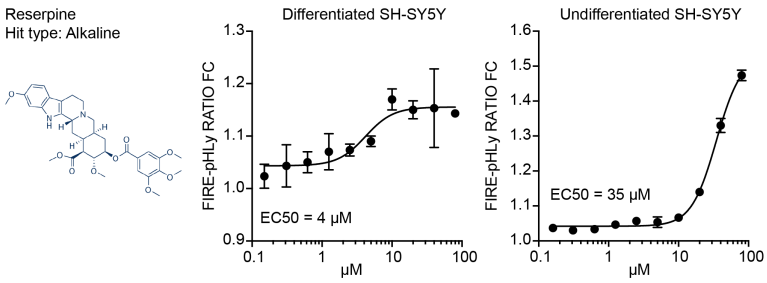

Figure 3.6. Hit confirmation for top bioactive alkaline hit tested in differentiated and undifferentiated SH-SY5Y cells.
Ten-point dose-response curves (2-fold serial dilution) from 80 µM to 0.15 µM. Cells were treated with compounds for 6 hours before imaging. FIRE-pHLy ratios were calculated by dividing total mTFP1 and mCherry fluorescence, displayed as a fold change relative to control, and plotted according to dose. (C) Reserpine exhibited an EC_{50} of 4 µM and 35 µM in differentiated and undifferentiated SH-SY5Y cells, respectively. Data points are presented as mean ± SD, from 3 biological replicates; n = ~3,000-5,000 differentiated or ~15,000-20,000 undifferentiated cells quantified per dose per time point.

Overall, we note the consistent expansion of the ratio FC range across the ten-point dose response in undifferentiated cells compared to their differentiated counterparts. In differentiated cells, the ratio FC range for OSI-027 and PP-242 was ~1.00 to ~0.90 and ~1.05 to ~0.93, respectively. For the undifferentiated cells, the range for OSI-027 and PP242 was ~0.97 to ~0.81 and ~0.97 to ~0.75, respectively. These data suggest that undifferentiated SH-SY5Y cells are more sensitive to pH lowering effects induced by OSI-027 and PP242 than differentiated cells. We elected to proceed with validating the top two acidic hits, OSI-027 and PP242, because of their chemical similarity and potential mechanistic interest in re-acidifying lysosomes. The overall summary of the primary screen is detailed in **Figure 3.7**.

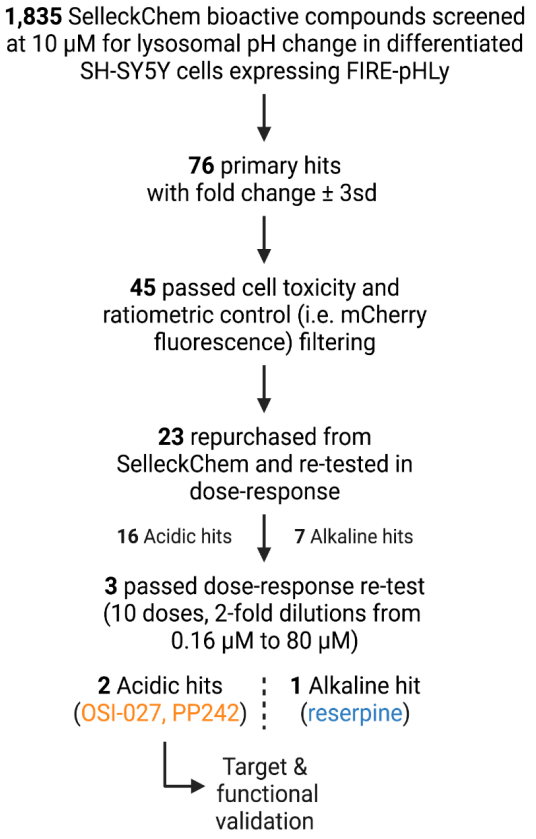

Figure 3.7. Hit selection summary.
Summary of small molecule hits that modulate lysosomal pH in SH-SY5Y cells.

Functional validation of top acidic hits OSI-027 and PP242

To functionally validate acidification of lysosomal pH, we treated live undifferentiated SH-SY5Y cells (without FIRE-pHLy) with compounds and assessed cathepsin D activity **(Figure 3.8A)**. Because cathepsin D auto-activates at acidic pH settings (Gulnik et al., 1992), its activity can be used as a functional readout of lysosomal pH; BODIPY FL-Pepstatin A is a cathepsin D antagonist that binds to the active form of the enzyme (Chen et al., 2000). Cells were treated with OSI-027 and PP-242 at 10 μM for various times before BODIPY FL Pepstatin A fluorescence was assayed **(Figure 3.8B)**. Compared to DMSO control, cathepsin D activity was significantly increased with OSI-027 and PP242 treatment. As a negative control, we tested bafilomycin A1 (BafA1), which increased pH by inhibiting the V-ATPase proton pump. BafA1 slightly decreased cathepsin D activity, but not significantly, suggesting that alkalinization of lysosomes did not further lower basal activated enzyme levels. Overall, the correlation between FIRE-pHLy ratio FC decrease and cathepsin D level increase validated OSI-027 and PP242 as robust lysosomal pH acidifiers.

After confirming that OSI-027 and PP-242 acidified lysosomal pH and increased active cathepsin D levels, we sought to validate these compounds in another native cell model, namely human induced pluripotent stem cell (iPSC)-derived astrocytes, or iAstrocytes. Quiescent (non-reactive) iAstrocytes stably expressing FIRE-pHLy were subsequently treated for 24 hours with OSI-027 and PP242 **(Figure 3.8C)**. Both compounds acidified pH (~50% reduction in FIRE-pHLy ratio FC) in iAstrocytes compared to control treatment, providing further support that these compounds acidify lysosomes across multiple cell types.

Reactive astrocytes secrete neurotoxic factors and have been implicated in the neuroinflammatory pathogenesis of neurodegenerative diseases (Phatnani & Maniatis, 2015).

Recently, Rooney et al. described an *in vitro* system to model inflammatory reactive astrocytes (Leng et al., 2021; Rooney et al., 2021). Reactive iAstrocytes activated by cytokines exhibited an alkaline lysosomal pH, which was accompanied by increased levels of lysosomal exocytosis, a contributor to neurotoxicity (Rooney et al., 2021). When reactive iAstrocytes were treated with 10 µM of PP242, elevated lysosomal pH was restored to control levels and was accompanied by a reduction in lysosomal exocytosis (Rooney et al., 2021). Ultimately, these data supported the notion that aberrant lysosomal pH was a contributing factor to neuroinflammation-induced functional changes in neurodegenerative disease and may be corrected with small molecules such as PP242 and OSI-027. Taken together, the acidifying effect of OSI-027 and PP242 in lysosomes was recapitulated in disease models. We posit that its effects may be therapeutic in other contexts of lysosomal dysfunction.

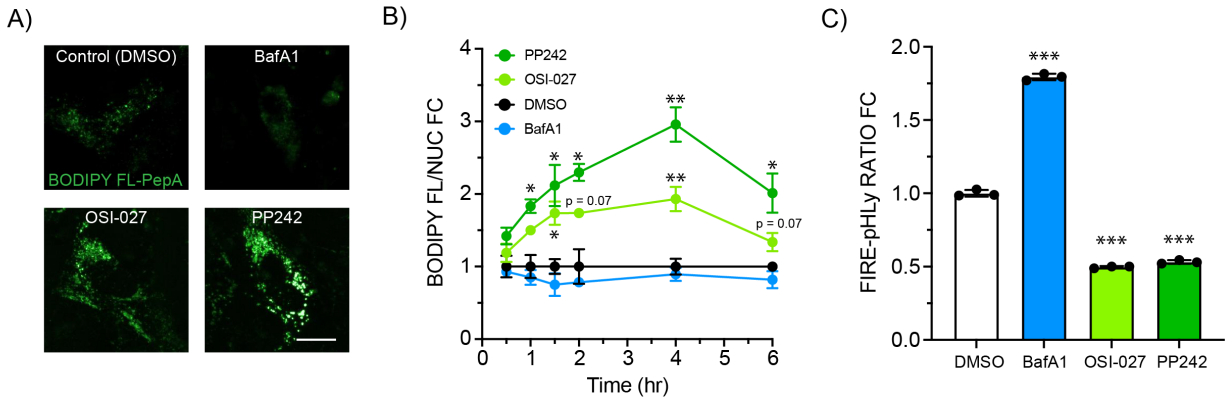

Figure 3.8. OSI-027 and PP242 increases mature cathepsin D levels and acidifies pH in human iAstrocytes. (A) Representative fluorescence images of undifferentiated SH-SY5Y cells treated with DMSO, 100 nM BafA1, 10 µM OSI-027, and 10 µM PP242 at t = 6 hrs and stained with BODIPY FL Pepstatin A probe. Scale bar = 10 µm. (B) Time course of cells treated with compounds for 0.5, 1, 1.5, 2, 4, and 6 hours. Cells were incubated with BODIPY FL Pepstatin A for 30 min before live-imaging. BODIPY FL fluorescence was normalized to cell number, displayed as a fold change relative to control, and plotted against time (hours). Data points are presented as mean ± SD, from 3 biological replicates; n = ~15,000-20,000 cells quantified per condition group per time point. Statistical analysis was performed using two-way ANOVA for multiple comparisons. *p ≤ 0.05; **p ≤ 0.01. (C) Bar graph quantification of FIREpHLy ratio fold-change (FC) in human iPSC-derived astrocytes (iAstrocytes) treated with OSI-027 and PP242 at 10 µM for 24 hours. Data points are presented as median ± SD from 3 technical replicates. Statistical analysis was performed using one-way ANOVA for multiple comparisons. **p ≤ 0.01; ***p ≤ 0.001; ns = not significant.

Lysosomal acidification induced by OSI-027 and PP242 correlates with mTOR inhibition and autophagy activation

Both OSI-027 and PP242 are described as potent and selective ATP-competitive inhibitors of mammalian target of rapamycin (mTOR) (Apsel et al., 2008; Bhagwat et al., 2011; Falcon et al., 2011). mTOR forms two protein complexes, mTORC1 and mTORC2; these signaling complexes **(Figure 3.9A)** form a major hub that regulates cellular processes such as metabolism, growth, and proliferation. mTOR inhibition is coupled with autophagy induction, which is associated with lysosomal activation and acidification (Kim & Guan, 2015; Yim & Mizushima, 2020; Zhou et al., 2013).

To understand whether the lysosomal acidification promoted by OSI-027 and PP242 was related to their role as mTOR inhibitors, we assessed mTOR inhibition and autophagy activation **(Figure 3.9)**. Both compounds dose-dependently inhibited downstream targets of mTORC1 **(Figure 3.9B, 3.9D)** and mTORC2 **(Figure 3.9B, 3.9E)** in undifferentiated SH-SY5Y cells. mTORC1 activity was measured by the phosphorylation state of P70 S6 Kinase (P70S6K) at position Thr389 and mTORC2 activity was assessed by the phosphorylation of Akt at position Ser473.

After confirming that OSI-027 and PP242 inhibited mTOR, we measured their ability to activate autophagy. mTORC1 negatively regulates autophagy through the phosphorylation of Unc-51 like autophagy activating kinase (ULK1) at Ser757 (Jung et al., 2009). OSI-027 and PP242 reduced $ULK1^{Ser757}$ levels dose-dependently with near complete reduction at 10 μM **(Figure 3.9C, 3.9F),** suggesting that both drugs initiated mTORC1-dependent autophagy. We then measured the levels of microtubule-associated protein light chain 3B (LC3B). The conversion of LC3B-I to LC3B-II correlates with the number of formed autophagosomes and

therefore reflects autophagy activation (Klionsky et al., 2016; Menzies et al., 2012). The ratio of LC3B-II to LC3B-I increased at higher OSI-027 and PP242 doses, achieving significance at 10 μM **(Figure 3.9C, 3.9G)**. Together, these results demonstrated that OSI-027 and PP242 induced autophagy, indicating that their ability to acidify lysosomes may be secondary to induction of autophagy rather than direct action on the lysosome.

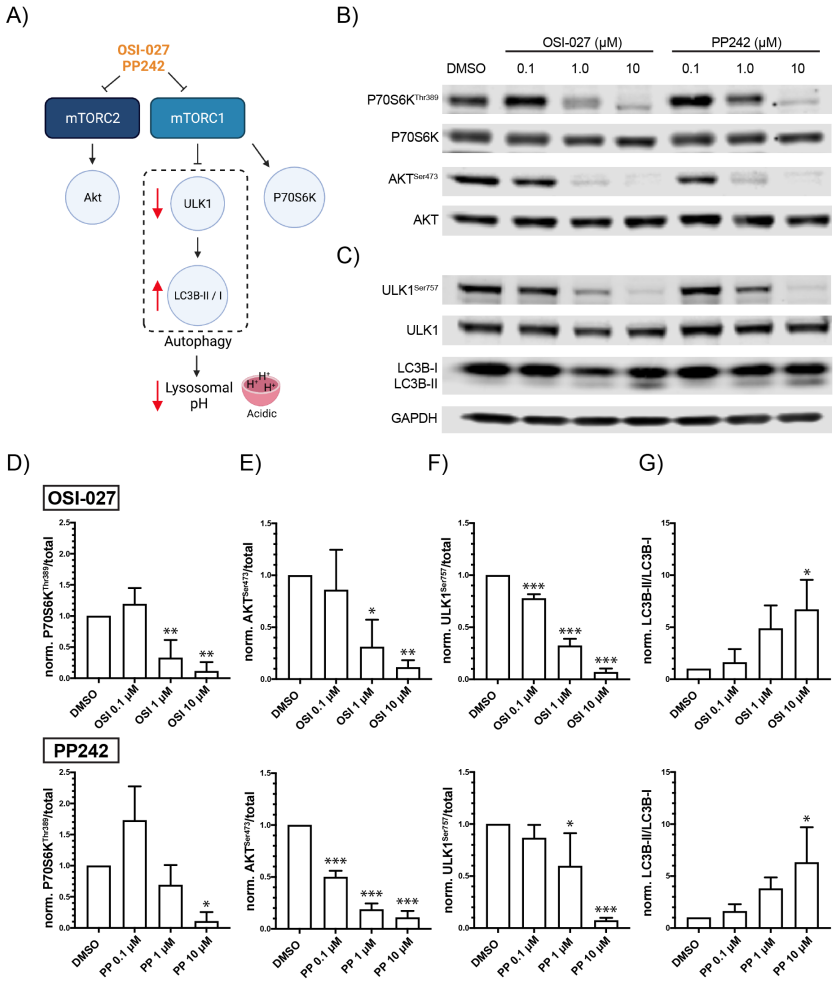

Figure 3.9. OSI-027 and PP242 inhibits mTORC1/2 and activates autophagy markers.
(A) Simplified schematic of the proposed mechanism for OSI-027 and PP242-mediated lysosomal acidification through autophagy (highlighted in red arrows). Compounds are shown in orange. (B) Representative immunoblots for mTORC1 and mTORC2 phosphorylation substrates P70S6K^{Thr389} and Akt^{Ser473}, respectively, in FIRE-pHLy SH-SY5Y cells treated with OSI-027 and PP242 at 0.1, 1, and 10 μM. (C) Representative immunoblots for autophagy markers ULK1^{Ser757} and LC3B-I/LC3B-II, respectively, in FIRE-pHLy SH-SY5Y cells treated with OSI-027 (OSI) and PP242 (PP) (same as above). GAPDH was used as the housekeeping protein. (D) Bar graphs showing quantification of P70S6K^{Thr389}/total (E) Akt^{Ser473}/total, (F) ULK1^{Ser757}/total, and (G) LC3B-II/LC3B-I. OSI-027 shown in top row; PP242 shown in bottom row. Data is normalized to DMSO controls. Bars are presented as mean ± SD from 3 independent replicates. Statistical analysis was performed using one-way ANOVA for multiple comparisons. *p ≤ 0.05; **p ≤ 0.01; ***p ≤ 0.001.

OSI-027 and PP242 acidifies lysosomes more potently than other mTOR inhibitors

Interestingly, our compound screen included other mTOR inhibitors, such as rapamycin and torin1, that were not identified as primary hits in our screen. To assess the differential effectiveness of additional mTOR inhibitors in modulating lysosomal pH, we retested rapamycin and torin 1 in FIRE-pHLy expressing SH-SY5Y cells over 24 hrs **(Figure 3.10)**. Confirming our screening results, OSI-027 and PP242 treatment induced a dose- and time-dependent decrease in lysosomal pH in cells **(Figures 3.10A, 3.10B)**, but treatment with rapamycin and torin1 did not acidify lysosomes across the tested dose range up to 24 hours **(Figures 3.10C, 3.10D)**. These results suggested that at the dosage and timing used in these experiments, OSI-027 and PP242 were more effective in acidifiying lysosomal pH in differentiated SH-SY5Y cells than the mTOR inhibitors torin1 and rapamycin.

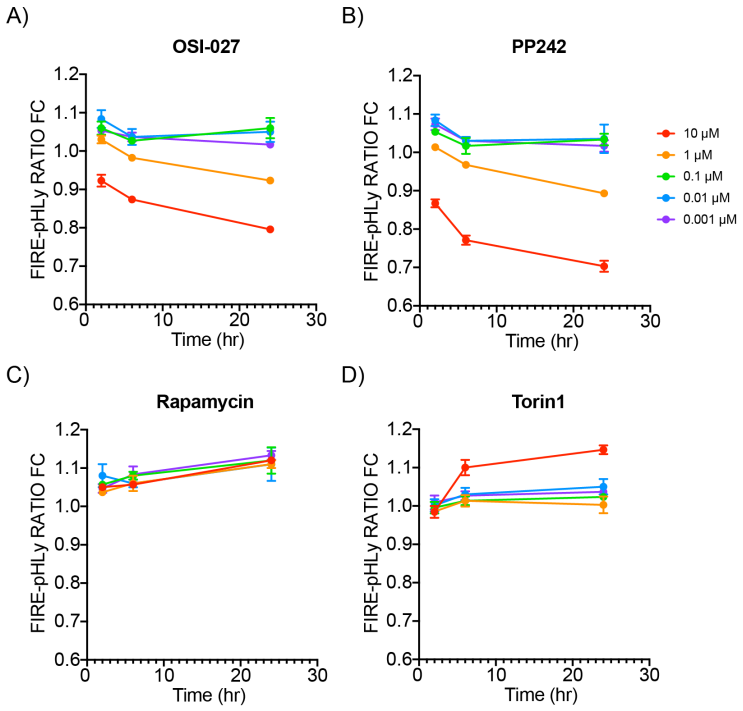

Figure 3.10. Dose-response and time-course comparison of mTOR inhibitors on lysosomal acidification. Five-point dose response (10-fold serial dilution) from 0.0001 µM to 10 µM treatment of (A) OSI-027, (B) PP242, (C) Rapamycin and (D) Torin1 measured after 2, 6, and 24 hours in FIRE-pHLy expressing SH-SY5Y cells. FIRE-pHLy ratio measurements were normalized to dose- and time-matched controls. Data points are presented as mean ± SD, from 3 technical replicates; n = ~15,000-20,000 cells quantified per condition group per time point.

Since we proposed that OSI-027 and PP242 induced pH acidification by activating autophagy, we hypothesized that rapamycin and torin1 did not activate autophagy in SH-SY5Y cells, at the doses and timing used in this study. Indeed, rapamycin did not significantly reduce ULK1^{Ser757} levels nor increase the ratio of LC3B-I and LC3B-II, indicating that autophagy was not activated under these conditions **(Figure 3.11A)**. Although torin1 treatment did reduce ULK1^{Ser757} levels starting at 100 nM compound, it did not significantly increase LC3B-II/LC3B-I ratio **(Figure 3.11B**), suggesting that torin1 did not induce autophagy as strongly as OSI-027 and PP242.

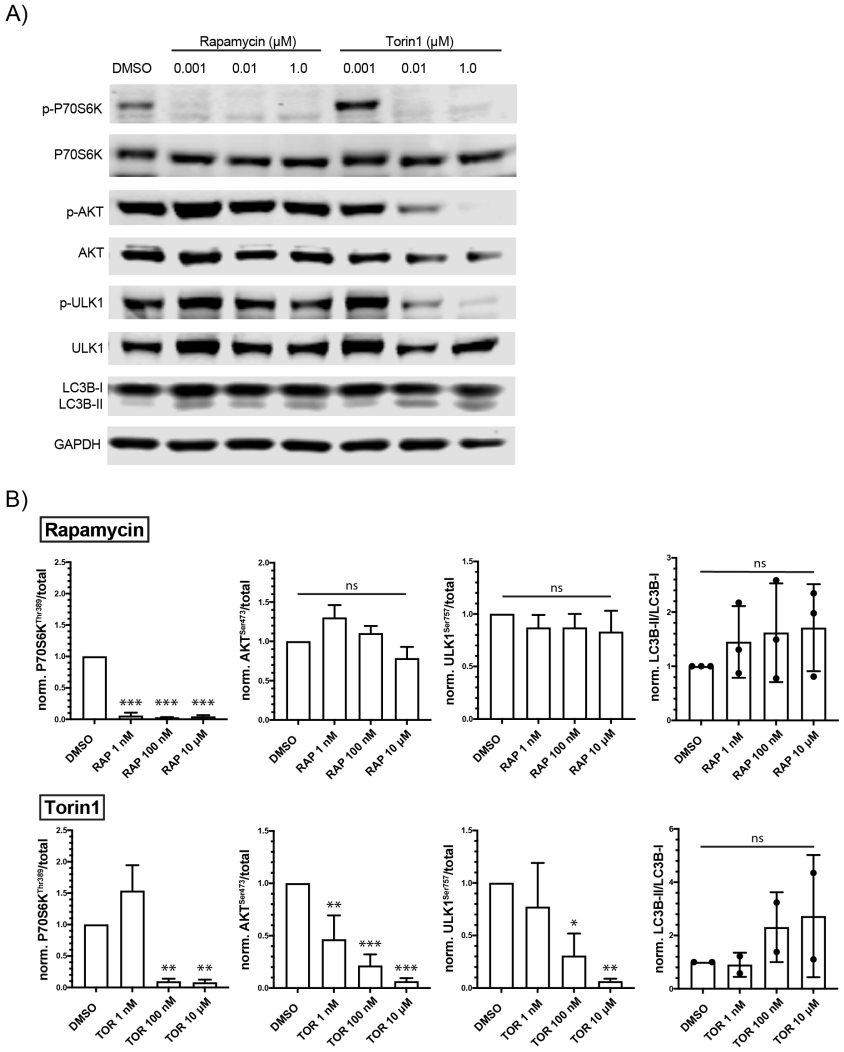

Figure 3.11. Immunoblotting for mTORC1/2 proteins after rapamycin and torin1 treatment.
(A) Representative immunoblots for mTORC1 and mTORC2 phosphorylation substrates P70S6K^{Thr389} and Akt^{Ser473} and autophagy markers ULK1^{Ser757} and LC3B-II/LC3B-I in undifferentiated FIRE-pHLy expressing SH-SY5Y cells treated with rapamycin and torin1 at 1 nM, 100 nM, and 10 μM. (B) Bar graphs showing quantification of mTOR1/2 markers (P70S6K^{Thr389}/total, Akt^{Ser473}/total, respectively) and autophagy markers (ULK1^{Ser757}/total, LC3B-II/LC3B-I). Data was normalized to DMSO controls. Data points are presented as mean ± S.D from 2-3 independent replicates. Statistical analysis was performed using one-way ANOVA for multiple comparisons. *$p \leq 0.05$; **$p \leq 0.01$; ***$p \leq 0.001$; ns = not significant.

In summary, we performed a high-content imaging-based phenotypic screen to identify small molecules that modulate lysosomal pH with a specific focus on acidifying compounds. We identified sixteen acidic and twenty-nine alkaline compounds using two distinct hit selection approaches. Population-based analysis is used in standard plate-based HTS studies, while object-based analysis provides a novel technique that could be used in future studies to dissect organelle subpopulation phenotypes.

Ultimately, we validated two out of the sixteen primary acidic hits. This hit rate may be a product of both biological factors such as lysosomal pH dynamics and screening limitations such as library size and protein druggability of the target. We suppose that because basal lumenal pH of lysosomes is already highly acidic (~4.5) compared to other cellular compartments, acidification beyond this set-point may be tightly regulated or even perhaps detrimental to the cell in certain contexts. This may explain the reduced dynamic range of FIRE-pHLy signal exhibited by acidifiers compared to alkalinizing compounds. Indeed, only a few examples highlight specific roles of lysosomal hyper-acidification in melanosome trafficking (van der Poel et al., 2011) and phospholipid biosynthesis (Lenk et al., 2019).

Alkaline compartments, on the other hand, are more common in the cell. In fact, lysosomes mature from the endolysosomal network, which maintains more alkaline pH ranges. Exogenous agents, such as drugs, have also been known to accumulate in acidic vesicles, such as lysosomes, and affect the local pH (De Duve et al., 1974; Kuzu et al., 2017). It is conceivable that perturbations in the alkaline direction are generally better tolerated in the cell, supporting

our observation that alkalinizing compounds exhibited a larger signal range in the primary screen.

OSI-027 and PP242 were identified as top acidic hits, demonstrating lysosomal pH lowering effects in undifferentiated and differentiated SH-SY5Y neuronal-like cells and in basal and activated iAstrocytes, possibly through activation of autophagy. Indeed, other groups have utilized OSI-027 and PP242 to study autophagy in the context of neurodegenerative disease models. For example, Silva et al. identified OSI-027 as a top hit in a mutant tau protein lowering screen performed in patient iPSC-derived neurons (Silva et al., 2020). Consistent with our data, OSI-027 lowered total mutant tau^{A152T} and hyperphosphorylated tau^{Ser396} levels at 1 and 10 μM, suggesting the correlation between lysosomal acidification and enhanced tau clearance. Interestingly, the tau lowering effect for OSI-027 was much stronger than that of rapamycin. Moreover, one group showed in a Parkinson's disease neuroinflammation model that impaired lysosomal acidification was accompanied by alpha-synuclein accumulation (Wang et al., 2015). Treatment with 40 nM PP242 rescued lysosomal pH and normalized alpha-synuclein protein levels in mouse PC12 cells and primary midbrain neurons. Together, these data support the supposition that OSI-027 and PP242 acidify lysosomes and thereby restore normal degradative function in neuronal cells.

It is still unknown why OSI-027 and PP242 are more effective in activating autophagy and decreasing lysosomal pH than other mTOR inhibitors such as torin1 and rapamycin. It is plausible that OSI-027 and PP242 have undescribed targets independent of mTOR that may be contributing to autophagy and lysosomal acidity. According to the KINOMEscan database (Fabian et al., 2005), an assay platform that annotates competitive binding between inhibitors and a panel of known kinases, PP242 binds to multiple other kinases. These include

phosphoinositide 3-kinase (PI3K) and ABL proto-oncogene 1 (ABL1), which have reported roles in regulating autophagy from cancer studies (Elzinga et al., 2013; Iershov et al., 2019; S. Wang et al., 2017; Yogalingam & Pendergast, 2008). Thus, by evaluating the other targets of OSI-027 and PP242, one may identify additional, mTOR-independent, mechanisms of lysosomal acidification. Importantly, OSI-027 and PP242 may serve as 'tool' compounds for further investigation of the mechanisms driving autophagy-mediated lysosomal activation in the context of neurodegenerative diseases.

METHODS

Compound library and re-purchased compounds

The library consisted of 1,835 compounds assembled from the commercially available SelleckChem bioactive collection (SelleckChem, Houston, TX). For dose-response and further validations, compounds were re-purchased from SelleckChem, unless otherwise indicated. Repurchased compounds were evaluated for purity by liquid chromatography/mass spectrometry.

Cell line maintenance and differentiation in 96-well microplates

Human SH-SY5Y neuroblastoma cells expressing the FIRE-pHLy construct were maintained in 1:1 Eagle's minimum essential medium (EMEM; ATCC, #30-2003) and F12 medium (Life Technologies; Carlsbad, CA, #11765062) with 10% FBS and 1% pen/strep under standard humidified conditions of 37ºC and 5% CO_2 atmosphere (Chin et al., 2021). Cells were trypsinized with 0.25% trypsin/EDTA solution (Sigma, #T4049) and seeded into collagen type-I-coated μClear 96-well microplates (Greiner Bio-One, #655956) at a low density of 10,000 cells/cm^2 with a total well volume of 100 μL using the WellMate microplate dispenser (Thermo Scientific, Waltham, MA) to allow for proliferation during the first phase of differentiation. Plates were incubated overnight at 37ºC/5% CO_2 before start of differentiation, as previously described (Chin et al., 2021). Briefly, cells were maintained in FBS(+) media supplemented with 10 μM retinoic acid (RA) from Days 0-6 and FBS-free media supplemented with 50 ng/mL brain-derived growth factor (BDNF) until compound pinning on Day 10.

HTS ratiometric FIRE-pHLy lysosomal pH reporter assay

The drug screen was performed at the UCSF Small Molecule Discovery Center (SMDC). From the library plate (5 mM stock dissolved in DMSO), 200 nL of compound was added in singlicate to 96-well assay plates (10 μM final screening concentration) using a fixed-volume pin tool (V&P Scientific, San Diego, CA) loaded onto the BioMek-FXP liquid handling automation workstation (Beckman Coulter, Brea, CA). DMSO was added to negative control wells on every assay plate. Assay plates were incubated for 6 hours (37^{O}C and 5% CO_2). 50 μL of 6% PFA (diluted in serum-free media) was dispensed directly into each 100 μL assay well (2% PFA final concentration) and shaken briefly using the EL406 Combination Washer Dispenser (BioTek, Winooski, VT). Plates were fixed at room temperature (RT) for 15 min and washed once with 100 μL 1X D-PBS (with $MgCl_2$ and $CaCl_2$). Cells were stained with 1:1000 (vol/well) Hoechst dye (10 mg/mL Hoechst 33342 solution, Thermo Fisher, #H3570) diluted in D-PBS for 20 min at RT protected from light and washed once with 1X D-PBS (with $MgCl_2$ and $CaCl_2$). Plates were wrapped and stored at 4^{O}C protected from light.

High-content confocal imaging, analysis types, and data output

Following our previously described imaging methods and feature extraction protocols (Chin et al., 2021), assay plates were imaged on the IN Cell 6500 HS Analyzer (General Electric Life Sciences/Cytiva, Marlborough, MA) and quantified on the IN Cell Developer Toolbox v1.9 (GE Life Sciences/Cytiva).

After acquisition of images, data was analyzed using two separate quantification pipelines – **(I)** Population-based and **(II)** Object-based analysis - to select primary acidic and alkaline hits.

I. Population-based analysis

The following parameters were quantified (per well) from image stacks:

- Total count of nuclei (i.e. cell count) = "COUNT_NUC"
- Total mCherry fl. intensity = "DxA_CHERRY_SUM"
- Total mCherry-masked mTFP1 fl. intensity = "DxA_CHERRY MASK TEAL_SUM"

Data was formatted as a .CSV file and analyzed using custom analysis protocol on Pipeline Pilot (Biovia). Relative lysosomal pH change was determined by calculating the "FIRE-pHLy ratio" (DxA_CHERRY MASK TEAL_SUM/DxA_CHERRY_SUM). Fold change was calculated by taking the sample result value divided by the mean of the plate-matched negative control.

II. Object-based analysis

The following parameters were quantified (per segmented mCherry-positive object) from image stacks:

- mCherry fluorescence intensity = "DxA_CHERRY_SINGLE"
- mCherry-masked mTFP1 fl. intensity = "DxA_CHERRY MASK TEAL_SINGLE"
- FIRE-pHLy ratio = "DxA_RATIO_SINGLE" (i.e. DxA_CHERRY MASK TEAL_SINGLE/DxA_CHERRY_SINGLE)
- Total lysosomal objects between $0.00 \leq$ DxA_RATIO_SINGLE ≤ 1.00 = "Bin0"
- Total lysosomal objects with DxA_RATIO_SINGLE every 0.05 increments
    - "Bin1" = $0.00 \leq$ DxA_RATIO_SINGLE < 0.05
    - Bin2 = $0.05 \leq$ DxA_RATIO_SINGLE < 0.10

- Bin3 = 0.10 ≤ DxA_RATIO_SINGLE < 0.15
- Bin4 = 0.15 ≤ DxA_RATIO_SINGLE < 0.20
- Bin5 = 0.20 ≤ DxA_RATIO_SINGLE < 0.25
- Bin6 = 0.25 ≤ DxA_RATIO_SINGLE < 0.30
- Bin7 = 0.30 ≤ DxA_RATIO_SINGLE < 0.35
- Bin8 = 0.35 ≤ DxA_RATIO_SINGLE < 0.40
- Bin9 = 0.40 ≤ DxA_RATIO_SINGLE < 0.45
- Bin10 = 0.45 ≤ DxA_RATIO_SINGLE < 0.50
- Bin11 = 0.50 ≤ DxA_RATIO_SINGLE < 0.55
- Bin12 = 0.55 ≤ DxA_RATIO_SINGLE < 0.60
- Bin13 = 0.60 ≤ DxA_RATIO_SINGLE < 0.65
- Bin14 = 0.65 ≤ DxA_RATIO_SINGLE < 0.70
- Bin15 = 0.70 ≤ DxA_RATIO_SINGLE < 0.75
- Bin16 = 0.75 ≤ DxA_RATIO_SINGLE < 0.80
- Bin17 = 0.80 ≤ DxA_RATIO_SINGLE < 0.85
- Bin18 = 0.85 ≤ DxA_RATIO_SINGLE < 0.90
- Bin19 = 0.90 ≤ DxA_RATIO_SINGLE < 0.95
- Bin20 = 0.95 ≤ DxA_RATIO_SINGLE ≤ 1.00

- Fraction of total lysosomal objects from Bins 1 to 20 = “FRACTION Bin 1-20” (e.g. FRACTION Bin1 = Bin1/Bin0)

Data was formatted as a .CSV file and analyzed using Pipeline Pilot. Frequency and count distributions of binned lysosomal objects were generated. Hit selection metrics such as ‘Median bin” and ‘Bin at max” were calculated.

The cumulative frequency and bin containing the max value was computed by iterating through the bins. A sigmoidal curve was fit to the cumulative frequency; the bottom was fixed at 0 and the top was fixed at 1. If an EC50 was able to be determined, EC25 was computed using POWER((25/(100-25)), 1/HILL)*EC50; EC75 was computed using POWER((75/(100-75)), 1/HILL)*EC50. IQR was computed taking the difference between the log10 of these two values (LOGEC75-LOGEC25).

Population-based and lysosomal-object data output was uploaded onto the SMDC HiTS server and will be made available upon request.

BODIPY FL Pepstatin A live-cell time course assay

Mature cathepsin D levels were assessed via BODIPY FL Pepstatin A staining on live cells . The staining protocol was performed according to the manufacturer's protocol (Chen et al., 2000). Briefly, cells were seeded in 96-well plates, cultured overnight and treated for 30, 60, 90, 120, 240, and 360 mins with 100 nM bafilomycin A1, 10 μM OSI-027, 10 μM PP-242, and DMSO as the solvent control. Prior to imaging, cells were incubated for 30 minutes with a staining solution consisting of 1 μM BODIPY FL Pepstatin A and 1:1000 (vol/well) Hoescht nuclear dye. Cells were washed once with D-PBS and imaged live on the IN Cell Analyzer 6500 HS and processed according to an adapted protocol on IN Cell Developer Toolbox v1.9.

Immunoblotting

Western blots were performed as previously described (Chin, Patwardhan, et al., 2021b).

Primary antibodies

Rabbit anti-ULK (1:1000, Cell Signaling, #8054)

Rabbit anti-ULK^{Ser757} (1:1000, Cell Signaling, #14202)

Rabbit anti-p70S6K (1:1000, Cell Signaling, #2708)

Rabbit anti-P70S6K^{Thr389} (1:1000, Cell Signaling, #9234)

Rabbit anti-Akt (1:1000, Cell Signaling, #9272)

Rabbit anti-Akt^{Ser437} (1:1000, Cell Signaling, #4060)

Rabbit anti-LC3B (1:1000, Sigma, #L7543)

Mouse anti-GAPDH (1:5000, Abcam, #8245)

Secondary antibodies

Donkey anti-Mouse Green (1:10,000, LICOR, #926-32212)

Donkey anti-Rabbit Green (1:10,000, LICOR, #926-32213)

Donkey anti-Rabbit Red (1:10,000, LICOR, #926-68073)

iAstrocyte experiments

iAstrocytes were generated as detailed in Leng et al. (Leng et al., 2021). Day 20 iAstrocytes were plated in ScienCell Astrocyte Media (ScienCell Research Laboratories cat. no. 1801) at 20,000 cells/cm^2 on BioLite Cell Culture Treated 96-well plates (ThermoFisher Scientific cat. no. 12-556-008) coated with Growth Factor Reduced, Phenol Red-Free, LDEV-Free Matrigel Basement Membrane Matrix (Corning cat. no. 356231) diluted 1:200 in DMEM/F12 (ThermoFisher Scientific cat. no. 11330032). iAstrocytes were transduced with FIRE-pHLy lentivirus at the

time of plating. Full media changes with ScienCell Astrocyte Media were conducted on days 1, 3, and 5 after plating. On day 5, small-molecule compounds were diluted in media to 10 μM. After 24 hours (i.e. on day 6 after plating), iAstrocytes were incubated with Accutase Cell Dissociation Reagent (ThermoFisher Scientific cat. no. A11105-01) for 10 mins at 37 °C and diluted in Dulbecco's phosphate buffered saline (DPBS; Milipore Sigma cat. no. D8537) for flow cytometry analysis.

Data from flow cytometry experiments were analyzed using FlowJo (version 10.7.1). FIRE-pHLy-positive populations were determined through live cell (SSC-A vs. FSC-A), single cell (FSC-H vs. FSC-A) and transduced ($mCherry^+$) gating strategies. FIRE-pHLy signal was quantified as the Median FITC-A:mCherry-A ratio for each well.

Data presentation, statistical analysis, and illustrations

Visualization of control and screening hit data was performed on the SMDC HiTS server and DataWarrior, an open-source cheminformatics tool. Pre-processing of data was organized in Microsoft Excel. Calculations of hit selection measurements were conducted on Pipeline Pilot (Biovia) (**Methods**). Dose-response curves were generated using a simple linear regression model in GraphPad Prism 9. For validation expeiments, all data were generated from randomly selected sample populations from at least three independent experiments represented unless otherwise mentioned in corresponding figure legends. Statistical data were presented as mean ± S.D or S.E.M. Multiple comparisons between groups were analyzed by one-way or two-way ANOVA test. All data plots and statistical analyses were performed using GraphPad Prism 9 with no samples excluded. Significant differences between experimental groups were indicated

as *P<0.05; **P<0.01; ***P<0.001; Only P <0.05 was considered as statistically significant. NS = not significant. Immunoblot images and quantifications were acquired from Image Studio (LI-COR Biosciences). Cartoon schematics were created on Biorender.com. Figures were assembled on Adobe Illustrator and Adobe Photoshop.

DATA AND REAGENT AVAILABLE

The authors declare that all relevant data supporting the findings of this study are available within the paper. Any data or reagents can be obtained from the corresponding authors (A.W.K. and M.R.A.) on reasonable request.

ACKNOWLEDGEMENTS

We thank the UCSF Small Molecule Discovery Center for their assistance on drug screening procedures, data management and storage. We also thank Deanna Kroetz for insights on drug screening and validation. Finally, we thank members of the Kao and Arkin labs for their thoughtful discussions. This work has received support from the NIH/NIA (R01 AG055342 to A.W.K; R01 AG062359 to M.K.; F30 AG066418 to K.L.).

AUTHOR CONTRIBUTIONS

M.Y.C., M.R.A., and A.W.K. for conceptualization and design; M.Y.C., K.A., J.D., C.A. and V.G.G. for experimental design and data acquisition; B.R., K.L and M.K. for conceptualization, design and data acquisition of iAstrocyte experiments; all authors analyzed and interpreted data; M.Y.C., M.R.A., and A.W.K. wrote the manuscript; all authors edited the manuscript.

COMPETING INTERESTS STATEMENT

The authors declare no competing financial interests.

REFERENCES

1. Apsel, B., Blair, J. A., Gonzalez, B. Z., Nazif, T. M., Feldman, M. E., Aizenstein, B., Hoffman, R., Williams, R. L., Shokat, K. M., & Knight, Z. A. (2008). Targeted polypharmacology: Discovery of dual inhibitors of tyrosine and phosphoinositide kinases. *Nature Chemical Biology*, *4*(11), 691–699. https://doi.org/10.1038/nchembio.117
2. Ballabio, A., & Bonifacino, J. S. (2020). Lysosomes as dynamic regulators of cell and organismal homeostasis. *Nature Reviews Molecular Cell Biology*, *21*(2), 101–118. https://doi.org/10.1038/s41580-019-0185-4
3. Baxi, K., Ghavidel, A., Waddell, B., Harkness, T. A., & Carvalho, C. E. de. (2017). Regulation of Lysosomal Function by the DAF-16 Forkhead Transcription Factor Couples Reproduction to Aging in Caenorhabditis elegans. *Genetics*, *207*(1), 83–101. https://doi.org/10.1534/genetics.117.204222
4. Bhagwat, S. V., Gokhale, P. C., Crew, A. P., Cooke, A., Yao, Y., Mantis, C., Kahler, J., Workman, J., Bittner, M., Dudkin, L., Epstein, D. M., Gibson, N. W., Wild, R., Arnold, L. D., Houghton, P. J., & Pachter, J. A. (2011). Preclinical Characterization of OSI-027, a Potent and Selective Inhibitor of mTORC1 and mTORC2: Distinct from Rapamycin. *Molecular Cancer Therapeutics*, *10*(8), 1394–1406. https://doi.org/10.1158/1535-7163.MCT-10-1099
5. Bright, N. A., Davis, L. J., & Luzio, J. P. (2016). Endolysosomes Are the Principal Intracellular Sites of Acid Hydrolase Activity. *Current Biology*, *26*(17), 2233–2245. https://doi.org/10.1016/j.cub.2016.06.046
6. Cabukusta, B., & Neefjes, J. (2018). Mechanisms of lysosomal positioning and movement. *Traffic*, *19*(10), 761–769. https://doi.org/10.1111/tra.12587

7. Casey, J. R., Grinstein, S., & Orlowski, J. (2010). Sensors and regulators of intracellular pH. *Nature Reviews Molecular Cell Biology*, *11*(1), 50–61. https://doi.org/10.1038/nrm2820

8. Chen, C.-S., Chen, W.-N. U., Zhou, M., Arttamangkul, S., & Haugland, R. P. (2000). Probing the cathepsin D using a BODIPY FL–pepstatin A: Applications in fluorescence polarization and microscopy. *Journal of Biochemical and Biophysical Methods*, *42*(3), 137–151. https://doi.org/10.1016/S0165-022X(00)00048-8

9. Chin, M. Y., Espinosa, J. A., Pohan, G., Markossian, S., & Arkin, M. R. (2021). Reimagining dots and dashes: Visualizing structure and function of organelles for high-content imaging analysis. *Cell Chemical Biology*, *28*(3), 320–337. https://doi.org/10.1016/j.chembiol.2021.01.016

10. Chin, M. Y., Patwardhan, A. R., Ang, K.-H., Wang, A. L., Alquezar, C., Welch, M., Nguyen, P. T., Grabe, M., Molofsky, A. V., Arkin, M. R., & Kao, A. W. (2021). Genetically Encoded, pH-Sensitive mTFP1 Biosensor for Probing Lysosomal pH. *ACS Sensors*. https://doi.org/10.1021/acssensors.0c02318

11. Colacurcio, D. J., & Nixon, R. A. (2016). Disorders of lysosomal acidification—The emerging role of v-ATPase in aging and neurodegenerative disease. *Ageing Research Reviews*, *32*, 75–88. https://doi.org/10.1016/j.arr.2016.05.004

12. De Duve, C., De Barsy, T., Poole, B., Trouet, A., Tulkens, P., & Van Hoof, F. (1974). Lysosomotropic agents. *Biochemical Pharmacology*, *23*(18), 2495–2531. https://doi.org/10.1016/0006-2952(74)90174-9

13. Elzinga, B. M., Nyhan, M. J., Crowley, L. C., O'Donovan, T. R., Cahill, M. R., & McKenna, S. L. (2013). Induction of autophagy by Imatinib sequesters Bcr-Abl in

autophagosomes and down-regulates Bcr-Abl protein. *American Journal of Hematology*, *88*(6), 455–462. https://doi.org/10.1002/ajh.23428

14. Encinas, M., Iglesias, M., Liu, Y., Wang, H., Muhaisen, A., Ceña, V., Gallego, C., & Comella, J. X. (2000). Sequential Treatment of SH-SY5Y Cells with Retinoic Acid and Brain-Derived Neurotrophic Factor Gives Rise to Fully Differentiated, Neurotrophic Factor-Dependent, Human Neuron-Like Cells. *Journal of Neurochemistry*, *75*(3), 991–1003. https://doi.org/10.1046/j.1471-4159.2000.0750991.x

15. Fabian, M. A., Biggs, W. H., Treiber, D. K., Atteridge, C. E., Azimioara, M. D., Benedetti, M. G., Carter, T. A., Ciceri, P., Edeen, P. T., Floyd, M., Ford, J. M., Galvin, M., Gerlach, J. L., Grotzfeld, R. M., Herrgard, S., Insko, D. E., Insko, M. A., Lai, A. G., Lélias, J.-M., … Lockhart, D. J. (2005). A small molecule-kinase interaction map for clinical kinase inhibitors. *Nature Biotechnology*, *23*(3), 329–336. https://doi.org/10.1038/nbt1068

16. Falcon, B. L., Barr, S., Gokhale, P. C., Chou, J., Fogarty, J., Depeille, P., Miglarese, M., Epstein, D. M., & McDonald, D. M. (2011). Reduced VEGF production, angiogenesis, and vascular regrowth contribute to the antitumor properties of dual mTORC1/mTORC2 inhibitors. *Cancer Research*, *71*(5), 1573–1583. https://doi.org/10.1158/0008-5472.CAN-10-3126

17. Forster, J. I., Köglsberger, S., Trefois, C., Boyd, O., Baumuratov, A. S., Buck, L., Balling, R., & Antony, P. M. A. (2016). Characterization of Differentiated SH-SY5Y as Neuronal Screening Model Reveals Increased Oxidative Vulnerability. *Journal of Biomolecular Screening*, *21*(5), 496–509. https://doi.org/10.1177/1087057115625190

18. Gulnik, S., Baldwin, E. T., Tarasova, N., & Erickson, J. (1992). Human liver cathepsin D. *Journal of Molecular Biology*, *227*(1), 265–270. https://doi.org/10.1016/0022-2836(92)90696-H

19. Hughes, A. L., & Gottschling, D. E. (2012). An early age increase in vacuolar pH limits mitochondrial function and lifespan in yeast. *Nature*, *492*(7428), 261–265. https://doi.org/10.1038/nature11654

20. Iershov, A., Nemazanyy, I., Alkhoury, C., Girard, M., Barth, E., Cagnard, N., Montagner, A., Chretien, D., Rugarli, E. I., Guillou, H., Pende, M., & Panasyuk, G. (2019). The class 3 PI3K coordinates autophagy and mitochondrial lipid catabolism by controlling nuclear receptor PPARα. *Nature Communications*, *10*(1), 1566. https://doi.org/10.1038/s41467-019-09598-9

21. Jung, C. H., Jun, C. B., Ro, S.-H., Kim, Y.-M., Otto, N. M., Cao, J., Kundu, M., & Kim, D.-H. (2009). ULK-Atg13-FIP200 Complexes Mediate mTOR Signaling to the Autophagy Machinery. *Molecular Biology of the Cell*, *20*(7), 1992–2003. https://doi.org/10.1091/mbc.E08-12-1249

22. Kim, Y. C., & Guan, K.-L. (2015). mTOR: A pharmacologic target for autophagy regulation. *The Journal of Clinical Investigation*, *125*(1), 25–32. https://doi.org/10.1172/JCI73939

23. Klionsky, D. J., Abdelmohsen, K., Abe, A., Abedin, M. J., Abeliovich, H., Acevedo Arozena, A., Adachi, H., Adams, C. M., Adams, P. D., Adeli, K., Adhihetty, P. J., Adler, S. G., Agam, G., Agarwal, R., Aghi, M. K., Agnello, M., Agostinis, P., Aguilar, P. V., Aguirre-Ghiso, J., … Zughaier, S. M. (2016). Guidelines for the use and interpretation of

assays for monitoring autophagy (3rd edition). *Autophagy*, *12*(1), 1–222. https://doi.org/10.1080/15548627.2015.1100356

24. Koh, J.-Y., Kim, H. N., Hwang, J. J., Kim, Y.-H., & Park, S. E. (2019). Lysosomal dysfunction in proteinopathic neurodegenerative disorders: Possible therapeutic roles of cAMP and zinc. *Molecular Brain*, *12*(1), 18. https://doi.org/10.1186/s13041-019-0439-2

25. Kuzu, O. F., Toprak, M., Noory, M. A., & Robertson, G. P. (2017). Effect of lysosomotropic molecules on cellular homeostasis. *Pharmacological Research*, *117*, 177–184. https://doi.org/10.1016/j.phrs.2016.12.021

26. Lawrence, R. E., & Zoncu, R. (2019). The lysosome as a cellular centre for signalling, metabolism and quality control. *Nature Cell Biology*, *21*(2), 133–142. https://doi.org/10.1038/s41556-018-0244-7

27. Lee, J.-H., McBrayer, M. K., Wolfe, D. M., Haslett, L. J., Kumar, A., Sato, Y., Lie, P. P. Y., Mohan, P., Coffey, E. E., Kompella, U., Mitchell, C. H., Lloyd-Evans, E., & Nixon, R. A. (2015). Presenilin 1 Maintains Lysosomal Ca2+ Homeostasis via TRPML1 by Regulating vATPase-Mediated Lysosome Acidification. *Cell Reports*, *12*(9), 1430–1444. https://doi.org/10.1016/j.celrep.2015.07.050

28. Leng, K., Rooney, B., Kim, H., Xia, W., Koontz, M., Krawczyk, M., Zhang, Y., Ullian, E. M., Fancy, S. P. J., Schrag, M. S., Lippmann, E. S., & Kampmann, M. (2021). *CRISPRi screens in human astrocytes elucidate regulators of distinct inflammatory reactive states* [Preprint]. Neuroscience. https://doi.org/10.1101/2021.08.23.457400

29. Lenk, G. M., Park, Y. N., Lemons, R., Flynn, E., Plank, M., Frei, C. M., Davis, M. J., Gregorka, B., Swanson, J. A., Meisler, M. H., & Kitzman, J. O. (2019). CRISPR

knockout screen implicates three genes in lysosome function. *Scientific Reports*, *9*(1), 9609. https://doi.org/10.1038/s41598-019-45939-w

30. Menzies, F. M., Moreau, K., Puri, C., Renna, M., & Rubinsztein, D. C. (2012). Measurement of Autophagic Activity in Mammalian Cells. *Current Protocols in Cell Biology*, *54*(1), 15.16.1-15.16.25. https://doi.org/10.1002/0471143030.cb1516s54

31. Mindell, J. A. (2012). Lysosomal Acidification Mechanisms. *Annual Review of Physiology*, *74*(1), 69–86. https://doi.org/10.1146/annurev-physiol-012110-142317

32. Monaco, A., & Fraldi, A. (2020). Protein Aggregation and Dysfunction of Autophagy-Lysosomal Pathway: A Vicious Cycle in Lysosomal Storage Diseases. *Frontiers in Molecular Neuroscience*, *13*. https://doi.org/10.3389/fnmol.2020.00037

33. Mony, V. K., Benjamin, S., & O'Rourke, E. J. (2016). A lysosome-centered view of nutrient homeostasis. *Autophagy*, *12*(4), 619–631. https://doi.org/10.1080/15548627.2016.1147671

34. Ohkuma, S. (1989). Use of fluorescein isothiocyanate-dextran to measure proton pumping in lysosomes and related organelles. In *Methods in Enzymology* (Vol. 174, pp. 131–154). Elsevier. https://doi.org/10.1016/0076-6879(89)74015-5

35. Phatnani, H., & Maniatis, T. (2015). Astrocytes in Neurodegenerative Disease. *Cold Spring Harbor Perspectives in Biology*, *7*(6), a020628. https://doi.org/10.1101/cshperspect.a020628

36. Ponsford, A. H., Ryan, T. A., Raimondi, A., Cocucci, E., Wycislo, S. A., Fröhlich, F., Swan, L. E., & Stagi, M. (2020). Live imaging of intra-lysosome pH in cell lines and primary neuronal culture using a novel genetically encoded biosensor. *Autophagy*, 1–19. https://doi.org/10.1080/15548627.2020.1771858

37. Rooney, B., Leng, K., McCarthy, F., Rose, I. V. L., Herrington, K. A., Bax, S., Chin, M. Y., Fathi, S., Leonetti, M., Kao, A. W., Elias, J. E., & Kampmann, M. (2021). *MTOR controls neurotoxic lysosome exocytosis in inflammatory reactive astrocytes* [Preprint]. Cell Biology. https://doi.org/10.1101/2021.09.11.459904

38. Ross, C. A., & Poirier, M. A. (2004). Protein aggregation and neurodegenerative disease. *Nature Medicine*, *10*(S7), S10–S17. https://doi.org/10.1038/nm1066

39. Settembre, C., Fraldi, A., Medina, D. L., & Ballabio, A. (2013). Signals for the lysosome: A control center for cellular clearance and energy metabolism. *Nature Reviews. Molecular Cell Biology*, *14*(5), 283–296. https://doi.org/10.1038/nrm3565

40. Silva, M. C., Nandi, G. A., Tentarelli, S., Gurrell, I. K., Jamier, T., Lucente, D., Dickerson, B. C., Brown, D. G., Brandon, N. J., & Haggarty, S. J. (2020). Prolonged tau clearance and stress vulnerability rescue by pharmacological activation of autophagy in tauopathy neurons. *Nature Communications*, *11*(1), 3258. https://doi.org/10.1038/s41467-020-16984-1

41. Sun, Y., Li, M., Zhao, D., Li, X., Yang, C., & Wang, X. (2020). Lysosome activity is modulated by multiple longevity pathways and is important for lifespan extension in C. elegans. *ELife*, *9*, e55745. https://doi.org/10.7554/eLife.55745

42. Tong, B. C.-K., Wu, A. J., Huang, A. S., Dong, R., Malampati, S., Iyaswamy, A., Krishnamoorthi, S., Sreenivasmurthy, S. G., Zhu, Z., Su, C., Liu, J., Song, J., Lu, J.-H., Tan, J., Pan, W., Li, M., & Cheung, K.-H. (2021). Lysosomal TPCN (two pore segment channel) inhibition ameliorates beta-amyloid pathology and mitigates memory impairment in Alzheimer disease. *Autophagy*, *0*(0), 1–19. https://doi.org/10.1080/15548627.2021.1945220

43. van der Poel, S., Wolthoorn, J., van den Heuvel, D., Egmond, M., Groux-Degroote, S., Neumann, S., Gerritsen, H., van Meer, G., & Sprong, H. (2011). Hyperacidification of Trans-Golgi Network and Endo/Lysosomes in Melanocytes by Glucosylceramide-Dependent V-ATPase Activity. *Traffic*, *12*(11), 1634–1647. https://doi.org/10.1111/j.1600-0854.2011.01263.x

44. Wang, S., Li, J., Du, Y., Xu, Y., Wang, Y., Zhang, Z., Xu, Z., Zeng, Y., Mao, X., & Cao, B. (2017). The Class I PI3K inhibitor S14161 induces autophagy in malignant blood cells by modulating the Beclin 1/Vps34 complex. *Journal of Pharmacological Sciences*, *134*(4), 197–202. https://doi.org/10.1016/j.jphs.2017.07.001

45. Webb, B. A., Aloisio, F. M., Charafeddine, R. A., Cook, J., Wittmann, T., & Barber, D. L. (2020). pHLARE: A New Biosensor Reveals Decreased Lysosome pH in Cancer Cells. *Molecular Biology of the Cell*, mbc.E20-06-0383. https://doi.org/10.1091/mbc.E20-06-0383

46. Xicoy, H., Wieringa, B., & Martens, G. J. M. (2017). The SH-SY5Y cell line in Parkinson's disease research: A systematic review. *Molecular Neurodegeneration*, *12*(1), 10. https://doi.org/10.1186/s13024-017-0149-0

47. Yim, W. W.-Y., & Mizushima, N. (2020). Lysosome biology in autophagy. *Cell Discovery*, *6*(1), 1–12. https://doi.org/10.1038/s41421-020-0141-7

48. Yogalingam, G., & Pendergast, A. M. (2008). Abl Kinases Regulate Autophagy by Promoting the Trafficking and Function of Lysosomal Components. *The Journal of Biological Chemistry*, *283*(51), 35941–35953. https://doi.org/10.1074/jbc.M804543200

49. Zhou, J., Tan, S.-H., Nicolas, V., Bauvy, C., Yang, N.-D., Zhang, J., Xue, Y., Codogno, P., & Shen, H.-M. (2013). Activation of lysosomal function in the course of autophagy

via mTORC1 suppression and autophagosome-lysosome fusion. *Cell Research*, *23*(4), 508–523. https://doi.org/10.1038/cr.2013.11

Publishing Agreement

It is the policy of the University to encourage open access and broad distribution of all theses, dissertations, and manuscripts. The Graduate Division will facilitate the distribution of UCSF theses, dissertations, and manuscripts to the UCSF Library for open access and distribution. UCSF will make such theses, dissertations, and manuscripts accessible to the public and will take reasonable steps to preserve these works in perpetuity.

I hereby grant the non-exclusive, perpetual right to The Regents of the University of California to reproduce, publicly display, distribute, preserve, and publish copies of my thesis, dissertation, or manuscript in any form or media, now existing or later derived, including access online for teaching, research, and public service purposes.

DocuSigned by:
Marcus Chin
D1A9529EAB584D9...
Author Signature

12/13/2021
Date